Chair of Applied Geophysics

Master's Thesis

3D Seismic Tomography of DT-1B Drill Site

Lucas Crozier Sutek Spriggs

May 2024

MONTANUNIVERSITÄT LEOBEN
www.unileoben.ac.at

AFFIDAVIT

I declare on oath that I wrote this thesis independently, did not use any sources and aids other than those specified, have fully and truthfully reported the use of generative methods and models of artificial intelligence, and did not otherwise use any other unauthorized aids.

I declare that I have read, understood and complied with the "Good Scientific Practice" of the Montanuniversität Leoben.

Furthermore, I declare that the electronic and printed versions of the submitted thesis are identical in form and content.

Date 20.05.2024

Signature Author
Lucas Crozier Sutek Spriggs

Acknowledgements

Many sincere thank yous are required for this Thesis. The first of which would go to PhD candidate Damian Pasiecznik. Without his guidance and help I would not have made it through this Thesis. The late-night beer chats discussing programming issues kept me sane. I owe you beers for life good sir. I truly appreciate all the assistance you gave me throughout the Thesis. I wish you the best in life man.

To my co-advisor Dr. Andrew Greenwood thank you for all the time and help you spent on guiding me through my Thesis. I know your time has been devoured by DIVE, and that it is relatively limited even with just teaching. Thank you for providing me with the opportunity with this Thesis, while knowing the extra stress you would have to deal with because of my Thesis.

I am grateful to Mrs. Christiane Pretzenbacher for all of her help throughout my entire Master's school experience. You were always very welcoming and helpful to a student who came from so far away to study in Leoben. I can honestly say that I do not know that I would have made it through the program without you. You helped me navigate Leoben and every process throughout my entire time here.

To Professor Bleibinhaus than you for accepting me into your MSc program. I learned much under your tutelage and in the degree program you run. It has been an honor to be your student.

To my family and friends unmentioned in this, you have been a support structure that helped me behind the scenes throughout my degree program, and people to talk to when I was stressed.

It’s been a great time in my life and I will never forget this unique experience. Thank you all.

Truly.

Abstract

Travel time tomography has been utilized to delineate the boundary between crystalline metamorphic lower crustal rocks and quaternary sediments of a site. The area investigated is approximately 50x50m within the Ivrea Verbano Zone (IVZ). The IVZ is a region of significant geological interest due to deep crustal segments that have been uplifted to shallow depths. DIVE (Drilling the Ivrea-Verbano zonE) is an international scientific collaboration, funded by the ICDP, which aims to unravel fundamental inquiries of the IVZ. This is done through drilling 3 drillholes, one of which is DT-1B located in Ornavasso Italy. In order to characterise the DT-1B drill site, geophysical investigations were conducted prior to the start of drilling activities including Ground Penetrating Radar (GPR), Electrical Resistivity Tomography (ERT), and active-source seismic surveys. The seismic data was acquired as a tightly spaced 3-D rolling spread with the source lines offset from the geophone lines. This source-receiver geometry is not optimal for 2-D seismic refraction profiling, and a 3-D refraction travel-time tomography scheme was subsequently used to derive a subset of 2.5-D profiles that span the drilling site. An Eikonal solver was used to generate velocity models and produce theoretical travel-time curves. The starting velocity model utilized velocities derived from first-break analysis and subsurface geometry assumed from the ERT and GPR data results. An RMS error of 4.97 ms between the observed and calculated travel-times is achieved after 12 iterations. The final velocity models compare well with the ERT and GPR profiles and the 3D-velocity cube serves as a good starting model for improved seismic reflection imaging.

Keywords: Drilling the Ivrea-Verbano zonE, Travel-time Tomography, active-source seismics, Geophysical Site Characterization.

Table of Contents

Abstract i

Table of Contents ii

List of Tables v

List of Figures vi

List of Abbreviations ix

1: Introduction 1

1.1 Motivation of the Study 1

1.2 Organization of Thesis 7

2: Geology of the IVZ 9

2.1 Tectonic Evolution of the IVZ 9

2.2 Lithostratigraphy and Structural Geology of the IVZ 10

2.3 Regional Setting and Val d'Ossola Geology 11

3: Seismic Tomography Theory, Programs, and Codes 13

3.1 Introduction 13

3.2 Seismic Tomography Theory 13

3.3 Other Inversion Methods 17

3.4 Associated Programs 19

4: Database 21

4.1 Introduction 21

4.2 Survey Set Up 24

4.3 Survey Geometry 28

5: Data Quality Assurance and Quality Control 33

5.1 Introduction 33

5.2 FBP QA/QC Methods 33

5.2.1 Vista FBP QA/QC Window 33

5.2.2 Matlab Travel Time QA/QC 35

5.3 Offset vs. First Break Picks 36

5.4 Root Mean Square Error Calculations 42

5.4.1 RMS Error Manual Calculation 42

5.4.2 Simulr16 RMS L-Curve Test 45

5.5 Simulr16 2D vs 2.5D 48

6: Results 49

6.1 Hard Rock and Soft Rock Cross-Line 2D Profiles 50

6.1.1 Soft Rock Cross Line Profile 50

6.1.2 Hard Rock Cross Line 52

6.2 In-Line 7 2D Profile 54

6.3 3D Survey Inversion Model 63

7: Discussion 69

7.1 Introduction 69

7.2 ERT Comparison to Seismic Velocity Inversion Model 71

7.3 Ground Penetrating Radar Comparison to Seismic Velocity Inversion Model 75

7.4 Comparison Conclusion 80

8: Concluding Remarks 82

8.1 Conclusions 82

8.2 Outlook.....83

References..... i

Appendix A (Extra Figures)..... vi

Appendix B (Matlab Codes) xiv

List of Tables

Table 1.1: IGFW Surveys ……..…….. 3

Table 4.1: Survey Parameters ……..…….…..…. 24

Table 5.1: In-Line 7 RMSE Utilizing the Shot Receiver Couples Calculation ……..…..... 44

Table 5.2: Model Comparison for Siumulr16 RMSE Calculation ……..……...… 47

Table 5.3: Simulr 2D vs 2.5D In-Line 7 Comparison …….……... 48

Table 6.1: Iterative Inversion Steps for Soft Rock Cross Line …….……. 50

Table 6.2: Iterative Inversion Steps for Hard Rock Cross Line ……. 52

Table 6.3: 2D High Velocity Profile Densification Grid ……..……..... 55

Table 6.4: 2D Low Velocity Profile Densification Grid ……..…….. 56

Table 6.5: Roll-on Statistics ……..……. 63

List of Figures

FIGURE 1.1- MAP VIEW OF IVZ …….. 2

FIGURE 1.2- THESIS WORKFLOW …….. 5

FIGURE 4.1- MAP VIEW OF SITE ……..…… 21

FIGURE 4.2- VELOCITIES OF SHOT 5001 FROM VISTA© ……..…….. 22

FIGURE 4.3- VELOCITES OF SHOT 5011 FROM VISTA© ……..…… 23

FIGURE 4.4- THEORIZED SUBSURFACE CALCULATIONS ……..... 23

FIGURE 4.5- SCHEMATIC OF SL, RL, AND CL ……... 25

FIGURE 4.6- SNAKE PATTERN SCHEMATIC ……. 26

FIGURE 4.7- IMAGE OF SHOT SWEEP ……..…. 28

FIGURE 4.8- SHOT 5001 AGC VS NO AGC IN VISTA© ……..... 29

FIGURE 4.9- SHOT 5001 AMPLITUDE SPECTRA IN VISTA© ……..….. 30

FIGURE 4.10- SHOT 5011 AGC VS NO AGC IN VISTA© …… 30

FIGURE 4.11- SHOT 5011 AMPLITUDE SPECTRA IN VISTA© ……..… 31

FIGURE 4.12- ENTIRE SURVEY AMPLITUDE SPECTRA IN VISTA© ……..…...… 32

FIGURE 5.1- QA/QC VISTA© WINDOW OF SHOT 10004 PRE-CORRECTION …...… 34

FIGURE 5.2- QA/QC VISTA© WINDOW OF SHOT 10004 POST CORRECTION 34

FIGURE 5.3- IL-7 OFFSET TRAVEL TIME QA/QC PRE-CORRECTIONS ….....…. 35

FIGURE 5.4- IL-7 OFFSET TRAVEL TIME QA/QC POST-CORRECTIONS ……. 36

FIGURE 5.5- SOFT ROCK CL FBP VS. OFFSET PRE-CORRECTION ……..... 37

FIGURE 5.6- HARD ROCK CL FBP VS. OFFSET PRE-CORRECTION ……..…..… 38

FIGURE 5.7- HARD ROCK & SOFT ROCK FBP VS. OFFSET POST CORRECTION ... 38

FIGURE 5.8- IL 7 FBP VS OFFSET PRE-CORRECTION ……...…..……...…. 39

FIGURE 5.9- IL 7 FBP VS OFFSET POST-CORRECTION ……..……. 40

FIGURE 5.10- FULL 3D SURVEY FBP VS OFFSET QC PRE-CORRECTION ……... 41

FIGURE 5.11- FULL 3D SURVEY FBP VS OFFSET QC CORRECTED …….…… 41

FIGURE 5.12- A SIMPLIFIED DIAGRAM OF THE RMSE SRC METHOD ……..... 43

FIGURE 5.13- L-CURVE OF IL7 DAMPING TEST ……... 46

FIGURE 5.14- GRAPH DISPLAY OF TABLE 4.2 …….. 47

FIGURE 6.1- MAP VIEW WITH 2D PROFILES LOCATED ……. 49

FIGURE 6.2- SOFT ROCK CL INITIAL INVERSION STEP ……..……... 51

FIGURE 6.3- SOFT ROCK CL FINAL INVERSION STEP ……..…….. 52

FIGURE 6.4- HARD ROCK CL INITIAL INVERSION STEP …..…….……. 53

FIGURE 6.5- HARD ROCK CL FINAL INVERSION STEP ……...… 54

FIGURE 6.6- INITIAL VELOCITY MODEL OF THE HVGD …… 57

FIGURE 6.7- HVGD 2nd DENSIFICATION STEP ……..... 58

FIGURE 6.8- HVGD 4th DENSIFICATION STEP …….……... 59

FIGURE 6.9- INITIAL VELOCITY MODEL OF THE LVGD ……...…. 60

FIGURE 6.10- LVGD 2nd DENSIFICATION STEP ……...….. 61

FIGURE 6.11- LVGD 4th DENSIFICATION STEP ……..…… 62

FIGURE 6.12- 3D FINAL INVERSION MODEL …… 64

FIGURE 6.13- IL3 OF 3D INVERSION MODEL ……..……. 65

FIGURE 6.14- IL 5 OF 3D INVERSION MODEL …….…….. 65

FIGURE 6.15- IL 7 OF 3D INVERSION MODEL ……...…… 66

FIGURE 6.16- IL 9 OF 3D INVERSION MODEL ……..…. 67

FIGURE 6.17- IL11 OF 3D INVERSION MODEL ……..… 67

FIGURE 6.18- IL14 OF 3D INVERSION MODEL ……..…… 68

FIGURE 7.1- IGFW REPORT ERT GPS LOCATIONS ……..…… 69

FIGURE 7.2- IGFW REPORT GPR GPS LOCATIONS …….. 70

FIGURE 7.3- MODIFIED FIGURE 5.10 …….…….. 71

FIGURE 7.4- VERTICAL ERT PROFILES ……..…… 72

FIGURE 7.5- 237M 2D ERT PROFILE LINE ……... 73

FIGURE 7.6- 6 DEPTH ERT PROFILES ……..… 73

FIGURE 7.7- ERT VS VEGETATION IMAGE …… 74

FIGURE 7.8- 25 MHz GPR LINE09 …….. 77

FIGURE 7.9- 100 MHz GPR LINE10 ……..….. 78

FIGURE 7.10- 250 MHz GPR LINE18 ……..… 79

List of Abbreviations

AGC …….….. Automatic Gain Control

ART/PB ……. Approximate Ray Tracing/Pseudo Bending

BFL ……...… Best Fit Line

bld ……... Forward Grid Spacing

CL …….. Cross-Line

DIVE …...…... Drilling the Ivrea-Verbano zone

DLS …… Damped Least Squares

EM …….. Electromagnetic

ERT …… Electric Resistivity Tomography

ElViS-VII ….. Electrodynamic-Vibrator-System 7

FBP …… First Break Picks

FD …….. Finite Difference

GPR ……... Ground Penetrating Radar

Hz ……... Hertz

HVGD …… High Velocity Grid Densification

ICDP ……. International Continental Scientific Drilling Program

IGFW ……. Integrated Geophysical Field Workshop

IL ……... In-Line

IMW …….. Ivrea Mantle Wedge

IVZ ……. Ivrea-Verbano Zone

Kg …….. Kilogram

LVGD …… Low Velocity Grid Densification

M …… Meter

Ma ……..… One Million Years

MCMC ……. Markov Chain Monte Carlo

mGal …….. Milligals

MHz ……..… Megahertz

Ms …….. milliseconds

mS/m ……… milliSiemens per meter

Myr ……..... Million Years

P-wave …… Pressure Wave

QA ……..... Quality Assurance

QC ……..... Quality Control

RL …….. Receiver-Line

RMSE …..…. Root Mean Square Error

ROCH …….. Roll-On Channel

ROL …….. Roll-On Line

RTK …….. Real-Time Kinematic

RU ……..... Remote Unit

SL …….. Shot-Line

SRC ……... Shot Receiver Couple

SSRD …… Source Sweep Recording Device

SXDC …… Summit X One DC Seismographs

TS …….. Trigger Signal

TZ …….. Transition Zone

1: Introduction

1.1 Motivation of the Study

A week-long geophysical field course known as the Integrated Geophysical Field Workshop (IGFW), is organized by the Chair of Applied Geophysics of Montanuniversitat, Leoben as part of the International Masters in Applied and Exploration Geophysics. During the 2022 IGFW a 3D reflection seismic survey and other geophysical methods were conducted to characterize the International Scientific Continental Drilling Program (ICDP)-Drilling the Ivrea Verbano zonE (DIVE) DT-1B drill site prior to drilling. The team consisted of Masters and PhD students of Montanuniversität Leoben led by Dr. Andrew Greenwood, Assoz. Prof. Robert Scholger, and Dr. Baron of The University of Lausanne. The field course ran the final week of April of 2022.

The DT-1B drilling site is located in Ornavasso, Val d'Ossola Italy, 8 km from the Insubric Line in the Ivrea Verbano Zone (IVZ). The IVZ is a unique place on the earth's crust, and is a region of significant geological interest due to deep crustal segments that have been uplifted to shallow depths. Because of this uniqueness, the region has been heavily investigated and continues to be the target of many scientific studies. One of these, DIVE, is a multi-national research consortium formed to gather data from boreholes in the IVZ. The main objective of DIVE is to characterize geologically, geophysically, and geochemically Lower Crustal Rocks and the transition to Mantel Rocks by creating rock cores for scientific testing. In order to achieve this, 3 boreholes placed in key locations in the IVZ have been planned, specifically two 1-kilometer-deep boreholes: the DT-1A and DT-1B in Megolo and Ornavasso in the Val d'Ossola, and a proposed second phase 4-kilometer-deep borehole: the DT-2 in Balmuccia, in

Val Sesia. The drilling of DIVE is funded by the ICDP, alongside several national science organizations and agencies (Pistone et al 2017). The planned locations of the first phase boreholes in relation to the IVZ are shown in Figure 1.1.

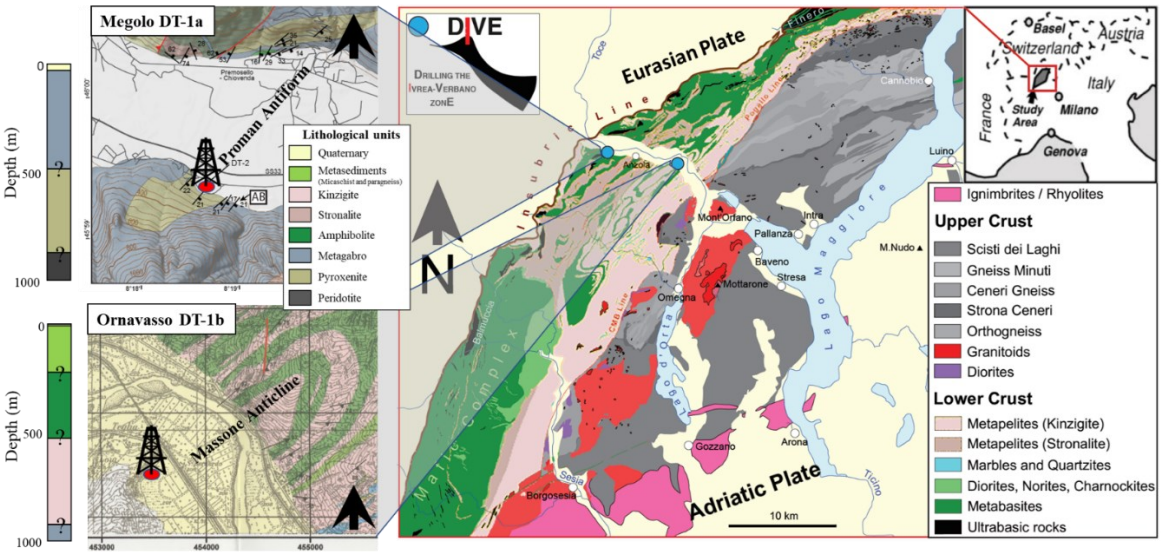

Figure 1.1*: Map view of the IVZ with the planned locations for the boreholes planned for the first phase of DIVE. Most important to this Thesis is the DT-1b drill site which is the focal point of this Thesis. (Pistone et al 2017).*

Stated goals of DIVE are: to improve the understanding of the processes that create and alter the lower continental crust and the mantle transition zone known as the Moho. To study in situ transitions between peridotite and metasedimentary or gabbroic rock. To characterize the physical properties of the drilled sections to improve techniques for the identification of seismic reflectors and understanding their nature. Studying the beginnings of the serpentinization process commonly found near tectonic plate boundaries, which coincides with the study of fluid-rock interaction, fluid flow, and permeability in shear zones and faults. Exploring the sites and conditions that host microbial life in planetary interiors, the earth's hydrosphere and atmosphere, and geochemical organic synthesis at depths. Comprehensive, direct, and downhole geophysical monitoring of seismicity, evaluation of seismic hazards near the suture zone of the alpine orogeny, alongside geothermal energy exploration. And finally, to develop an educational research center in the IVZ (Pistone et al 2017). DT-1B, the

lithologically shallowest of the three planned boreholes, aims to drill into the upper-lower crust in order to characterize lower crustal rocks above the Moho transition.

The geophysical methods used during the IGFW were designed to investigate the upper 10 m of the area with a goal to characterize the DIVE DT-1B borehole site to detect any near surface anomalies that may inhibit or complicate drilling operations. Anomalies could include: boulders that previously collapsed from the cliff face, and are subsequently buried in the quaternary sediment, or anthropogenic artefacts due to millennia of human inhabitation in North-Western Italy. These anomalies would prohibit or slow down the drilling process and increase costs.

In addition to the 3D P-wave survey, 3D Ground Penetrating Radar (GPR) and Electric Resistivity Tomography (ERT) surveys were conducted. The 3D P-wave survey is designed to be shallow and high-resolution. This survey is the main focus of this Thesis. Table 1.1 contains all of the surveys conducted during the IGFW.

Table 1.1 *IGFW Surveys*

Geophysical Method	Seismic Survey	GPR Survey	ERT Survey
Survey Design/Frequency	3D P-Wave	3D 250 MHz 3D 100 MHz 3D 25 MHz	2D Wenner 2D Dipole-Dipole 3D Wenner Alpha 3D Wenner-Beta 3D Gradient
Dimensions	45x45 m	50 x 1 m 25 x 2 m 25 x 2 m	237 m Profile 40 m x 50 m

All of the GPR grids and the ERT 3D grid occupy the same location of the 3D P-wave survey. Because of the overlapping of all three of the geophysical surveys, the results of the inversion

process produced in this Thesis can and will be compared to the results from the ERT and GPR.

The objective of this Thesis is to create a velocity model from the 3D P-Wave seismic survey data collected as part of the IGFW and to characterize the subsurface lithologies (the hard rocks and soft rocks) within the survey area. This hard rock vs soft rock interface, is designated within the Thesis as the Transition Zone (TZ). Where do the lithologies transition into one another within the DT-1B drill site, and how does the seismic survey compare in identifying this TZ versus the GPR and ERT data gathered during IGFW. The velocity model is generated using the Simulr16 program (Bleibinhaus., 2003). The velocity model is then compared to the 2D and 3D ERT surveys, and the 3D GPR surveys that were gathered during the IGFW. Figure 1.2 displays the workflow of the Thesis.

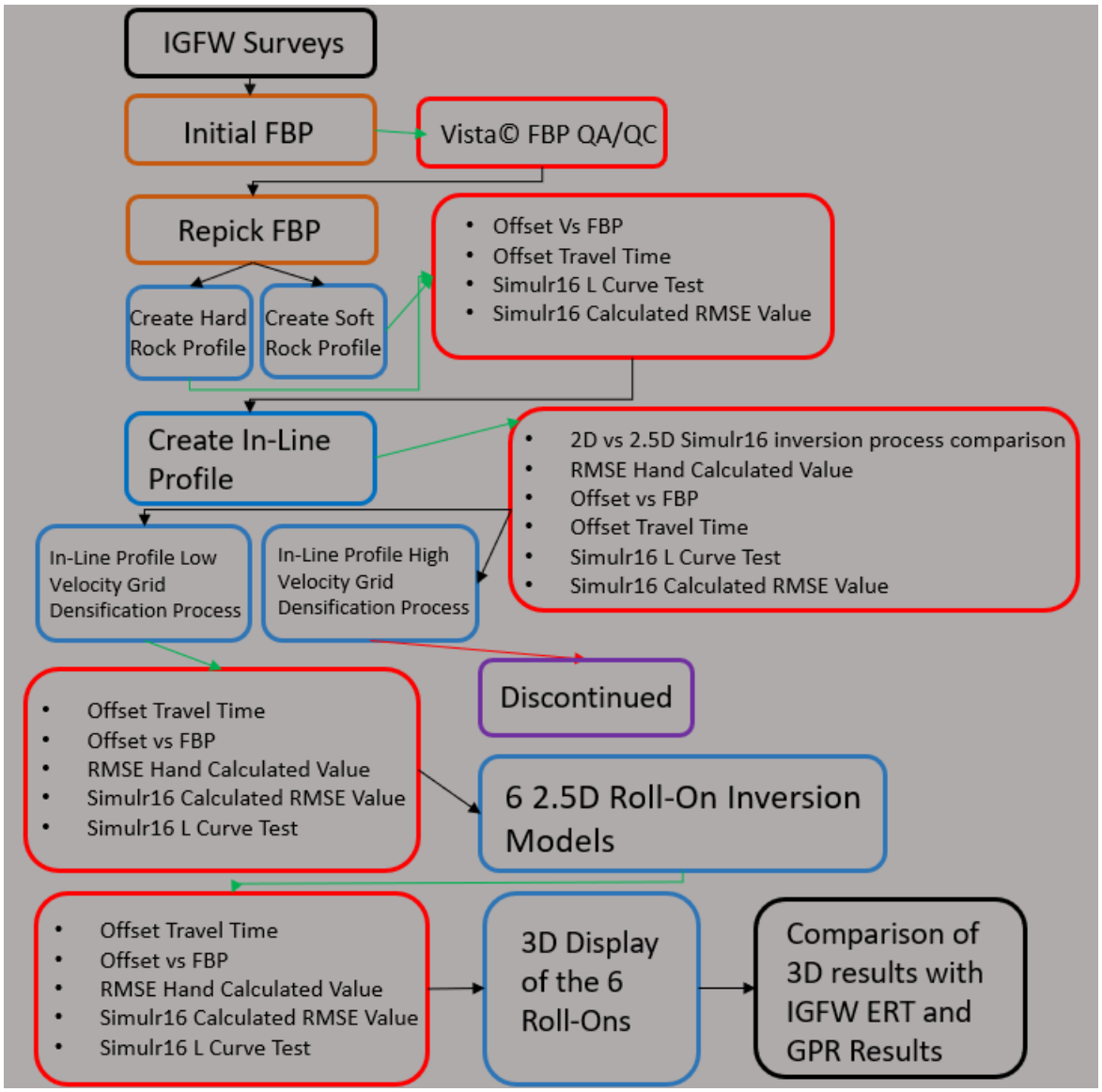

***Figure 1.2**: This Figure displays the workflow of the Thesis. The black rectangles represent the beginning and end of the Thesis. The Orange rectangles represent First Break Picking (FBP) steps of the Thesis. Red rectangles represent Quality Assurance (QA) and Quality Control (QC) steps of the Thesis. Blue Rectangles represent steps where a profile, or profiles undergo the inversion process. The purple rectangle represents a discontinued inversion process result. Green arrows always flow from an inversion process step to a QA/QC step. Black Arrows flow to either inversion process steps, FBP steps, or results. The sole red arrow flows from an inversion process step to a discontinued result.*

Each of the Geophysical methods utilized in the IGFW and this Thesis interact with the subsurface lithologies differently. This makes every geophysical survey inherently unique, however each survey has similar modelling issues and advantages, with each of the methods depending upon the lithological contrasts located within the site. The following literature review brings to light issues that might develop later in the Thesis.

ERT has been proven to provide the best results for determining sediment changes and detecting boundaries, however the locations of those boundaries can be blurred due to smoothness constraints (Hirsch., 2008). In karstic regions ERT is effective in mapping shallow subsurface features. However, it has limitations in modelling including: extensive resistivity ranges, identifying fractures, and solid rocks. Model uncertainties for identifying bedrock and unconsolidated materials are related to the large ranges of resistivities of the karstic materials, and ERT cannot identify individual karstic fractures (Tao., 2021). Areas that demonstrate high resistivity, in ERT, but also lack high amplitude GPR reflections are indicative of no significant dielectric contrasts caused by gradual change in rock character from weathered to hard rock mass (Butchibabu., 2021). Regions of interbedded clays, sands, and gravels cause low resistivity anomalies in ERT surveys, due to the higher water content. This makes distinguishing the higher resistivity of loose and semi compacted regions from clay rich regions in segments of combined data easier (Gołębiowski., 2022).

GPR provides the highest resolution and provides information on internal structures. This is offset due to the fact that the GPR signal is severely attenuated in regions of excessive conductivity caused by fine grained clay particles (Hirsch., 2008). Karstic lithologies which display large variations in component soil electromagnetic (EM) propagation velocities, have fractures, and solid rocks interbedded with newer unconsolidated sediments also exhibit uncertainties in modelling. Fractures in the bedrock with apertures smaller than the dominant wavelength of the GPR, or in beds thinner than the Rayleigh resolution limit, will not be imaged. However higher frequency GPR, such as 500 MHz, will image fractures in shallow layers less than 4 m (Tao., 2021). Interbedded clays with sand and gravel will raise the moisture content raising the conductivity and creating higher attenuation for GPR surveys. This can cause an extreme loss of depth penetration for GPR from an estimated 15 m down to 1.5-2 m in depth (Gołębiowski., 2022).

Seismic Refraction inversion processes can reproduce bedrock interfaces; however, it has issues detecting compositional changes in surficial sediments, and can require a possibly non-existent low velocity surface layer to represent a change in shallow depth sediments (Hirsch., 2008). It is acknowledged that refraction methods are poorly sensitive to shallow low velocity zones (Owoc., 2019). Places of interbedded sands and clays on sites of levees show a less evident reflection in seismic surveys, acting as a signal layer/area (Gołębiowski., 2022).

Hirsch (2008) targeted river deposited sediments, unlike the crystalline basement rock and quaternary deposits of the DT-1B drill site. If the quaternary deposits of the DT-1B drill site are in some way deposits resultant from the nearby Toce River, interbedding of sands and gravels with clays will result in discrepancies between the GPR and ERT similar to that of surveys conducted on levees in Gołębiowski (2022). Meanwhile Tao (2021) did not utilize seismic refraction in their overall comparison of the Karstic region, so one might theorize that the modelling uncertainties mentioned in their study will not be evident in comparison with DT-1B seismic data. However, it is quite possible the crystalline bedrock will have fractures from the uplift process that formed the IVZ. The detection of these fractures is likely to be infeasible due to the comparatively low frequencies, 25-250 MHz, utilized in the IGFW GPR surveys. Due to quaternary sediment's small lithological variation, regardless of origin or age, their spatial recognition and interpretation is hindered in seismic results (Owoc., 2019). This could affect the resultant inversion model of seismic survey data due to the large presence of quaternary sediments within the DT-1B site.

1.2 Organization of Thesis

The Thesis is formed from eight chapters. Chapter 1 introduces the motivation behind the Thesis, the goals of DIVE and the IGFW, as well as the work flow of the Thesis.

Chapter 2 develops the tectonic evolution of the IVZ, the geology and lithology of the IVZ, and finally zooms into the geology of the Val d'Ossola and the DT-1B drill site.

Chapter 3 delves through the basic theory of Damped Least Squares Seismic Tomography, and briefly mentions other popular inversion methods. It also discusses the computer programs and codes utilized during the Thesis, and the process of using several codes and programs in a workflow to create a 3-dimensional velocity model of the DT-1b drill site.

Chapter 4 discusses the survey geometry, the survey layout, and roll-along sequence. To clarify questions about topics discussed in this chapter images have been generated to help readers better understand the functionality of how the survey works.

Chapter 5 explores the varied methods utilized to perform Quality Assurance and Quality Control during the processing work-flow. These methods include codes generated in Matlab, spreadsheet calculations, and retesting data.

Chapter 6 presents the final results of three 2D velocity models cutting through different sections of the survey grid. It also discusses the grid densification process that is utilized to create the final 2D model through the centre of the survey grid, which is subsequently used to create the 3D starting model. It then displays the node densification steps and the completed 3D velocity models of the survey.

Chapter 7 discusses the strengths and weaknesses of the method and of the Thesis. It also compares the results of the 3D inversion process with the ERT and GPR 3D surveys that were collected during the IGFW.

Chapter 8 is concluding remarks, and possible future work.

2: Geology of the IVZ

2.1 Tectonic Evolution of the IVZ

The IVZ is located in the Western Alpine Arc which began to form approximately 35 Myr ago. This is caused by the Adriatic plate converging and colliding with the European Foreland portion of the Eurasian plate (Schmid., 2000). This orogenic event “features a west directed thrusting movement of the Adriatic Microplate relative to the stable European Plate”. This crustal shortening occurred in three episodes (Schmid., 2017). The first event (Late Cretaceous to 35 Ma) displaced at least 250 km, is characterized by “North-Northwest sinistral transpression”, and “strikes from the Central and Eastern Alps and the Adriatic Microplate towards the North Northwest with respect to the stable European Plate”. The second stage occurred from 35 to 25 Ma entailing 100-150 km of shortening displacement concentrated along the Penninic frontal thrust. This displacement is “characterized by lateral indentation of Adria, including the Ivrea Mantle Wedge (IMW) towards the West-Northwest”. This is combined with “underthrusting of the IMW below the Western Alpine Nappe Pile”. Finally, the third event (25-0 Ma) is associated with the Apennine Orogeny, which led to “orthoclinal bending in the southernmost Western Alps”. This happened simultaneously with a “50-degree counter-clockwise rotation of the Corsica-Sardinia block”. (Schmid., 2017).

The IVZ is interpreted to have formed during the second episode of shortening (Schmid., 2000). The IVZ is exhumed to a shallow crustal depth due to the “Jurassic rifting at the passive continental margin of the Adriatic Continent”. At this point it acted as a high strength wedge, due to it being comprised of denser stronger mantle rocks, and “controlled the lateral ends of indentation near the Cueno and Rhone-Simplon faults” (Schmid., 2017). Based on the geometry gathered from controlled source seismology the crust and mantle of the Adriatic

Microplate that forms the IVZ became “wedged into the alpine edifice and underplated shallow crustal layers in the internal Alps” (Schmid., 2017). Despite this extensive, drastic, tectonic activity, and exhumation nearly complete sections of the continental crust are preserved to the extent that the IVZ offers the most complete continental crustal cross section in the world (Pistone., et al 2020).

2.2 Lithostratigraphy and Structural Geology of the IVZ

The IVZ itself can be described as a “sub-vertical cross section through the pre-alpine deep continental crust, tilted along a north-northeast axis”. It is a unique location for analyzing a complete continental crust section from the base to the surface (Pistone., et al 2020). While the IVZ is *relatively* un-metamorphosed it has undergone: local rifting related magmatism, subduction related fluid influx, and tectonic related thermal perturbations ranging between 550°-700°C. This thermal stage concluded with a <300°C continental geotherm starting around 100 Ma for the final exhumation during the Alpine Orogeny (Pistone., et al 2020).

A general statement of the geology of the IVZ and upper IGB can be described as being dominated by plagioclase for a combined thickness of approximately 48 km. Combined the IVZ and IGB are considered as being “a complete record of the early Permian continental crust” which is laid on top the lower body of the IGB which is composed of pyroxene hornblendite (Pistone., et al 2020).

In more detail, the Southwest portion including the entire Insubric fault connection is a mafic complex with interspersed peridotite bodies. A significantly larger peridotite body, known as the Balmuccia Peridotite, is located on the North West border of the Insubric Fault. This peridotite body has had its eastern edge described as an exposed petrologic Moho (Quick., 1995). For reference a “Petrologic Moho” corresponds to the depth, in the earth’s crust, where

plagioclase no longer forms in the crystalline structures that form within mafic magmas. This differs from the "Geophysical Moho" that is the depth in the earth's crust where p-wave velocities almost instantly change from a standard of 7 km/s to 8 km/s (Pistone., 2020).

2.3 Regional Setting and Val d'Ossola Geology

From the west to the northwest of the IVZ is the Insubric Fault which separates it from the Alpine metamorphic rocks of the Canavese Zone (Brodie., 1987). The Canavese Zone combined with the IVZ and the Southern Alps form the upper plate of the Alpine orogen. These two zones are of non-metamorphic nature and lay alongside exhumed mantle rocks overlain by Jurassic age radiolarities (Schmid., 2017). The Canavese Zone is considered to be the root of the highest nappe exposed in the Prealpes Romandes. Meanwhile profiles to the south include thin slices of the IMW and lower crustal lithologies of the Ivrea that reach the surface, however the main body of the IMW is below a depth of 10 km with the base of the IMW above the subduction channel (Schmid., 2017).

The IVZ is bordered by the Pogallo Line to the southeast which separates it from the Strona-Ceneri Zone, which is dominated by upper greenschist to mid-amphibolite facies, orthogneisses, paragneisses, and schists (Brodie., 1987). It is theorized, due to radiometric testing, that the Pogallo Line is a pre-Alpine orogeny low angle, crustal thinning, extensional fault zone dating to the Late Permian or Early Jurassic (Pistone., et al 2020).

Located at an average of 200 meters above sea level the Val d'Ossola is a uniform levelled valley with minimal bedrock exposure. The Toce river flows through the valley and feeds into the nearby Lago Maggiore, depositing clastic sediments, a possible source of the quaternary sediment lithology in the valley and DT-1B drill site. It is dominated by two large antiformal structures that range from acute to isoclinal in angularity. Both of which are formed with approximately 4 km wavelengths, possess steep axial surfaces, and folds the regional banding. Neither of these structures have well developed syn-formal structures, and of the two the

northern structure is younger. The southern antiform structure plunges gently to the northeast and has a parallel trend with the lineation of the local valley wide gneisses. Located in the core of the northern antiformal structure are high grade metabasic rocks such as garnet and calcic plagioclase granulites (Brodie., 1987). DT-1B is located within the Val d'Ossola on the hinge zone of the tightly folded Massone Antiform. Deformation and erosion in this zone have created to the Northwest of the survey a cliff face that is composed of Kinzigite and Stronalite, which are garnet biotite gneisses that occur in granulite facies (AGI 1960). These units are theorized to extend deeper into the subsurface and farther to the Southeast. To the Southeast of the cliff face, deep quaternary sedimentary deposits have buried the remnant of the cliff, and dominate the survey area.

3: Seismic Tomography Theory, Programs, and Codes

3.1 Introduction

This Chapter discusses Seismic Tomography Theory, the various programs, and the codes used and written for the Thesis. This Thesis heavily relies upon three different programs to complete the work; however, several other programs were utilized to generate images. The three main programs utilized are VISTA©, Matlab, and Simulr16. Several of the image generating programs include Microsoft PowerPoint and Google Earth. For seismic trace sorting, geometry, picking of the first arrival times, and the first Quality Assurance (QA) and Quality Control (QC) controls is performed in VISTA©. Several QA/QC and data translation necessary for moving information from VISTA© to Simulr16 codes were written in Matlab. Simulr16 is a Fortran coded Seismic Tomography Inversion program, which is run on Linux. Simulr16 is the program utilized for the inversion process to generate the velocity models in the Thesis. Simulr16 uses The Damped Least-Squares method of inversion and is represented in equations 3.1 through 3.9. While Simulr16, and thus this Thesis, utilizes the Damped Least Squares (DLS) method of inversion several other popular and effective methods of inversion deserve a brief discussion.

3.2 Seismic Tomography Theory

Seismic Tomography is a subsurface imaging technique which utilizes either earthquake or man-made generated seismic waves to produce 2D and 3D velocity models of the subsurface. This is accomplished by utilizing P-wave travel times from multiple shot and receiver

locations to generate a velocity model of the subsurface. Seismic Tomography treats propagating wave energy from the source to the receiver, as traveling along an infinitesimally small ray path, not propagating as a contiguous wave front. This is known as Geometric Ray Theory (Rawlinson., 2003). The travel time of the propagating wave is calculated with the equation:

$$\mathbf{t = \int_l v^{-1}(x(l))dl} \tag{3.1}$$

where t is the ray travel time, l is the ray trajectory, and $v(x)$ is the velocity in x. Seismic Tomography is applicable in surveys ranging from the sub meter scale of laboratory experiments, meter scaled (for survey sites), and up to global scales, to image the Mantle and Core. An approximate relationship between the measured seismic data (d) and the velocity model parameters (m) for a linear problem is defined as:

$$\mathbf{d = Gm} \tag{3.2}$$

where G is a matrix representing equations of the system data. The seismic data d can be separated into two groups the observed data (d_{obs}) which includes the noise η and the true data known as (d_{true}). Almost all geophysics systems are non-linear, which means that it has either failed the Superposition Law or the Scaling Law. The Damped Least Squares method is utilized to solve non-linear inversion problems. The Superposition Law is defined as:

$$\mathbf{G(m_1 + m_2) = G(m_1)+G(m_2)} \tag{3.3}$$

where the net reaction of two or more catalysts is equal to the sum of the reactions from each individual catalyst. The Scaling Law is defined as:

$$\mathbf{G(am) = aG(m)} \tag{3.4}$$

where the sum of a scalar inside the matrix is equal to the sum of the scalar outside the matrix.

Exactly determined problems are those in which the measured data illuminates all model parameters, there is a unique solution with a null data misfit value, and a null prediction error. This is represented by the equation:

$$\mathbf{m} = (\boldsymbol{G^T G})^{-1}\boldsymbol{G^T d} \tag{3.5}$$

where $\boldsymbol{G^T}$ is the transpose of the $\boldsymbol{G}$ Jacobian matrix. The Jacobian Matrix contains partial derivatives of data with respect to the initial model parameters (Maiti., 2012). This is the exact solution for noiseless data. An overdetermined problem is a non-isolated system (therefore a system with noise) where, $\boldsymbol{n}$ (the number of measured data $\boldsymbol{d}$ samples) is larger than $\boldsymbol{p}$ (the number of defined positions in the model $\boldsymbol{m}$). In this case noisy data is conditioned to a least-squares error to calculate an ideal solution using:

$$\boldsymbol{min}(\|\boldsymbol{Gm} - (\boldsymbol{d_{true}} + \boldsymbol{\eta})\|_2) = \boldsymbol{min}(\|\boldsymbol{Gm} - \boldsymbol{d_{obs}}\|_2) \tag{3.6}$$

An underdetermined problem is where $\boldsymbol{n}$ is smaller than $\boldsymbol{p}$, and a minute number of solutions exist. Every parameter that can be determined as noise is not modelled and there exist many satisfactory solutions to a threshold $\boldsymbol{\delta}$:

$$\mathbf{min}(\|\mathbf{Gm} - \mathbf{d_{obs}}\|_2) \leq \boldsymbol{\delta} \tag{3.7}$$

The Data and models are affected by different uncertainties; however, we wish the linear regression be mainly driven by data affected by low uncertainty. Thus, we can weight each data residual differently. The most popular weighting method is known as the L2-norm and is represented as:

$$\mathbf{m} = (\boldsymbol{G^T Cd^{-1} G})^{-1}\boldsymbol{G^T Cd^{-1} d} \tag{3.8}$$

where $\boldsymbol{Cd}$ represents a matrix that is the inverse of the data covariance matrix. The L2-norm is denoted by the $\|(..)\|_2$ in equations (3.6) and (3.7).

Zero Order Tikhonov Regularization is a solution to minimization problems where the matrix operator is the identity matrix and the amplitude of epicardial estimates are penalized (Lowther 2001). The Zero Order Tikhonov Regularization is also known as The Damped Least-Squares method and its equation is:

$$\mathbf{m} = (\boldsymbol{G^T G} + \phi \boldsymbol{I})^{-1} \boldsymbol{G^T d} \tag{3.9}$$

where $\boldsymbol{I}$ represents the Identity Matrix, $\boldsymbol{G}$ is the Jacobian Matrix, and $\boldsymbol{\phi}$ is the damping parameter representing the L-curve criterion. This is used to located the "knee point" of the L-curve, or the trade-off curve. The trade-off curve involves multiple inversions steps to be run for increasing values of $\boldsymbol{\phi}$. The trade-off curve is then built by representing the L2 norm of the data misfit versus the L2 norm of the model penalty vector. For high $\boldsymbol{\phi}$ values the curve tends toward low values of the model norm at the expense of an increased data misfit value. For low $\boldsymbol{\phi}$ values the inversion process provides optimal data prediction, but increased model norm. The optimal $\boldsymbol{\phi}$ value is determined from the "knee point" of the curve that constitutes a good compromise between data prediction and model reconstruction. In equation (3.9) $\boldsymbol{\phi}$ is a scalar that controls the speed and convergence of the inversion process, and is known as the Tikhonov regularization (Maiti., 2012).

Computer generated models created by utilizing subsurface velocity contrasts from non-homogeneous lithological differences are the intended goal of seismic tomography. Seismic waves interact with such velocity contrasts and create refractions and reflections of the ray paths which form the geometric ray theory. As a result of the travel times being dependent upon the paths of the rays and the paths of the rays being dependent upon the velocity model, seismic tomography is a non-linear inverse problem. A Priori information (information that is previously known) is an important tool in seismic tomography to set limits and constraints on models. A well constrained model will be able to identify probable global minimum for the

inverse problem, and non-linear problems can be compared and solved similarly to a linear problem.

3.3 Other Inversion Methods

The Markov Chain Monte Carlo (MCMC), which is a technique where the use of random numbers to solve inversion problems that are deterministic or probabilistic in nature (Sambridge., 2011). This method is the inversion of choice for Bayesian inversions conducted on non-linear problems. A Bayesian approach to inversion problems is that there is not a real model, but each model parameter is considered as a random realization drawn from a given distribution, and the achieved solution is a probability distribution on the model space (Dashti., 2017). The MCMC is a pseudorandom sampling model method that produces a model which points to the minimum global and reduces the non-uniqueness effect of said minimum (Haerudin., 2021). One of the strengths of the MCMC is that it does have significantly less optimization issues than other methods. This is due to the MCMC not relying upon objective functions being smooth, nor does the MCMC include potentially numerically unstable processes like matrix inversions (Sambridge., 2002). Several of its weaknesses are that it is comparably slower if the random model is inefficient, and if gradient methods are utilized in conjunction with the MCMC the possibility of no solution being determined is a non-zero outcome, due to the chance of a complete iterative inversion failure (Sambridge., 2002). The most simple MCMC randomized sampling equation for a parameter space is:

$$\boldsymbol{x_i} = \sum_{\boldsymbol{i=1}}^{\boldsymbol{d}} \boldsymbol{r_i e_i} \tag{3.10}$$

where $\boldsymbol{e_i}$ is the unit vector along the $\boldsymbol{I}$ axis in the parameter space, and $\boldsymbol{r_i}$ is a random number that lies within the range of (0,1) (Sambridge., 2002).

Another method of Inversion is the Grid Search. In this method the subsurface is divided into rectangular grids of fixed equal dimensions but with the sought-after parameter (density, velocity, etc) unknown (Grandis., 2014). Each sample subdivision is then calculated by a linear inversion process, and if the latest subdivision has the lowest error value, it is then set as the limit. The inversion process will continue until all grids are calculated and the grid with the smallest Root Mean Square will be the best solution (Pramudya., 2021). Several downsides to this method include mandatory limited model parameters, an inverted ability to find the global minimum as the number of unknowns increases, and the error function must be smooth with respect to distance between grid squares. This is because the more the model parameters expand the greater the computation time and cost increases (Shan., 2007). The benefits to this method include it being less influenced by multiple minima, it does not require the computation of a matrix inverse, nor the computation of a gradient of the objective function.

The final method of inversion to be discussed will be Gauss-Newton Inversion. This method uses a Taylor series expansion of initial parameters to linearize the model equation so that only the first order partial derivatives are considered (Scherzer., 2023). One of the major drawbacks of the Gauss-Newton method is the need to invert a square Hessian matrix that has both dimensions equal to the number of model parameters. A Hessian matrix is a square matrix of second order derivatives of the objective function that maps errors from data space onto model space (Lewis., 1991). The square Hessian matrix is an issue due to the fact that the model parameters, in modern inversion applications, can number in the millions (Gribenko., 2017). Other drawbacks to this method are that it is prone to getting trapped at local minima, thus not discovering global minima, and that it requires a well-defined starting model. The benefits to this method are that in regards to a linear model it will find the minima

in a single iteration, and even in those nonlinear problems with a good initial model, convergence can still be rapid (Huang., 2010).

3.4 Associated Programs

Matlab is an advanced programming language that is proficient in the use of algorithms for the approximation of mathematical analysis problems. In this thesis multiple Matlab codes were written to include: translating data between two programs, QA and QC methods, and gridding routines for the velocity model grid refinement process required for inversion.

VISTA© is a seismic data processing software from Schlumberger that can be used for early acquisition to final processing. In the thesis Vista is utilized for data, stacking, first break picking, QA/QC and the generation of SEGY files required for Simulr16. SEGY is a standard geophysical data storage file format, which was developed by the Society of Exploration Geophysicists in 1973 (Hagelund., 2023). Multiple different files were generated in VISTA© that were used in Matlab to perform QA/QC of the picked travel-time data.

Simulr16 is developed for crustal scale refraction and reflection seismics. It is based upon Simul by (Thurber., 1983). The forward and inverse models' parameterization are identical. Velocities are calculated iteratively until designated criteria halt the process. Approximate Ray Tracing/Pseudo Bending (ART/PB) is the method utilized for Forward Modelling in Simulr16, and in the modification from (Thurber., 1983) the ART/PB has been extended to take into consideration elliptical anisotropy and to model reflection travel times (Bleibinhaus., 2003). The cost function, of Simulr16, for inverting seismic waves is:

$$\mathbf{E} = \mathbf{e^T W_d e} + \boldsymbol{\theta}^2 \boldsymbol{\Delta} \mathbf{m^T} \boldsymbol{\Delta} \mathbf{m}$$

Where **e** represents data misfit and $\boldsymbol{W_d}$ represents data weighting which is a diagonal matrix with the inverse variances. These values range from 0-3 where 3 is the lowest quality factor.

(Bleibinhaus., 2003). It uses an isotropic eikonal solver based upon (Holt., 1995) for increased accuracy computing travel times and ray paths (Bleibinhaus., 2003).

The four inversion processes in this thesis, the three 2D profiles and the complete 3D, were conducted using this program. The In-Line 2D profile has different starting models attempts for the inversion process to include: multiple models, multiple starting velocity models, a 2.5D vs. 2D, and finally a grid densification process, in order to better define the starting 3D inversion model.

Four obligatory data files are required to parameterize Simulr16, these are SHOT, STNS, CNTL, and MOD. The SHOT and STNS files define the geometry of the seismic source and receivers by taking the GPS data from the SEGY of VISTA© and formatting it properly for the inversion process of Simulr16. The CNTL file controls the inversion parameters, such as, number of iterations, 2D vs 3D, and damping value. The MOD file establishes the starting model of the inversion, whereby the velocity gradient, node coordinates, and node spacing are defined. Three different co-existing grids are defined in MOD: Finite-Difference (FD) grid, the forward ART/PB grid, and the inversion grid. The FD grid is necessary for the eikonal ray-tracer and its spacing is chosen by the user in the MOD file. The forward grid is a sparce rectangular grid whose axes spacing is chosen according to the ray density. The inversion grid is a copy of the forward grid where most, but not all, parameters are inverted. According to (Bleibinhaus., 2003) the Simulr16 starting model's forward grid seismic velocities are defined at the intersections of arbitrarily spaced x/y/z-planes. In between intersections the velocity is computed through the tri-linear interpolation:

$$\boldsymbol{v(x,y,z) = \Sigma_{l=i}^{i+1}\Sigma_{m=j}^{j+1}\Sigma_{n=k}^{k+1} v(l,m,n)\left[\left(1-\frac{|x-x_l|}{x_{i+1}-x_i}\right)\left(1-\frac{|y-y_m|}{y_{j+1}-y_j}\right)\left(1-\frac{|z-z_n|}{z_{k+1}-z_k}\right)\right]}$$

4: Database

4.1 Introduction

A map view of the DT-1B drill site, indicating the In-Lines, Cross-Lines, Receiver Lines, Shot Lines, the source and receiver GPS locations, the Hard Rock Cross-Line profile, the Soft Rock Cross-Line profile, and the In-Line 7/Shot Line 8 (IL7SL8) profile, their relation to the entire survey, the proposed and finalized drill site, and a hypothetical Hard Rock vs. Soft Rock overlay based upon vegetation growth is shown in Figure 4.1.

Figure 4.1*: Map view of the survey site [Image @ 2023 Maxar Technologies]. The black arrow points to north for reference. The grey arrow indicates the footpath to the Southeast of the survey. The beige arrow refers to the hard rock cliff that dominates the Northwest of the survey area. Blue circles are the GPS coordinates of the receiving geophones. The blue arrow indicates the beginning of In-Line 3. Red circles are the GPS coordinates of the shot locations. Red Arrow indicates the end of Cross-Line 7. Included in this figure is a rough diagram of the survey and the locations of the three proposed 2D profiles, the proposed location (the green circle) and final location (the yellow circle) of the DT-1B borehole. A Hard Rock Cross Line profile, a Soft Rock Cross Line profile, and the IL7SL8 2D profile are all indicated by the red lines. It also shows a hypothetical subsurface lithological division of the survey area based upon vegetation growth from water supply. The yellow overlay indicates what is theorized to be hard rock in the subsurface in this image due to the drier grass. The cause of this is the harder rock prevents a shallow water table and any rainwater quickly runs downhill. The green*

overlay indicates the soft sedimentary deposits which has a shallower water table allowing lusher grass growth and pooling water runoff from the cliff face and hard rock to the Northwest. The black line within the survey area represents the theoretical TZ.

The TZ is notable because it complicates accurate first break picking, the RMSE calculations, and the inversion processes. The TZ is not a continuous flat plane throughout the survey. Its proposed angle and horizontal location on each individual SL and RL vary. Figures 4.2 and 4.3 show two different shot points, 5001 in the soft rock for Figure 4.2, and 50011 in the hard rock for Figure 4.3, and the velocity estimation of the lithologies of the DT-1B drill site. Figure 4.4 provides the theorized subsurface of the survey area and critical angle calculations using a priori data gathered from the IGFW surveys and velocities from Figures 4.2 and 4.3. For theoretical ray path calculations equations Snell's Law: $sin\theta_2 = \frac{n_2}{n_1} sin\theta_1$, and $\theta_{crit} = arcsin\frac{n_2}{n_1}$ is utilized.

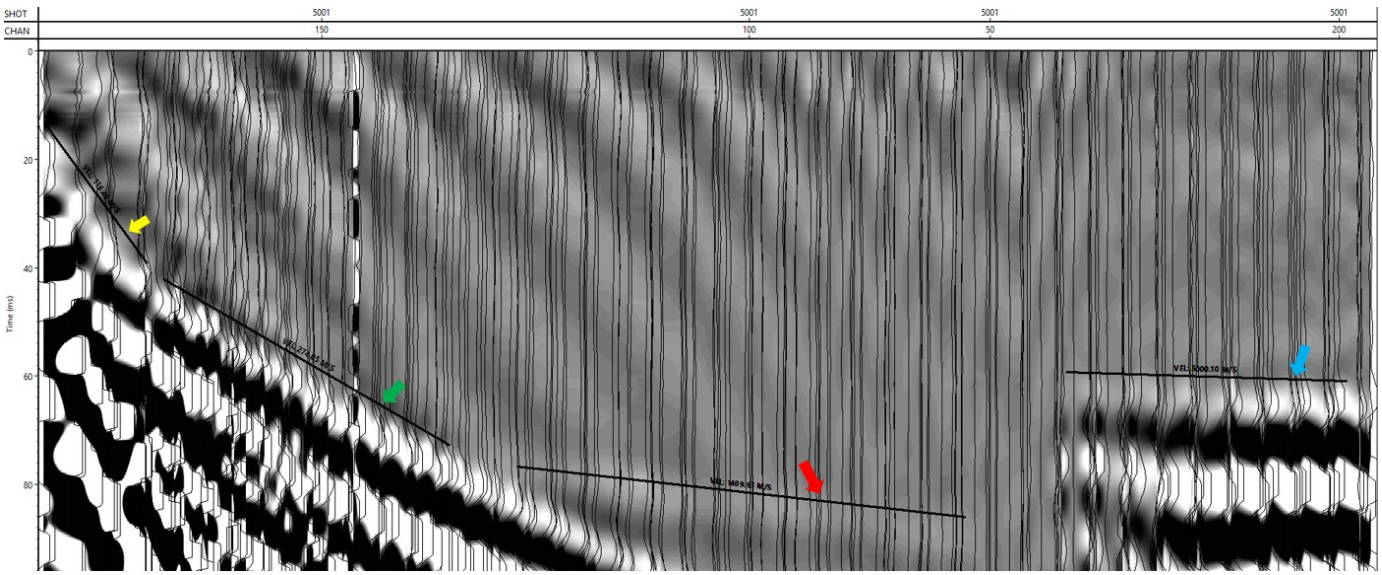

Figure 4.2*: This figure displays the velocities of the subsurface viewed in VISTA© from shot 5001. This is a shot in soft rock, and four different velocities are evident in the DT-1B drill site. The yellow arrow indicates the top weathered soft rock layer that is 116.46 m/s. The green arrow indicates the un-weathered soft rock that is 274.85 m/s. The red arrow indicates a velocity of 1409.93 m/s. The blue arrow indicates the hard rock at 5000.10 m/s.*

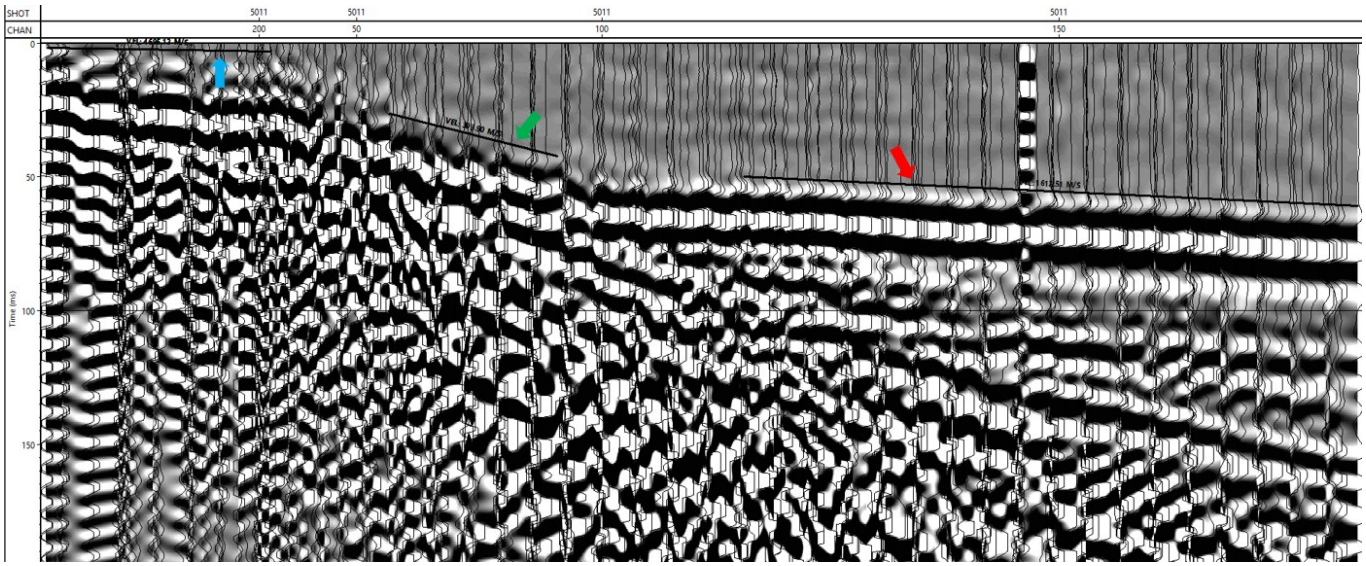

***Figure 4.3**: This figure displays shot 5011, a shot in the hard rock, and three velocities are evident, as the weathered soft rock is not evident in this shot. The blue arrow indicates the hard rock at 5066.28 m/s. The green arrow indicates the un-weathered soft rock at a velocity of 309.39 m/s. The red arrow indicates a velocity of 1623.21 m/s. The weathered soft rock, which is shown with the yellow arrow in 4.2, is not identifiable in the shots activated on the hard rock sections of the survey.*

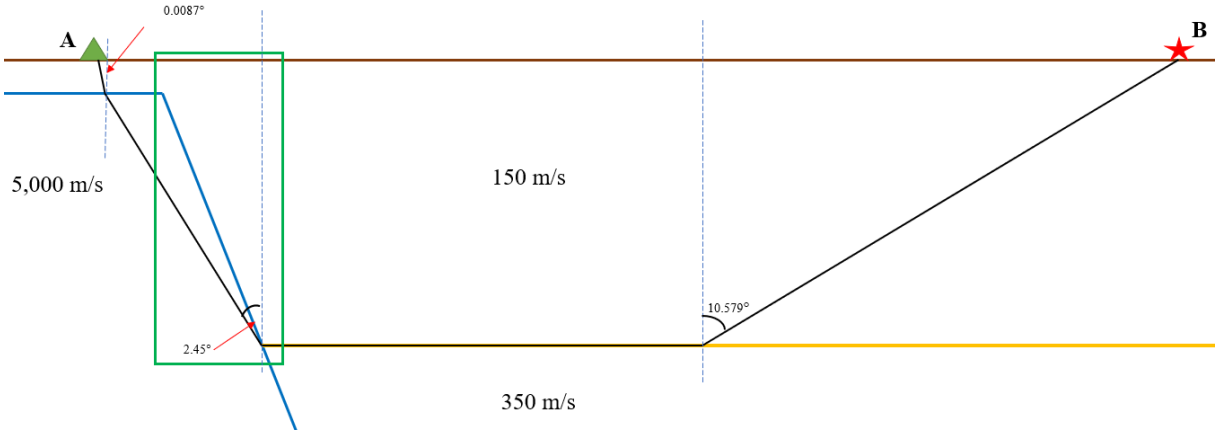

***Figure 4.4**: This image is not to scale and has been horizontally elongated for the express purpose of allowing the calculated critical angles to become visible. This is the theorized subsurface of the survey area. **A** shows the side of the survey that is close to the cliff face to the North-West. **B** represents the side of the survey that is to the South-East and the footpath. The brown line represents the topographical surface. The Blue Lines represent the proposed top and horizontal extensional profiles of the hard rock in the survey. The yellow line at the bottom represents the proposed bottom of the quaternary sedimentary soft rock. The black lines represent the proposed ray paths created by the shots. The green box represents what is designated as the TZ. The green triangle represents the location of the receiver. The red star represents the location of this shot. The dashed blue lines represent a theoretical 90-degree plane to display the calculated angles of the ray paths.*

Prior to the first inversion step and forward modelling using Simulr16, the source and receiver geometry (coordinates) must be defined and the first-arrival travel-times have to be determined. The seismic survey used a 240 channel Summit X One system, with a number of Roll-ons. The channels in this Thesis are Remote Units (RU). The utilized RU convert the

analogue geophone signal to digital, and 7 Summit X One DC Seismographs (SXDC) are used to collect and transmit the digital data to the field laptop. A Roll-on involves removing RUs from activated geophones and pairing them with the soon to be activated geophones. The geophone locations are organised in a rectangular grid that measures 45 by 40 meters previously shown in Figure 4.1. A seismic sweep is the activation of the vibrator, known as the shot. Each shot record is comprised of 238 geophones that were active at one time due to two channels being non-functional. The Trigger Signal (TS) and the Source Sweep Recording Device (SSRD) were also recorded by the SummitX system.

4.2 Survey Set Up

The geophones were placed with a 1-meter separation in 16 Receiver Lines (RL), referred to as In-Lines (IL). Shot locations were at 4-meter separation shot parallel and in-between the receiver lines with a total of 19 Shot Lines (SL). Table 4.1 summarizes the survey parameters and their quantities. Perpendicular to the RL and SL are Cross-Lines (CL), of which there are 40. There are a total of 12 Cross Lines that coincide with the spacing of the shot locations. Figure 4.5 is a schematic of a segment of the SLs, RLs, and CLs. The southeast side of the seismic survey area, near the footpath, is the start of the receiver lines, with the termination of the receiver lines being closest to the cliff face.

Table 4.1*: Survey Parameters*

Survey Parameter	Quantity
Cross-Line Length	45 meters
In-Line Length	40 meters
Distance between Cross-Lines	1 meter
Distance between In-Lines/Receiver Lines	2 meters

Distance between Shot-Lines	2 meters
Distance between Shot Locations	4 meters
Eigen Frequency of Geophones	10Hz
Number of Channels	240
Number of Active Geophones per Sweep	238
Unique Receiver Locations	640
Number of Roll-ons	6
Number of Shot Locations	229
Seismic Sweep	30-120 Hz, 10 second duration, 100 ms taper

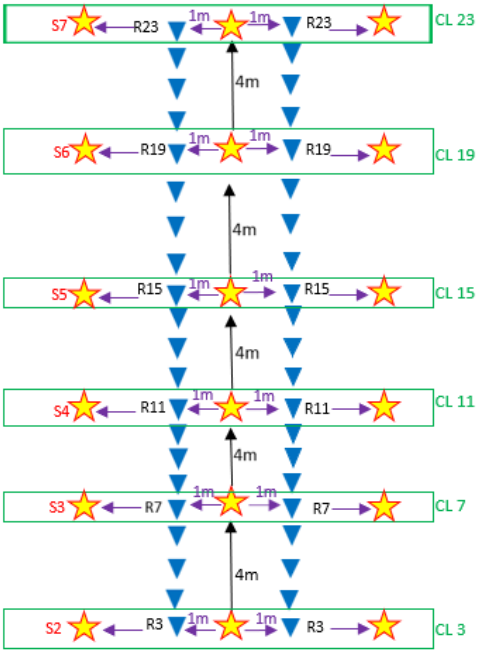

Figure 4.5*: This is a schematic of a SL, RL, and CL. Each red/yellow star is a shot location, with 4-meter separation between each represented by the black arrows. Each blue triangle represents a geophone location with a 1-meter separation between each geophone. The purple arrows represent the 1-meter separation between the SLs and RLs. The green rectangles represent what are designated*

CLs. CL3 includes Receiver 3 and Shot 2, CL7 includes Receiver 7 and Shot 3, and each CL continues thusly.

Each In-Line is comprised of 40 receivers for a total of 40 m offset per In-Line. Every In-Line is separated from the two on either side by a two-meter distance. Each shot sweep had 6 active In-Lines There are a total of 5 subsequent roll-ons to complete the survey. Each roll on is comprised of 6 complete In-Lines including four from the previous roll-on and two new active In-Lines. This process is continued until a total of 16 In-Lines had been swept. The Line Cable is laid out in a snake pattern which is show in Figure 4.6. Between each In-Line a SXDC is placed alternating the on the road side or cliff side of the survey.

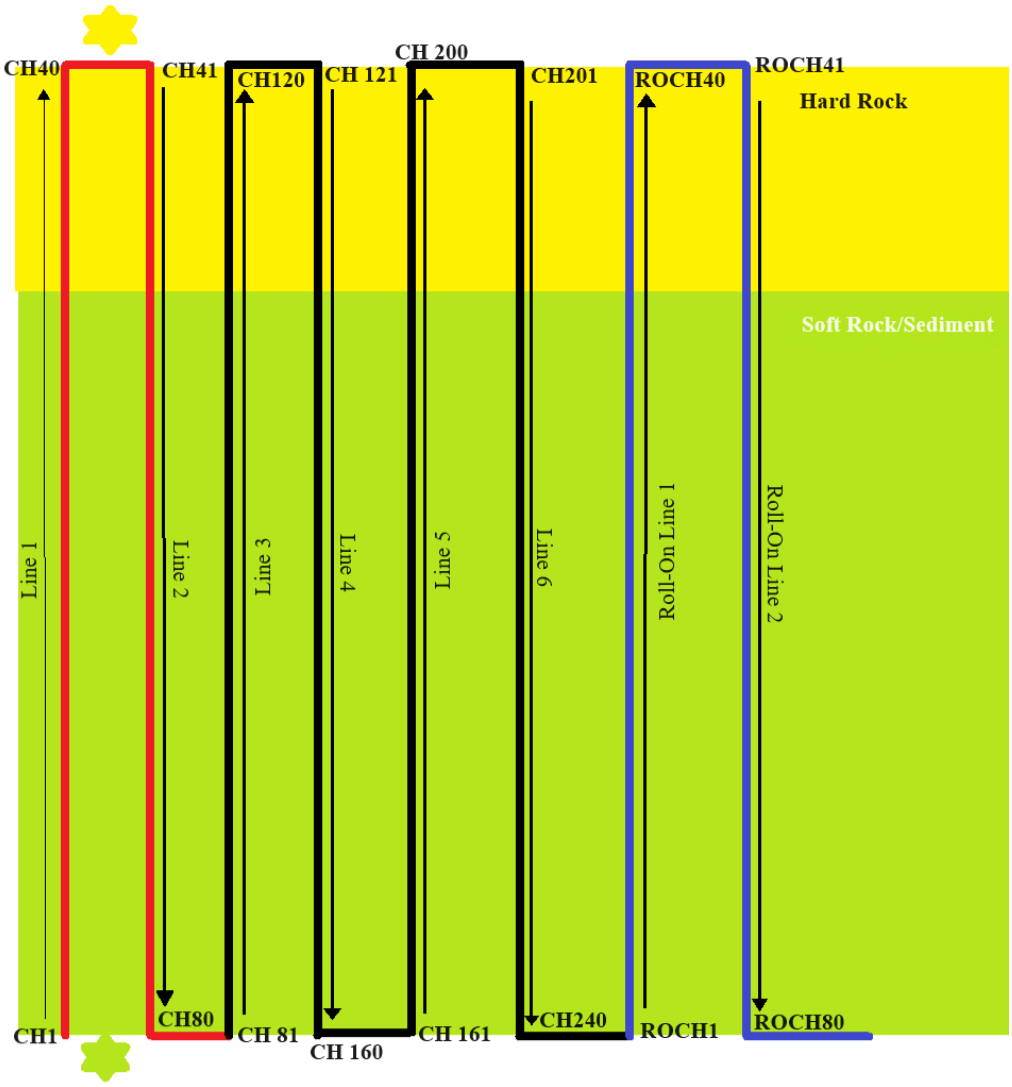

***Figure 4.6**: Schematic illustration of the snake pattern of the survey displaying one full shot sweep, and one subsequent Roll-On. The red lines (titled line 1 and line 2), which start at channel 1 and end*

at channel 80, represent the first two lines of the shot sweep. These lines are those that are removed and then become the Roll-On Lines. The black lines (titled Line 3, 4, 5, and 6) are the remaining lines which form the remainder of the Shot Sweep. These lines include Channel 81 through Channel 240. The Blue lines, titled Roll-On Line 1 (ROL) and ROL 2, are what used to be the red lines that form the entirety of each subsequent roll on. The ROLs restart the channel count at 1 and end at channel 80, both represented by ROCH1 and ROCH80. The parts shaded green represent the southeast sediment dominated side of the survey near the footpath and yellow represents the northwest hard rock dominated side of the survey closer to the base of the hill. The blast markers represent the shot locations on any individual line and are coloured to represent the rock type in which the shots occur. Green in the sediment and yellow in the hard rock. The green shot location is the start of shot line such as 5001 and the yellow shot location is the end of the shot line which would be shot 5012.

The seismic source utilized in the survey is an Electrodynamic-Vibrator-System (ElViS-VII) which is a wheelbarrow style, mobile weighted vibrator. The ElViS's source weight is 32 kgs, but the total hold down weight is 130 kgs. A student's weight is added on top of the ElViS to increase a successful coupling between the vibrator and surface when the sweep is activated. The ElViS-VII system requires preprogramed source sweep chips. The specific sweep is chosen as it had the best interaction, of the available source sweep chips and data gathered from test shots, with the mix of soft sediments and hard rock lithologies that were present in the survey area. The survey sweep is shown in Figure 4.7.

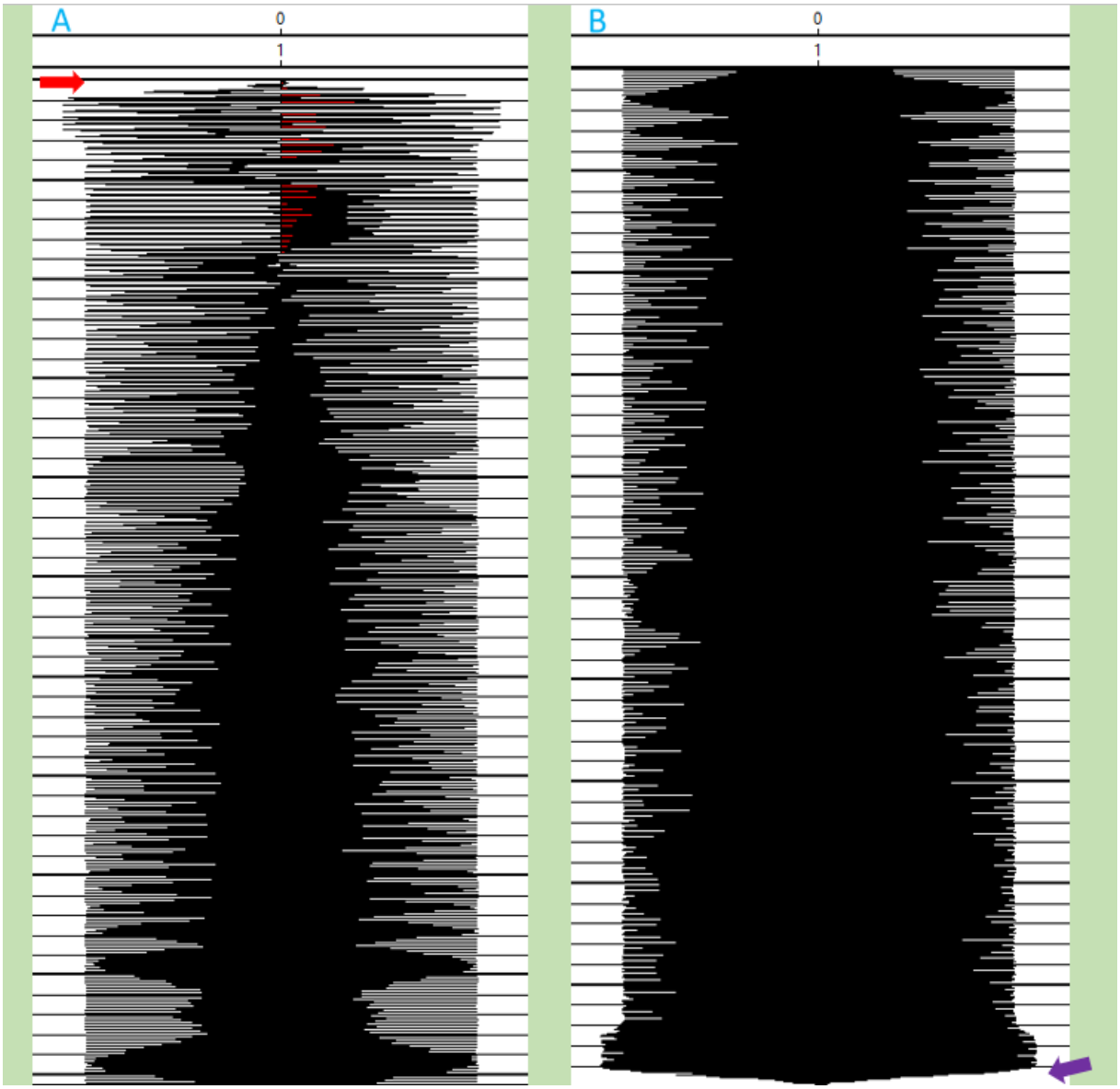

Figure 4.7*: This is an image of the Sweep utilized in the seismic survey as viewed in VISTA©. It lasts 10 seconds. The black and red represents the positive and negative amplitudes of the sweep. A) Displays the first 5000 ms of the sweep. It also includes the lowest frequencies of the sweep starting at 30 Hz. Due to the lower frequency the negative amplitudes are easily detectable. The red arrow indicates the 100 ms long swell as the vibrator starts up. B) Displays the last 5000 ms of the 10 second sweep. The negative amplitudes are no longer visible in B. It includes the highest frequency of the sweep ending at 120 Hz. It also features the 100 ms taper of the sweep, which is indicated by the purple arrow.*

4.3 Survey Geometry

Geophone and shot locations GPS locations were recorded with a Trimble Real-time Kinematic (RTK) system. In the field, distances and angles of both shot and receiver locations were correctly spaced utilizing measuring tapes and an outer square of priorly constructed guidelines to ensure accuracy. However due to field conditions, such as uneven ground

preventing the seismic source from coupling with the ground correctly or a large rock preventing geophone insertion, occasional locations had to be adjusted. The absolute minimum of deviation required from each location is utilized in these instances.

Figures 4.8 and 4.10 display the visual differences between the hard rock and soft rock shots and how they are perceived in the snake pattern of the receivers within the First Break Picks (FBP) window in Vista. This includes active and unactive Automatic Gain Control (AGC) images. Figures 4.9, 4.11, and 4.12 display the average amplitude spectra of Shot 5001 in the soft rock, Shot 5011 in the hard rock, and the entirety of the survey.

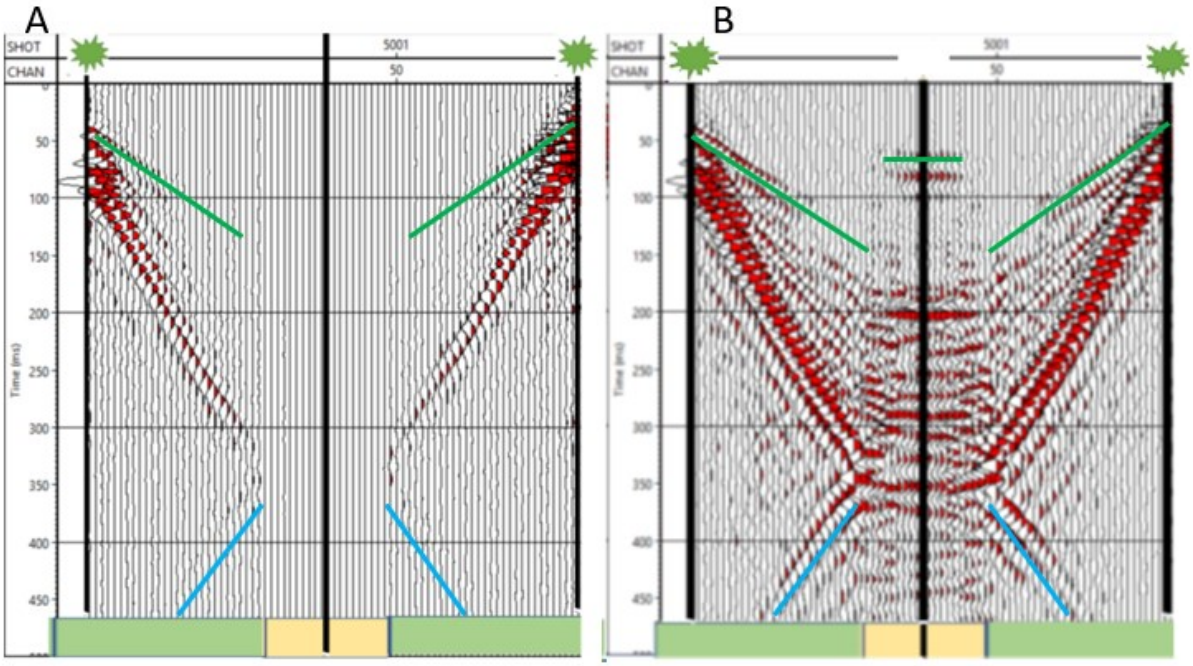

Figure 4.8*: This figure displays the shot location 5001 with consideration to Figure 4.6. The color bars at the bottom and the shot locations at the top, match the colors of Figure 4.6. Green in soft rock, yellow in hard. These shot locations are also located in-between channel 1 and channel 80. This also helps to visualize the snake pattern of the survey. From the black bar on the left to the center black bar is the first IL comprised of channel 1 to channel 40, then the center black bar to the black bar on the right is the second IL comprised of channel 41 to channel 80. The hard rock is located around the central black bar where the yellow color is located at the bottom.* ***A****) Displays that shot 5001, without the AGC correction in Vista, in the soft rock sediment does not display the hard rock reflections. The green lines show the first arrival for the shot. The blue lines at the bottom show a reflected ray from the hard rock back into the soft rock.* ***B****) Displays shot 5001 with the AGC active in Vista with the hard rock part of the survey now visible. The green lines show the first arrival for the shot, unlike in* ***A*** *you*

*can see the hard rock first arrivals. The blue lines at the bottom show display the same reflected rays that were barely visible in **A**.*

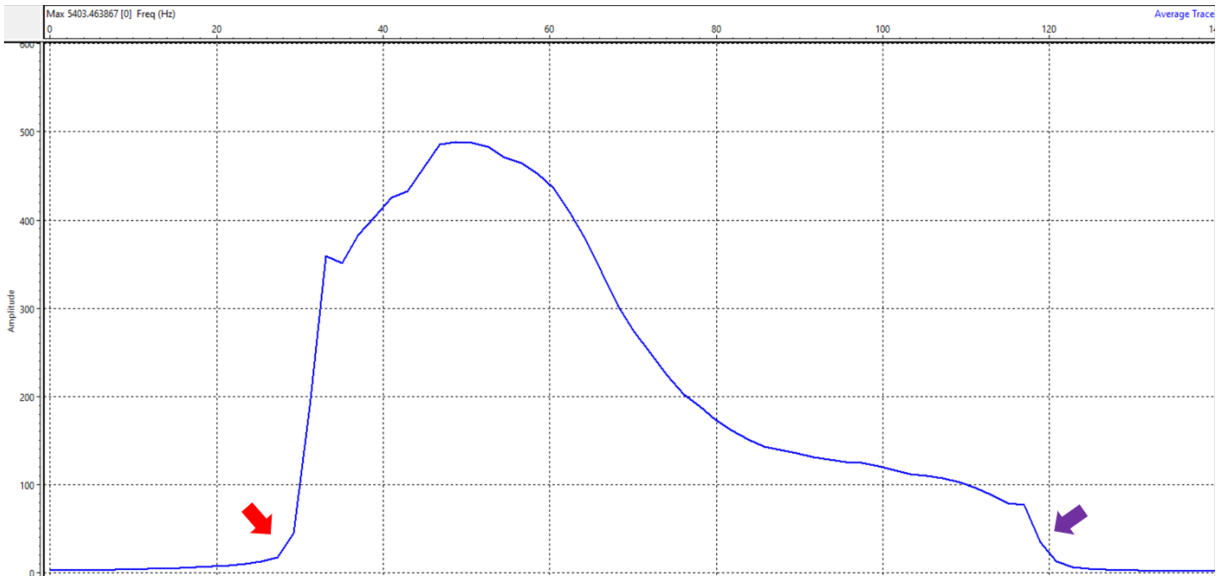

***Figure 4.9**: The amplitude spectra for shot, 5001, as shown in Figure 4.8, which is in the Soft Rock. This utilizes a window in the VISTA© program. The graph lines on the x-axis are 0-140 Hz (Frequency), and 0-600 (Amplitude). The blue line is the average of the traces for shot 5001. Visible on the average of the traces is the 100 ms swell, with its beginning indicated by the red arrow, and taper, indicated by the purple arrow, of the shot. The spectrum does not quite have the boxcar shape that is created for the signal to noise ratio, but it is approximately visible.*

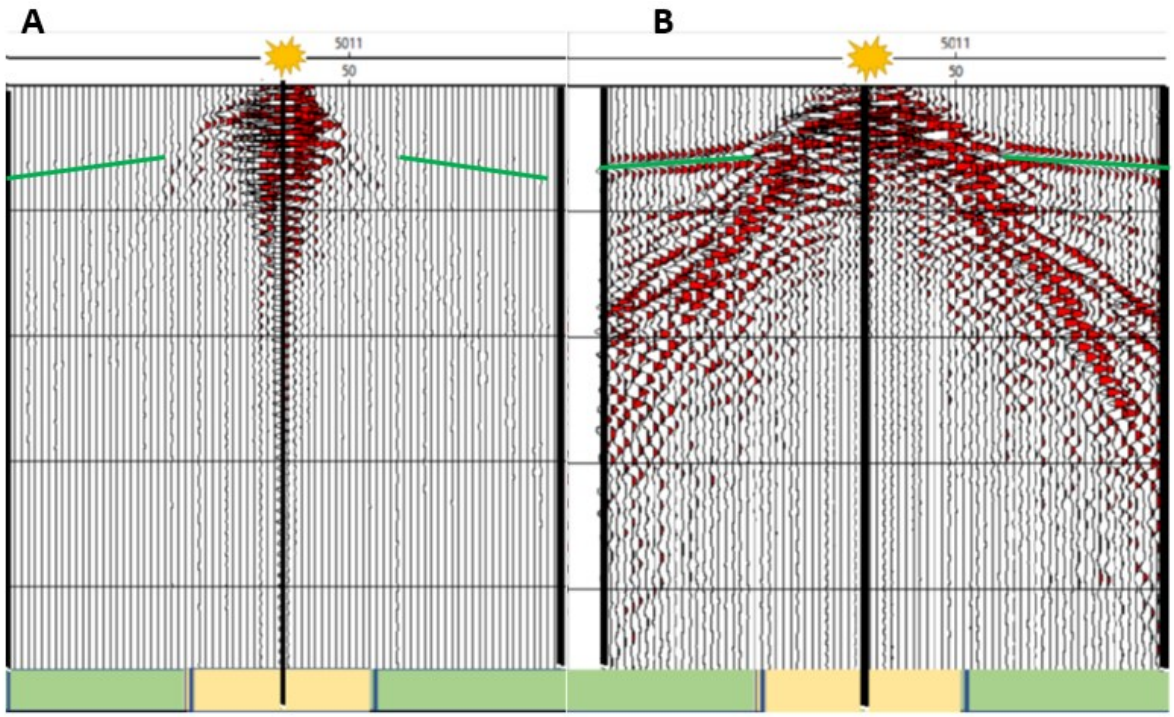

***Figure 4.10**: This figure shows Shot location 5011 with consideration to Figure 4.6, to include the color bars at the bottom of the image and the shot locations at the top. These shot locations are*

different from Figure 4.8 in location and in color to demonstrate where the shot is located on Vista (between channels 40 and 41), and they are yellow to show that they have been initiated on the hard rock of the survey. ***A)*** *Displays shot 5011 without the AGC in Vista. The hard rock segment is completely visible, meanwhile the soft rock part of the survey is hardly visible. However, the First Arrivals are somewhat visible, these are highlighted by the green lines in the top third of the image.* ***B)*** *Displays shot 5011 in Vista with the AGC active. This makes the soft rock portion of the survey visible, and allows the FBPs to be picked more accurately. The barely visible first arrivals in* ***A*** *are much more visible with the AGC active and are also highlighted by the green lines at the top third of the image.*

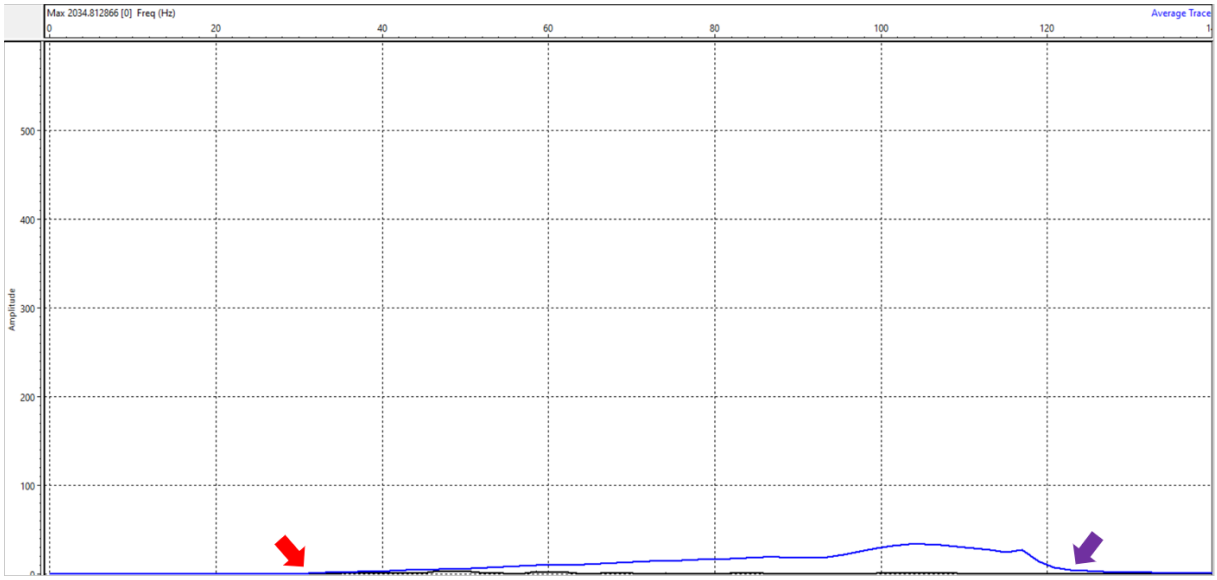

Figure 4.11*: This Figure displays the amplitude spectra for the entirety of the same shot, 5011, as shown in Figure 4.10, located in the Hard Rock. This utilizes a window in the VISTA© program. The graph lines on the x-axis are 0-140 Hz (Frequency), and 0-600 (Amplitude). The blue line is the average of the traces for shot 5011. The 100 ms swell is indicated by the red arrow. The 100 ms taper is indicated by the purple arrow. The spectrum is drastically different from Figure 4.9 lacking anything close to the boxcar shape.*

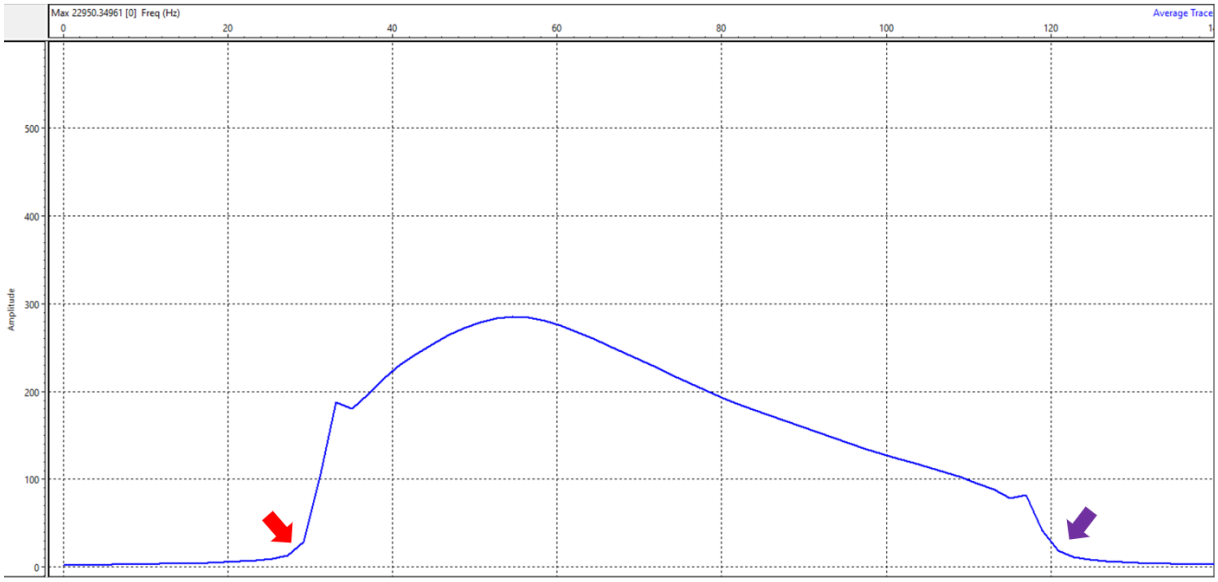

***Figure 4.12**: This figure displays the average amplitude spectra for the entire survey all 54502 traces. The graph lines on the x-axis are 0-140 Hz (Frequency), and 0-600 (Amplitude). This utilizes a window in the VISTA© program. The blue line is the average of the traces. The 100 ms swell is indicated by the red arrow. The 100 ms taper is indicated by the purple arrow. The average's more rounded shape, compared to Figure 4.9, displays how the differences between the hard rocks and soft rocks interact with the sweep's frequencies. However, the spectra are still much more amplified than the pure hard rock of Figure 4.11.*

Each of the 19 shot lines is comprised of between 11 and 13 shots. Shot Lines 1 and 2 were the only SLs that were comprised of 11 shots in total. SLs 3 through 16 entail the shot lines that are 12 shots in length. SL 17 through 19 all have 13 shots. This variation is caused by the encroachment of bushes and overgrowth at the base of the cliff into the survey area, to the Northwest of the survey site.

Each shot location had two activations of the source. The second sweep is instituted for redundancy and had the added benefit of ensuring a better coupling between the ElViS-VII system and the ground to ensure a higher signal to noise ratio. The two shot activations at the same locations were stacked prior to any processing. However, the final three shot lines do not have two activations per site. As these three shot lines were added onto the initial survey for extra data and greater depth acquisition, and due to time limitation, each of these lines had only one activation of the source on each shot location.

5: Data Quality Assurance and Quality Control

5.1 Introduction

The integrity, data analysis, and results of this Thesis all rely upon ensuring that every part of the process has undergone QA and QC. QA establishes and maintains requirements for data. QC is the process through which a researcher ensures that data quality requirements are maintained. Multiple methods of both QA and QC were utilized in this Thesis including Initial FBP Repicks, Offset vs. FBPs Graph, Root Mean Square Error (RMSE) Calculations, and 2D vs. 2.5D Simulr16 inversion processing options. This chapter goes into the procedure, location in the workflow of the Thesis, and displays examples, of each individual QA/QC method utilized.

5.2 FBP QA/QC Methods

5.2.1 Vista FBP QA/QC Window

All FBP were visually handpicked in VISTA©. The original FBP selection underwent several complete repicks to identify hidden layers that were not considered during the first picking process. After calculating RMS errors and running the first couple of trial inversion steps in Simulr16, subsequent iterations of picking were performed and the hidden layer is identified. Bad picks and outlying traces were also identified during this second picking process by utilizing a horizon flattening function in VISTA©. Figure 5.1 displays one flattened shot record in Vista that includes several missing picks. The same window is shown again after corrections in Figure 5.2.

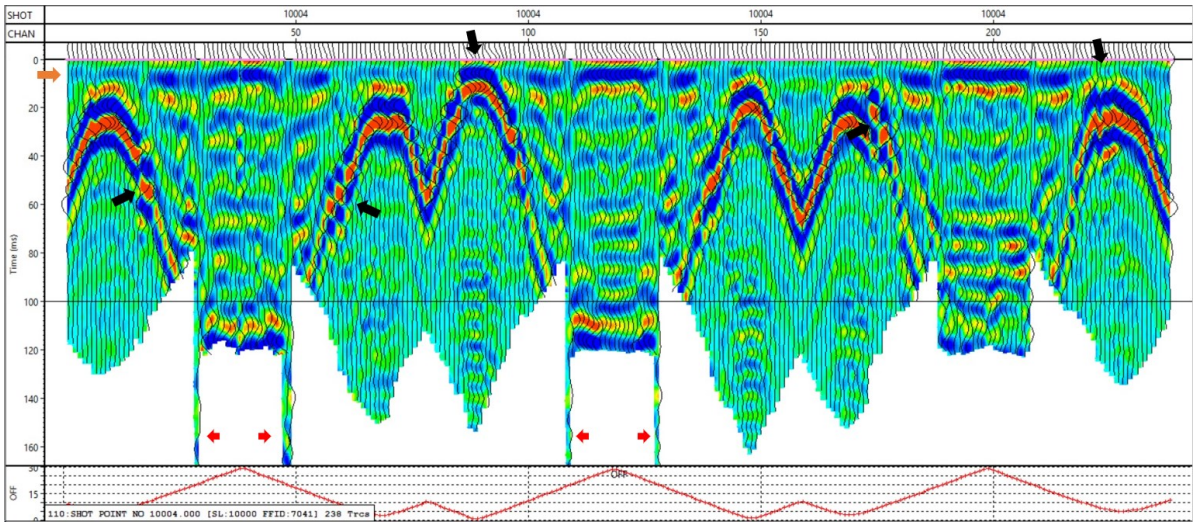

Figure 5.1*: Displays the entirety of Shot 10004 in a functional window in VISTA©. In this window the shot flattens the top of the data recording on the selected FBP this is visible by a thin pink line at the top of the blue, green, red, and yellow seismic image. This increasing and decreasing trend follows logically the snake pattern layout of the survey itself. The orange arrow in the top left of the image indicates the flat straight blue (or negative) layer generated by the seismic source. This helps to displays the effectiveness of the chosen FBPs. The black arrows placed throughout the image show questionable and noisy traces that have possibly been erroneously picked, and thus need to be fixed in the QA/QC process. The red arrows at the bottom of the image display places where there are traces that have been missed in the original picking process. The red line at the bottom of the image that is separated from the rest of the image displays the distance offset of the individual traces from the shot location.*

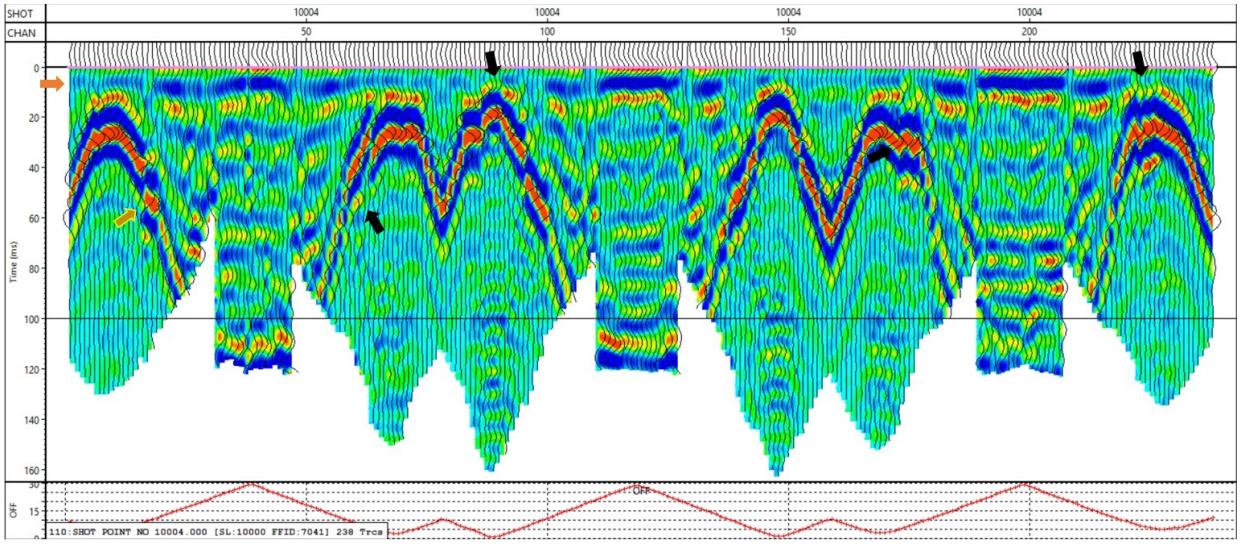

Figure 5.2*: This image shows the corrected view of Shot 10004 in Vista. This image is the exact same image as Figure 5.1 post corrections. The orange arrow at the top left once again indicates the negative layer that exists below the FBP displaying a nearly continuous layer. The unpicked traces from Figure 5.1 have been corrected and picked. The black arrows throughout indicate the previous possibly noisy traces that were deemed to be needed corrected. The questionable area from Figure 5.1 displayed by the brownish yellow arrow in the center left of the figure is the one erroneous region that is deemed to have been correctly picked.*

5.2.2 Matlab Travel Time QA/QC

The second method of FBP QA/QC utilized a Matlab code that graphs the FBP values versus the travel-path between the receiver and source locations. This generates a "V" image that displays the change in velocities of the subsurface within the survey area. It is possible to identify on the graph any outlying or erroneous picks. Figure 5.3 displays the travel time plot of In-Line 7 pre-correction. This is the IL profile that underwent the 2D inversion process. Figure 5.3 shows this QA/QC process also identified an error in acquisition, whereby the first 4 ms of the data had been excluded from the beginning of the data recording. All FBPs times were subsequently corrected by 4 ms, and the post QA/QC correction process image is displayed in Figure 5.4. After the corrections were applied to IL 7 the "V"s are much more evident, excepting the very points which are above the 4 ms line that deliminates the unrecorded segment.

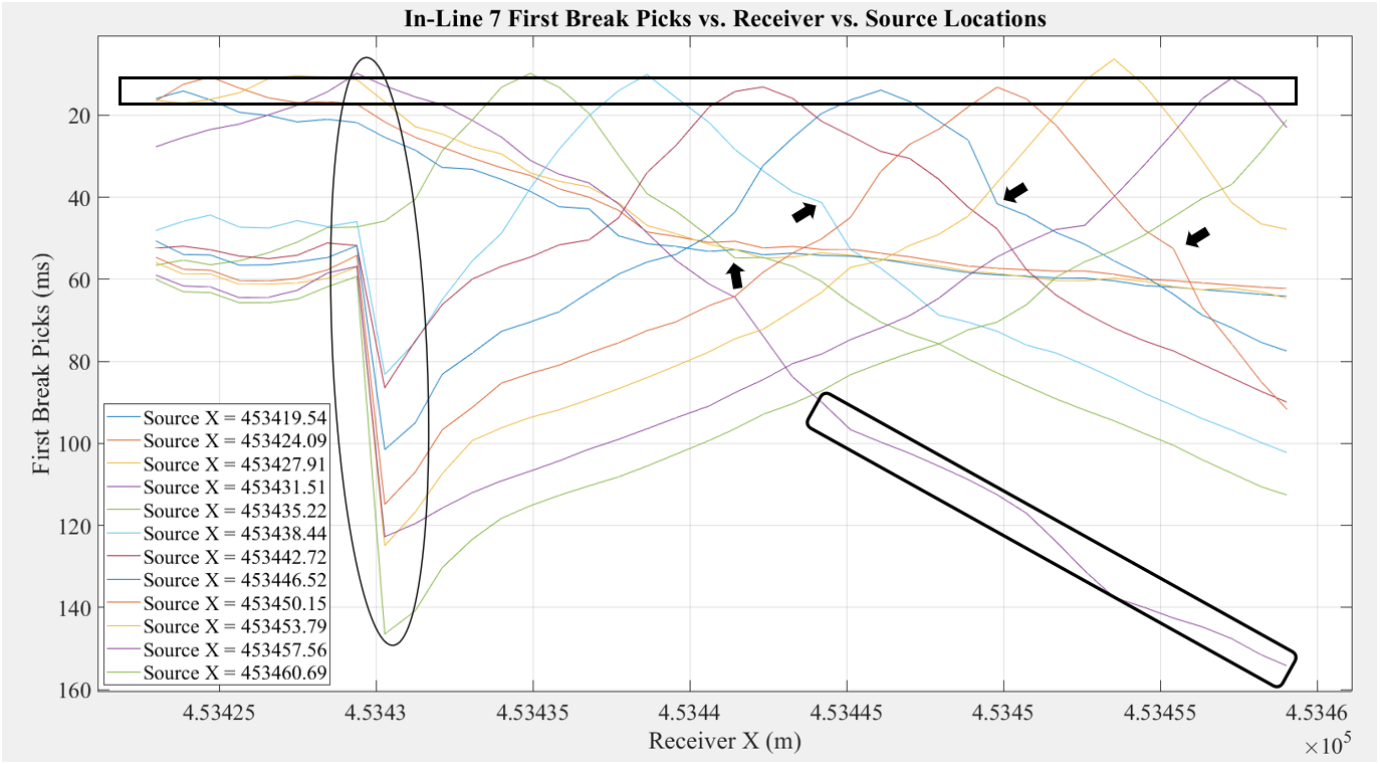

***Figure 5.3**: This image displays the In-Line 7 Travel Time QA/QC for FBPs. Each individual-colored line represents all of the receivers along the line for a single shot. The points at the top of the graph for each of these lines are the shot locations, and the displacement from those points on the graph equate to the distance from the shot point on the IL. The black square at the top of the figure displays the perceived problem of the unrecorded 4 ms, and the effect this has on the "V"s that are generated by the velocity offset code. The black oval surrounds what has been termed the TZ, which is where the*

FBPs are not able to be validly picked. The black arrows indicate traces with high likelihood of being erroneously picked. The black square in the bottom right of the figure indicates an entire third of a line that is possibly incorrectly picked, as it drastically diverges from the other lines.

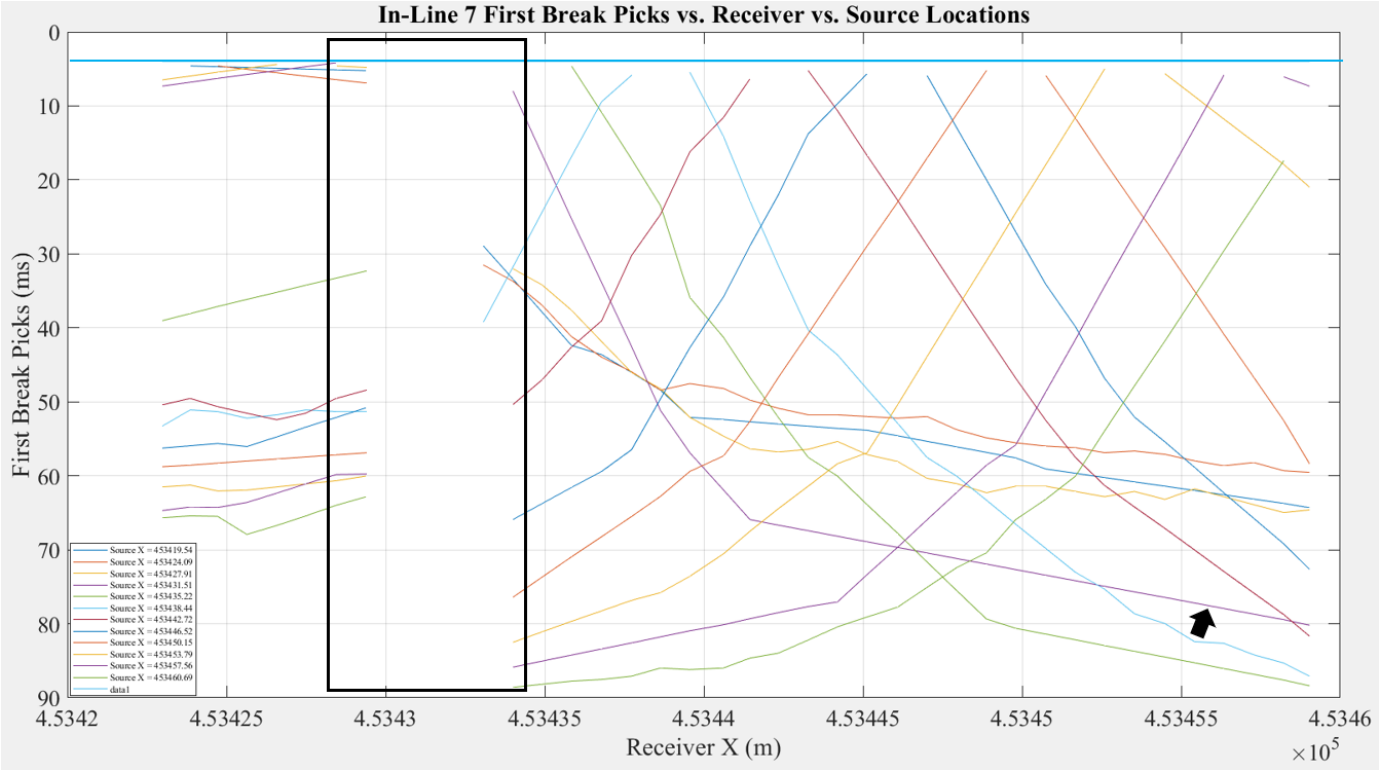

***Figure 5.4**: This figure displays the results of the post QA/QC correction of In-Line 7. The blue line at the top is exactly at 4 ms below and denotes the probable missing data. The traces that are right near the shots are all above this line and thus have not been picked. That is why the colored lines are not connected. The large black square denotes the location of the TZ, and the traces cannot be validly picked, thus they are missing and the lines do not connect. The line indicated by the black arrow is the line from the bottom right part of Figure 5.3 that diverged from the other lines. It is identified as being incorrectly chosen, corrected, and now follows the trends of the other shots. All the possible erroneous picks indicated by black arrows in 5.3 were incorrectly picked and have been corrected.*

5.3 Offset vs. First Break Picks

In this method of QA/QC the offset and FBP data is taken from Vista and a utilized in a Matlab code to display potentially erroneously chosen FBPs. The erroneous traces are identified, their Offset and FBP time are recorded, and then those traces were re-inspected, and re-picked. Most of these erroneous picks were human error however a couple were identified as being on traces with heavy noise contamination. This method of QA/QC is

performed on the Hard Rock Crossline, the Soft Rock Crossline, the Inline 7, and the entire survey. These are displayed on Figures 5.5 through 5.11.

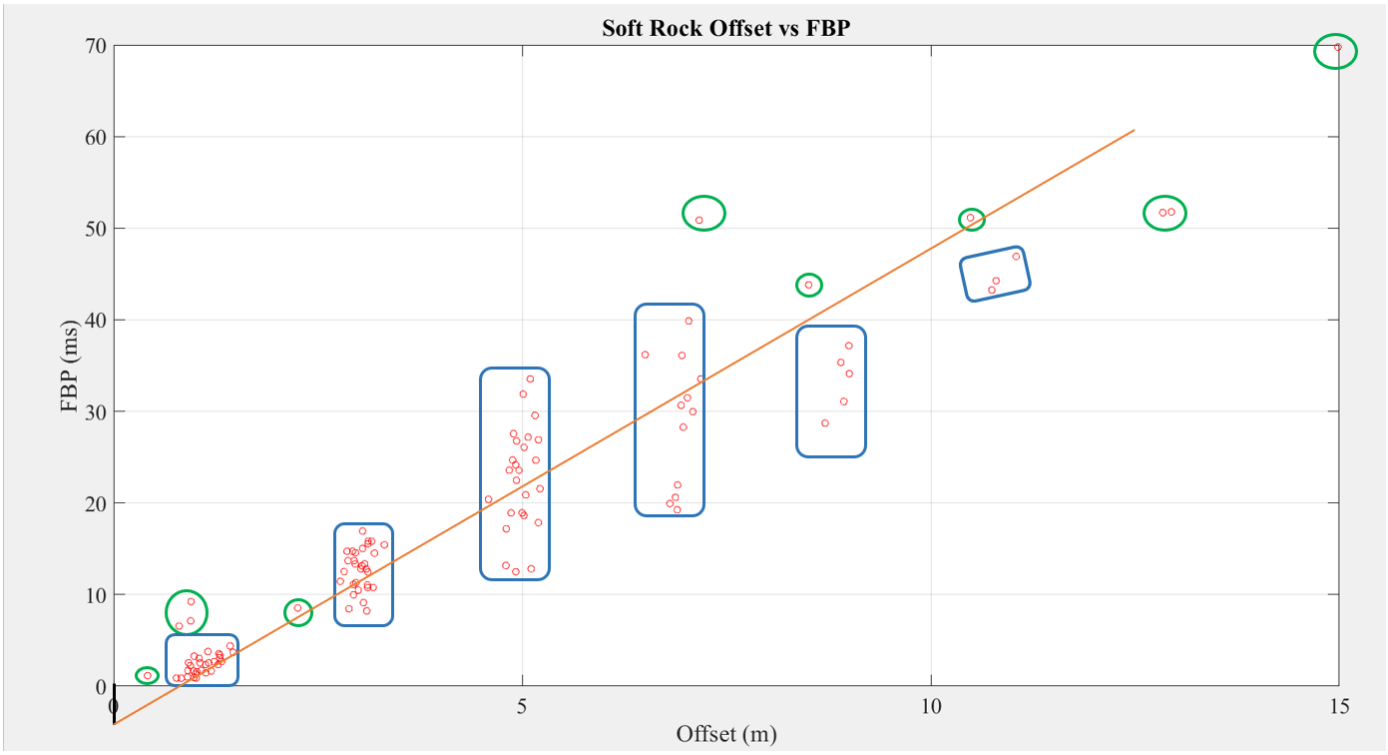

***Figure 5.5**: Soft Rock Cross-Line 4's traces Offset vs. FBP pre-correction plotted in Matlab. Each Individual red circle represents the exact cartesian coordinate of every trace in the Soft Rock Cross Line 4. The black line shows the time correction of the proposed un-recorded 4 ms. The orange line represents the proposed Best Fit Line (BFL) for the Offset vs. FBP this is calculated approximately as* $\frac{10m}{.051s}$ *to 197 m/s. The green circles represent erroneously chosen FBP of traces which are then subsequently noted down for a re-investigation of the picking process. The blue rectangles represent the clustering of the 6 active In-Lines that are active on each shot sweep. These 6 In-Lines as previously stated have approximately 2 meter separation from one another and this is represented in this figure.*

***Figure 5.6**: Hard Rock Cross-Line 10's traces Offset vs. FBP pre correction plotted in Matlab. This image has the same layout and parameters as Figure 5.5, however the proposed un-recorded 4 ms has already been added. The orange line represents the proposed BFL for the Offset vs. FBP this is calculated approximately as $\frac{10m}{.011s}$ to 909 m/s.*

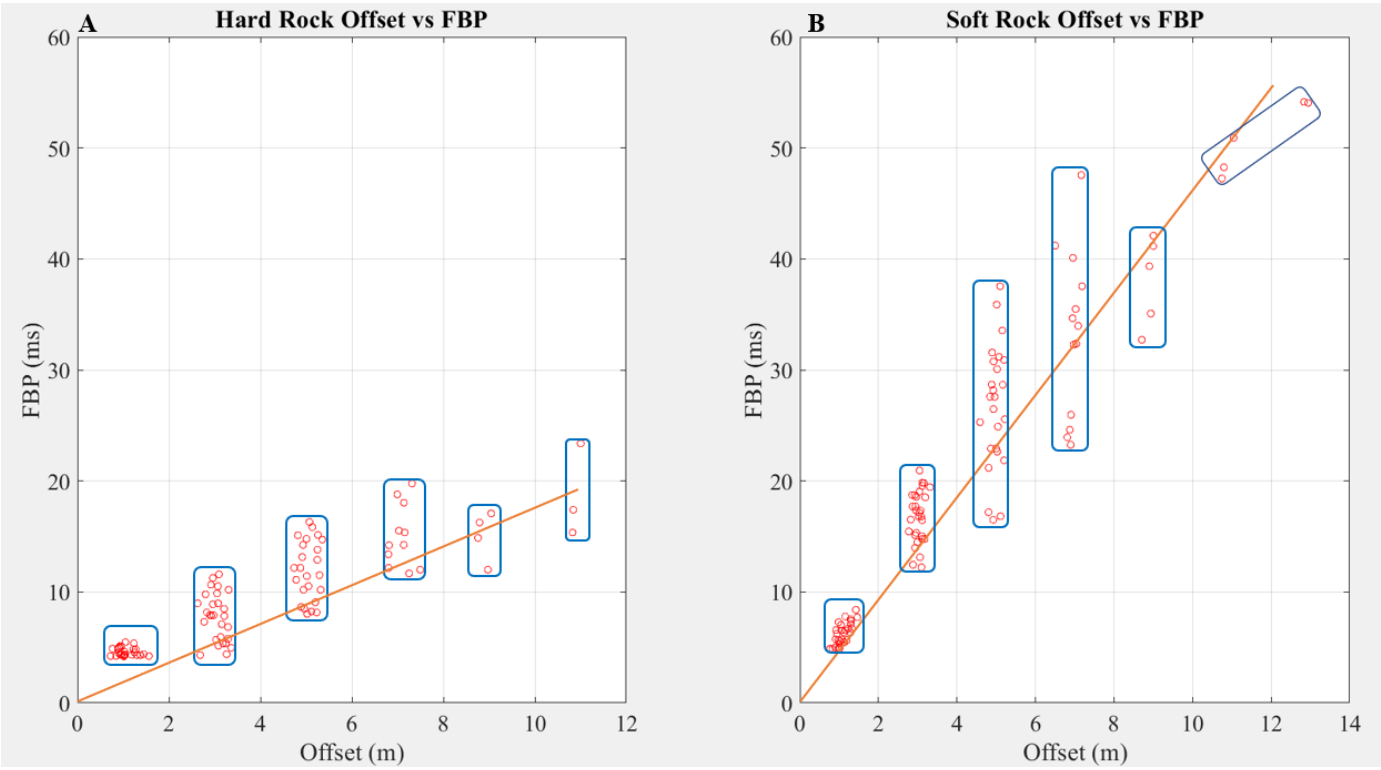

***Figure 5.7**: A is the corrected version of the Hard Rock Cross-Line 10's traces FBP vs. Offset post correction. B is the Figure of the Soft Rock Cross-Line 4's FBP vs. Offset post correction. In both sub images the blue rectangles represent the 6 clusters for the active line per shot sweep. The orange line*

*represents the proposed BFL on both **A** and **B** for the Offset vs. FBP. These are calculated approximately: **A)** $\frac{10m}{.017s}$ for 589 m/s and **B)** $\frac{10m}{.047s}$ to 213 m/s.*

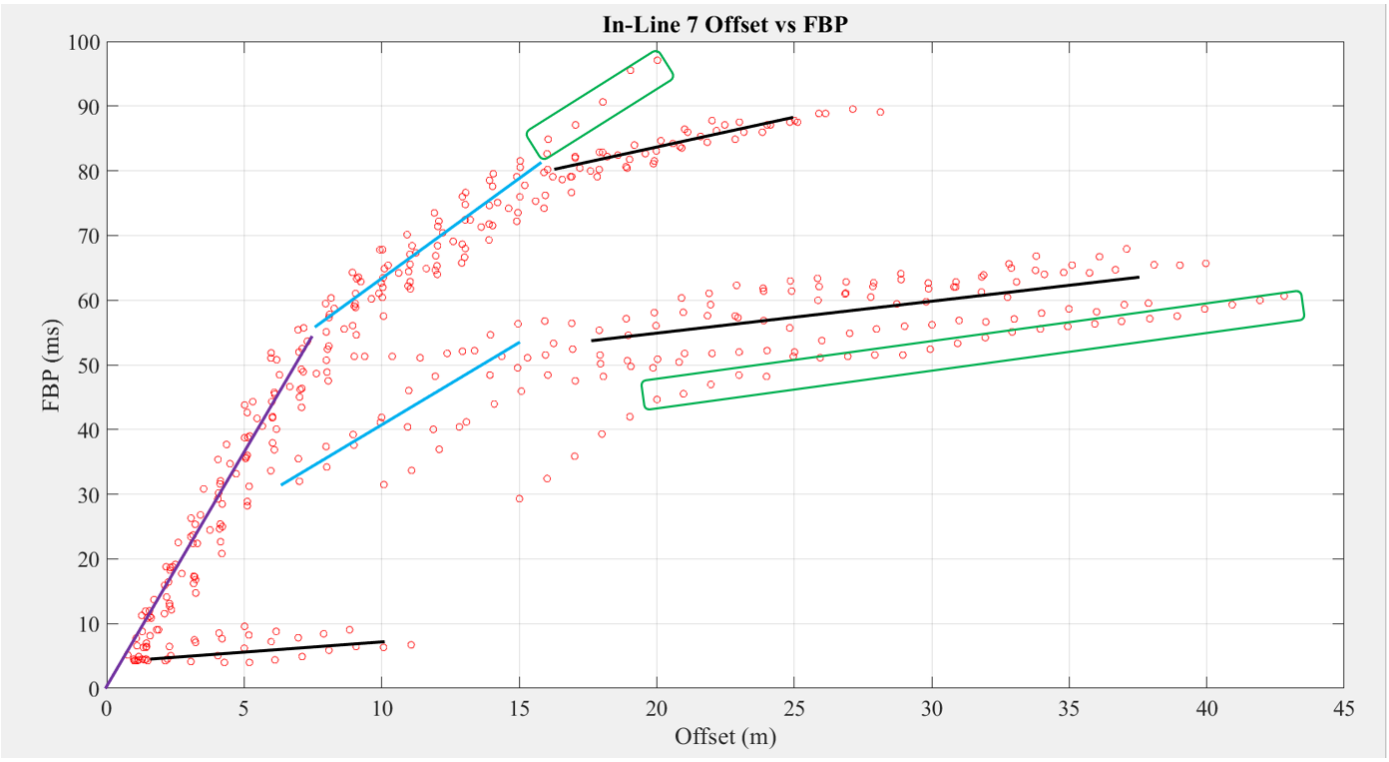

***Figure 5.8**: In-Line 7's traces Offset vs FBP pre-correction plotted in Matlab. Each individual red circle represents the exact cartesian coordinate of every trace of the In-Line profile. The green rectangles indicate erroneously picked traces which are then subsequently noted down for a re-investigation of the picking process. The straight lines represent the three lithological velocity trends represented in the survey area. These are color coded so that: the purple line represents the most shallow lithology that is approximately $\frac{7.5m}{0.055s}$ 137 m/s, the two blue lines represent the deeper soft rock that is approximately $\frac{8.5m}{0.025s}$ 340 m/s, and the black lines represent the hard rock lithology which is approximately $\frac{15m}{0.009s}$ 1,667 m/s.*

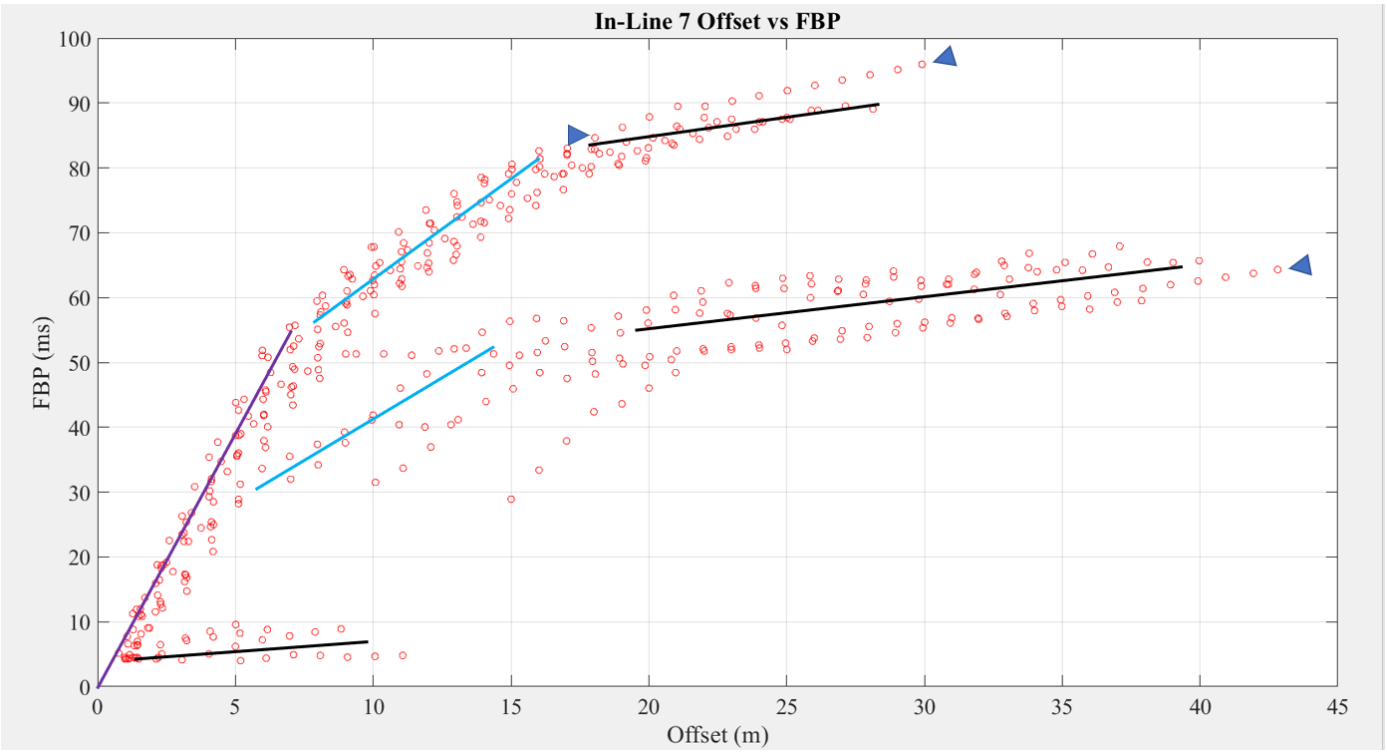

***Figure 5.9**: In-Line 7's traces Offset vs. FBP post correction plotted in Matlab. This image displays the corrected version of Figure 4.8. The corrected traces are indicated by the blue triangles which replace the green rectangles in Figure 5.8. These corrected traces now follow the trend of the Offset vs. FBP of the rest of In-Line 7. The straight lines represent the three lithological velocity trends represented in the survey area. These are color coded so that: the purple line represents the most shallow lithology that is calculated as: $\frac{8m}{0.055s}$ for 145 m/s, the two blue lines represent the deeper soft rock that is calculated as: $\frac{8m}{0.025s}$ for 320 m/s, and the black lines represent the hard rock lithology which is calculated as: $\frac{10m}{0.006s}$ for 1667 m/s.*

***Figure 5.10**: 3D Survey's traces plotted as First Break Picks vs. Offset plotted in Matlab. Each individual red circle represents the exact coordinate of every one of the 54k traces in the survey. The blue triangles at the bottom indicate the non-picks of the FBP due to noise, corruption, or inability to pick. In the data these are represented as a -1 for FBP thus they are located below y=0. The green rectangles indicate erroneously picked traces are noted, and then are either repicked to fit the survey, or changed into a -1.*

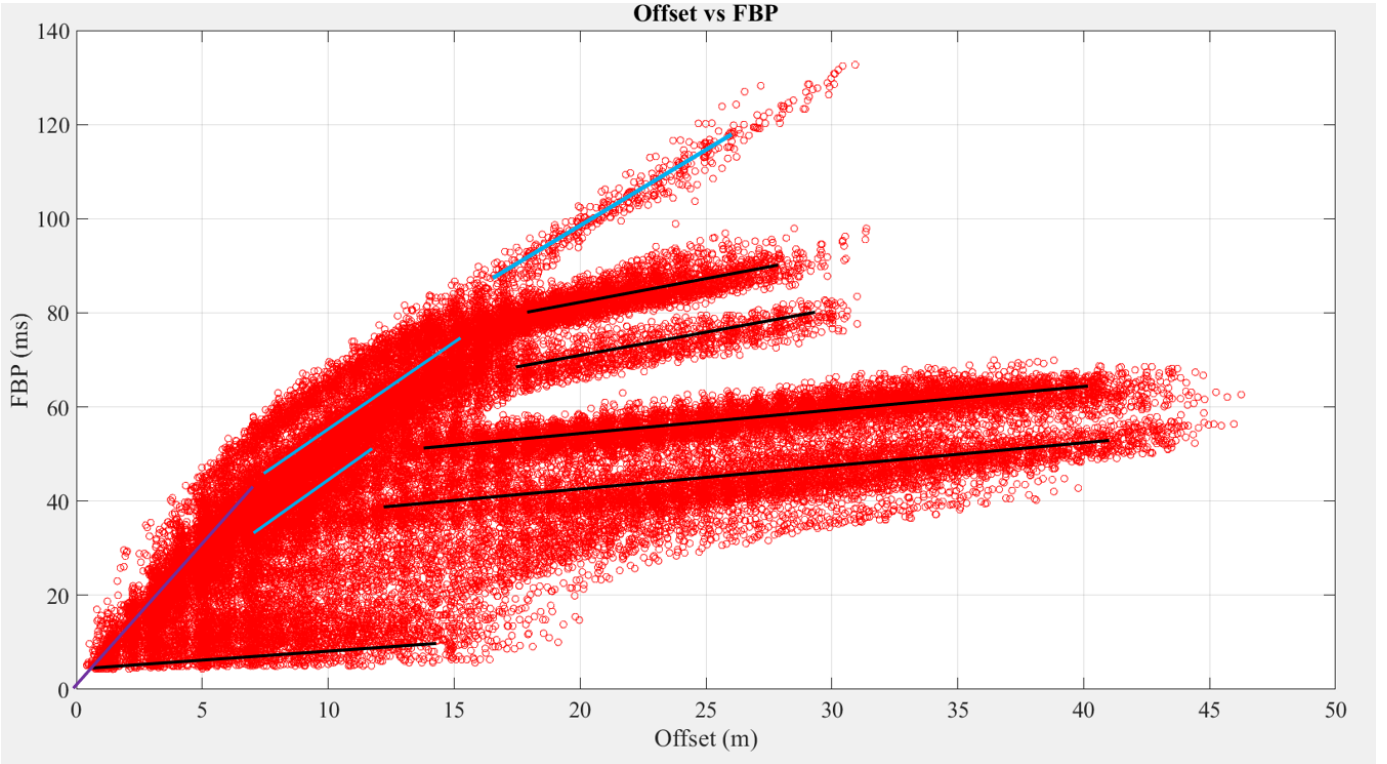

***Figure 5.11**: 3D Survey's traces plotted as FBP vs. Offset post correction plotted in Matlab. This*

image has the same layout and parameters as Figure 5.10. The corrections have been applied including the 4 ms added. The straight lines represent the three lithological velocity trends represented in the survey area. These are color coded so that: the purple line represents the most shallow lithology that is calculated as: $\frac{7m}{.044s}$ *for 159 m/s, the two blue lines represent the deeper soft rock that is calculated as:* $\frac{6m}{.015s}$ *for 400 m/s, and the black lines represent the hard rock lithology which is calculated as:* $\frac{20m}{.0.010s}$ *for 2,000 m/s.*

5.4 Root Mean Square Error Calculations

Root Mean Square Error is the standard deviation of the prediction errors. These prediction errors are a measure of how far from the regression line, or Best Fit Line (BFL), each individual data point is located. This gives the information of how concentrated the data is around the BFL. In the Thesis it is the difference between the observed FBP time versus the predicted FBP time. Two methods of the RMSE were utilized to ascertain the level of noise and accuracy of the FBPs (the observed data), as well as the goodness of fit between the observed and theoretical data, these were manual and Simulr16 calculated, respectively.

5.4.1 RMS Error Manual Calculation

The formula for the RMSE utilized in this method of the Thesis is:

$$RMSE = \left[\sum_{i=1}^{N} \frac{(z_p - z_o)^2}{N}\right]^{1/2}$$

Where ***p*** equals the predicted FBP value, and ***o*** is the observed FBP value. This method is only applicable to calculate the RMS of the In-line profile and the full 3D survey, due to the manner in which it is designed. In this method a Shot/Receiver Couple (SRC) with its corresponding FBP value is set as the predicted variable and then its exact inverse SRC FBP value is set as the observed variable. Figure 5.12 gives a display of how this method is designed and is calculated. It is a simplified diagram of a complete line of the RMSE

calculations as a full line has 11 SRCs. Each of those 11 SRCs is calculated against every other SRC in the line.

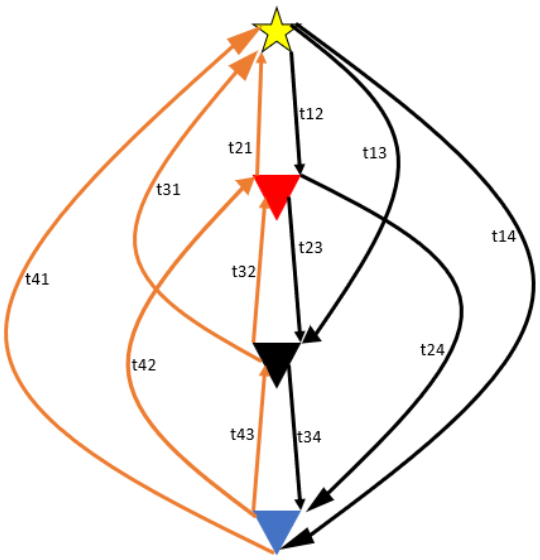

***Figure 5.12**: A simplified diagram of the RMSE Shot/Receiver Couple calculation method. In this diagram each triangle represents an SRC. The star represents an SRC where the vibrator is currently active, which is also SRC number 1. The red triangle is SRC number 2, the black triangle is SRC number 3, and the blue triangle is SRC number 4. Every black line arrow represents the Predicted FBP time between the two SRC, and every orange line arrow represents the Observed FBP between the two SRC. The lines are labelled for easy display of the function of the RMSE calculation. The line labelled t14 is the Predicted FBP from SRC number 1 going to SRC number 4, and its inverse, t41, is the Observed FBP from SRC number 4 going to SRC number 1.*

Due to the 3D survey design, all the co-located Shot/Receiver Couples have an approximate 1-meter offset between the shot and receiver. It is necessary in this calculation that this 1-meter offset is considered as being negligible. This is due to the lack of co-location and the small size of the survey as any non-negligible RMSE calculation cannot be, independently of Simulr16, validated.

Table 5.1 shows the RMSE calculation for all SRC within the IL7SL8 inversion profile. The total sum of the SRC RMSEs is then averaged and gives the result for the In-Line Profile and 3D profile. The calculated RMS average for IL7SL8 is 3.54. The 1st SRC's FBPs populates the Forecast column, the inverse of that FBP populates the Observed column, the third

column is the Difference between the two, and the final column displays the Squared Value of the calculated difference. The exact same method is applied to the complete fourth Roll-on (RLs 7 through 12) for an RMSE average of 6.06. Its larger error is attributed due to introducing a 3rd dimension into the calculation, instead of just a linear approximation.

***Table 5.1**: In-Line 7 RMSE utilizing the Shot Receiver Couples Calculation.*

Forecast	Observed	Difference	Squared
65.653	61.747	-3.906	15.2568
74.495	71.845	-2.65	7.0225
77.771	80.169	2.398	5.7504
81.047	82.832	1.785	5.7504
57.085	59.897	2.812	3.18622
60.215	54.201	-6.014	7.90734
46.401	48.055	1.654	36.1682
60.445	60.205	-0.24	2.73572
71.785	74.641	2.856	0.0576
77.088	79.724	2.636	8.15674
57.085	58.117	1.032	6.9485
57.254	52.646	-4.608	1.06502
19.004	23.022	4.018	21.2337
42.711	42.802	0.093	16.1443
58.765	62.545	3.78	0.00865
69.685	76.616	6.931	48.0388
53.445	57.405	3.96	15.6816

54.565	51.353	-3.03	9.1809
18.024	18.759	0.735	0.54022
45.577	48.895	3.318	11.0091
59.745	63.763	4.018	16.1443
49.42	54.067	4.647	21.5946
51.94	48.202	-3.738	13.9726
20.652	27.579	6.927	47.9833
43.014	48.107	5.093	25.9386
47.536	52.775	5.239	27.4471
45.536	46.869	1.333	1.77689
20.334	19.494	-0.84	0.7056
47.091	44.229	-2.862	8.19104
47.091	44.425	-2.666	7.10756
30.234	30.198	-0.036	0.0013
1.958	1.979	0.021	0.00044
		Sum =	402.5076
		Average =	12.5783
		Calculated RMSE =	3.5465

5.4.2 Simulr16 RMS L-Curve Test

The Simulr16 program calculates an RMS error value for each iterative inversion step. However, it is necessary to have first run a damping test for each model. This process is discussed as the L-Curve Test in section **3.2**. Figure 5.13 is the L-Curve Test for the ILSL8

inversion model, and this provides the damping value to use for the subsequent inversion process.

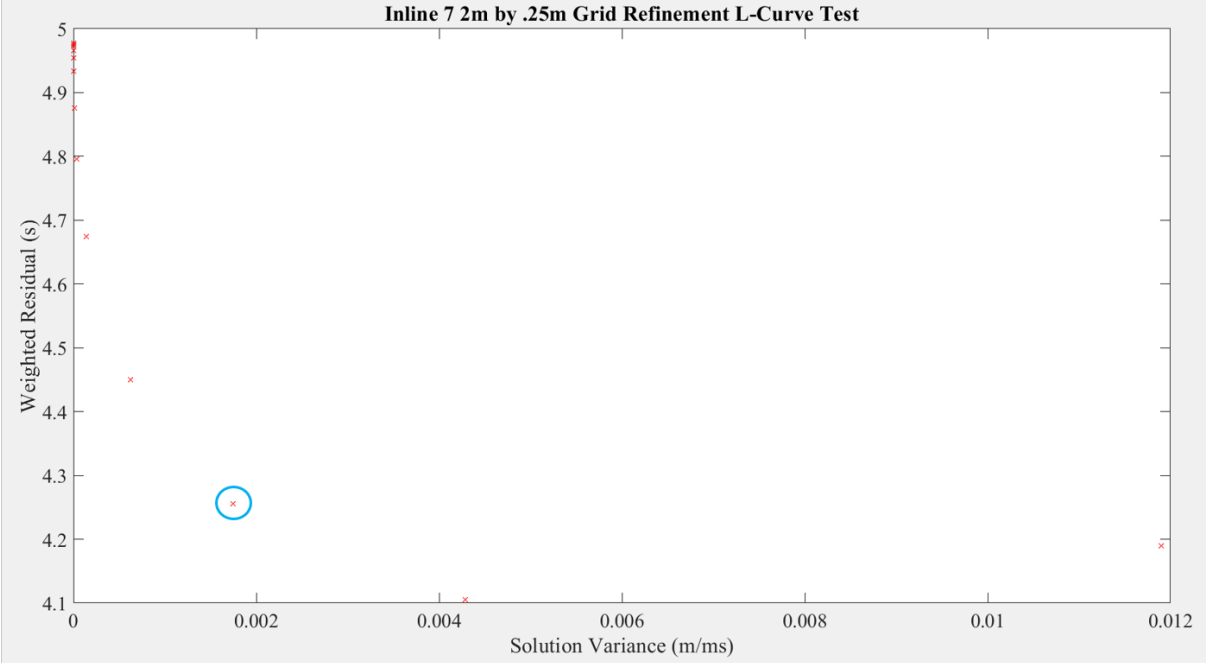

***Figure 5.13**: Displays the L-Curve Test of the 2 m by .25 m Grid Refinement of the Inline 7 Inversion model. The small red stars are the results of different damping values calculated by Simulr16, and the goal of doing the Damping Test is to identify the elbow point of the curve. The elbow point for this test is the 11th damping value, is shown by the light blue circle, and its value is 1.*

The Inversion process is then run with the damping value, which then compares the goodness of fit between the observed (FBPs) and predicted data. This is called the RMS Residual which is calculated by Simulr16 (Bleibinhaus 2003) as:

$$e_{rms} = \sqrt{\frac{1}{N}\sum_{i=1}^{N} e_i^2}$$

If the RMS is very large the model does not accurately explain the survey data. After each inversion iteration the RMS between the forward model and the observed data is calculated by Simulr16, which can be saved and displayed. If the starting model is not well defined, it may take many inversion iterations for the program to reach an acceptable RMS value. If the starting model is completely incorrect the RMS will never reach an acceptable level. This is an effective method of QA/QC built into the Simulr16 program. As it demonstrates that a

starting model is poorly defined for the provided data, if after the standard number of iterations, approximately 12, Simulr16 cannot reach close to value calculated by the Manual RMS Method of section 5.4.1. A comparison between the 2 m by .25 m IL7 starting model and an initial IL7 Test starting model utilizing the same data and node density/placement, but not the same velocity model is show in table 5.2 in conjunction with Figure 5.14.

***Table 5.2**: Model Comparison for Siumulr16 RMSE Calculation*

Iteration Number	2m by .25m IL7 RMS value	IL7 Test RMS value
0	4.21	45.54
1	3.79	44.58
2	3.67	43.59
3	3.61	42.43
4	3.56	40.99
5	3.53	39.31
6	3.49	37.58
7	3.46	35.36
8	3.44	33.14
9	3.42	30.31
10	3.40	27.15
11	3.38	23.66
12	3.37	20.17

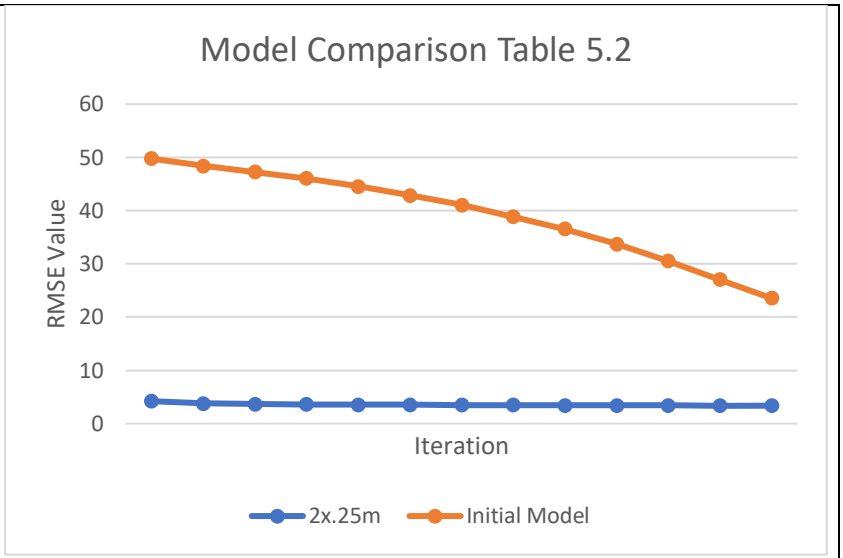

Figure 5.14: Visual display of Table 5.2 information.

5.5 Simulr16 2D vs 2.5D

Simulr16 can be run in 2D, 2.5D, and 3D modes. The In-Line 7 profile is created in both 2D and 2.5D to see if there is a substantiative improvement on the Simulr16 calculated RMS Errors. This is considered as a possible error vector in the Thesis' tomography due to the approximately 1-meter offset of the Shot Lines from the In-Lines, in conjunction with the relatively small and dense layout of the survey. Thus, the need for a QA/QC check in this particular step of the Thesis. In this method of QA/QC every parameter including the same original model, damping value, and FBPs were used, with the only variable being the Simulr16 2D/2.5D option. These two tomography attempts were run to determine if it is worth the greatly increased calculating power and time to acquire a discernibly lower RMSE value on this profile. The better option, between the 2D or 2.5D method, is then applied to the grid densification process.

Displayed on Table 5.3 are the two different model and parameterizations between the 2D and 2.5D. In these 2D vs 2.5D inversion processes the exact same In-Line, FBPs, original node density and placement, starting velocity model, and damping values were utilized. This outcome indicated that the significantly increased duration of the inversion process calculation, which is required for the 2.5D method, is not worth being an acceptable trade-off for the small to negligible improvement of RMSE values during the node densification process.

***Table 5.3**: Simulr16 2D vs 2.5D IL7SL8 Comparison.*

Option	2D RMSE	2.5D RMSE	RMSE Difference
IL7SL8 Model 1	4.523	4.449	0.074
IL7SL8 Model 2	3.965	3.961	0.005

6: Results

Figure 6.1 demonstrates the final locations of the three 2D profiles that were used in the inversion processes to develop the models. None of these profiles, including the 3D profile, include the elevation in the inversion process or model. After QC QA of the data several 2D tomography profiles were calculated. These are the Soft Rock Cross Line on CL 11 and the Hard Rock Cross Line on CL 35. Both Cross Line profiles have an independent starting model designed in Simulr16 as defined in Section 3.4. The information gained from these two CL profiles is then utilized to generate a starting model for the 3rd 2D profile, the In-Line Profile. This IL profile is located on Receiver Line 7 Utilizing Shot Line 8's activations. It is titled as IL7SL8 in this Thesis. The IL7SL8 profile then undergoes two independent grid densification processes to more completely characterize the subsurface. The selected Grid Densification Model is then used to form the starting velocity model for the 3D inversion process. This workflow is designed to develop the most accurate as possible starting model for the final 3D inversion.

Figure 6.1*: Map view of the survey site [Image @ 2023 Maxar Technologies]. Blue circles are the GPS coordinates of the receiving geophones. Red circles are the GPS coordinates of the shot locations. The yellow line represents the profile of Hard Rock Cross Line 35 in the survey. The orange line represents the profile of Soft Rock Cross Line 11 in the survey. The pink line represents the profile*

of the In-Line 7 2D profile. The specific locations of these profiles are chosen because of the final location of the DT-1B drill site. This location, alongside the original proposal, are both approximately on the In-Line 7. The Hard Rock and Soft Rock profiles are to display the different lithologies along the length of In-Line 7.

6.1 Hard Rock and Soft Rock Cross-Line 2D Profiles

6.1.1 Soft Rock Cross Line Profile

The Soft Rock Cross Line profile lies on Cross Line 11, thus each shot number 4 on every SL. In this profile each shot line has only 6 active receivers in the inversion process due to the snake lay out of the survey and the Roll-ons. Figure 6.2 displays the starting velocity model of the Soft Rock inversion process. Figure 6.3 displays the resultant inversion model of the Soft Rock CL. This line is then used to help create the IL7SL8 velocity profile inversion starting model. It also proves that the soft rock portion of the survey does not exceed approximately 500 m/s in velocity. The Simulr16 calculated RMSE is 3.52, on iteration 11. Table 6.1 displays the iterative inversion steps of the Soft Rock Cross Line profile. Which is comparable with the hand calculated 3.54 RMSE and in conjunction with the a priori data gathered from the field course. Thus, this inversion model can be considered fairly accurate for the subsurface.

***Table 6.1**: Iterative Inversion Steps for Soft Rock Cross Line.*

Iteration Number	RMS Value
0	10.836
1	6.012
2	4.061
3	3.790
4	3.639
5	3.655
6	3.624

7	3.592
8	3.586
9	3.590
10	3.533
11	3.520

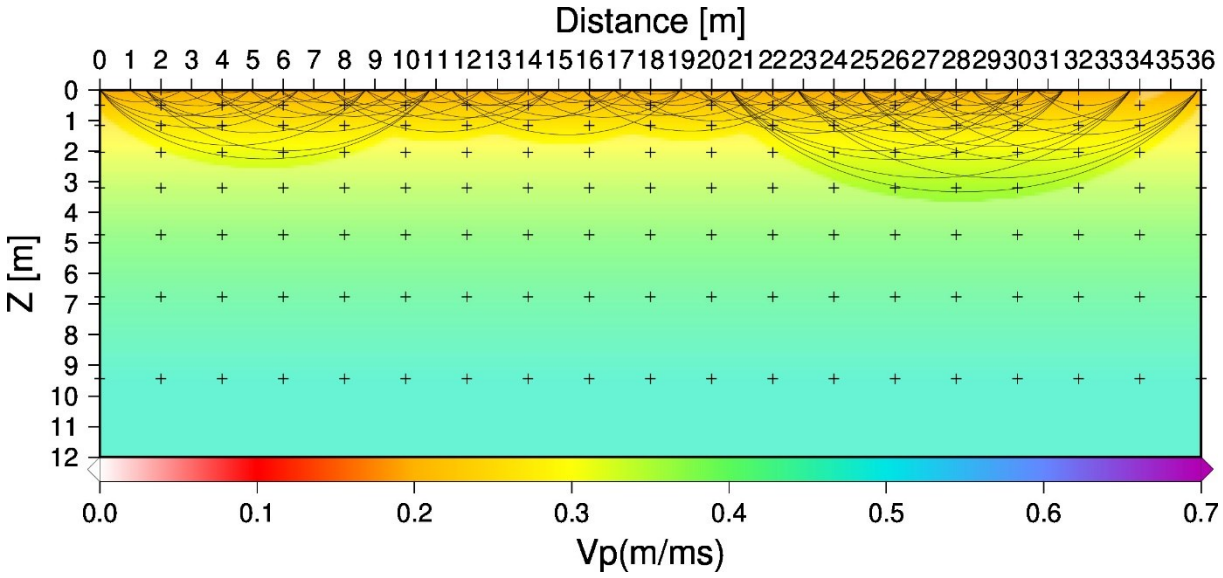

***Figure 6.2**: The starting model of the Soft Rock CL. The origin of this profile in this figure is co-located with SL1 and RL 1. The small black crosses are the locations of the nodes that have a 2 meter by 1 meter spacing. The thin black lines represent the calculated ray paths. The velocities are a steady vertically decreasing gradient. The larger depth reached by ray paths towards meter 36 is explained by the fact that SLs 17-19 increase in offset compared to their active receivers.*

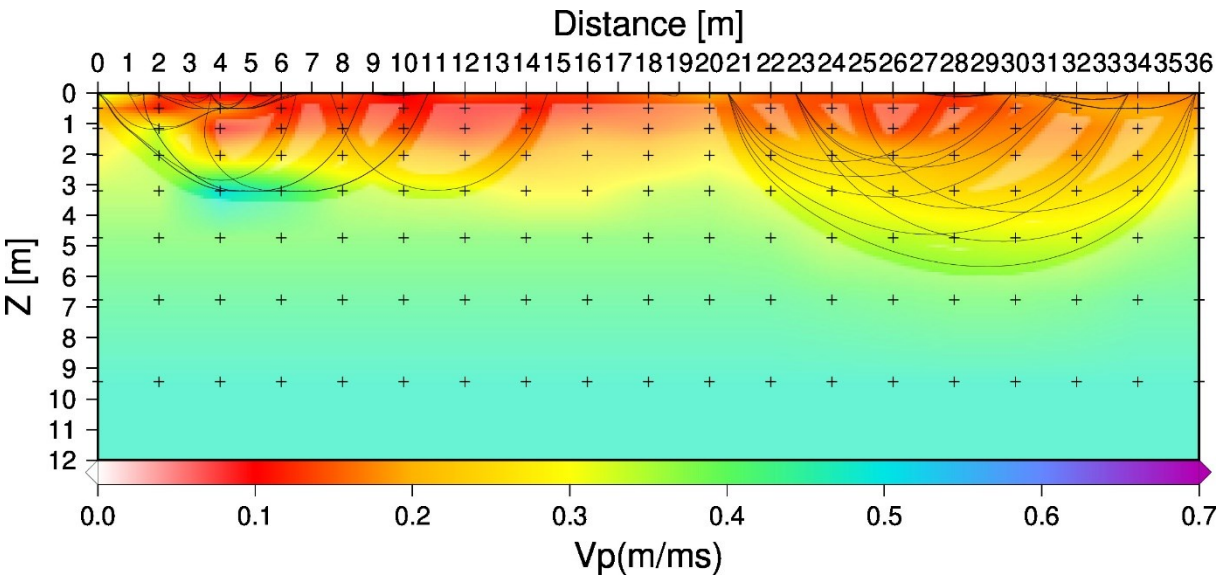

***Figure 6.3**: This is iteration 11 of the inversion profile model of the Soft Rock CL. The origin of this profile in this figure is co-located with SL 1 and RL 1. The small black crosses are the locations of the nodes that have a 2 meter by 1 meter spacing. The thin black lines represent the calculated ray paths. They reach a maximum depth of 6.25 meters from shot line 18 similar to Figure 6.3, however their depth has increased to reach similar velocities that they reached in the initial step. This inversion model displays that the southern part of the survey has a shallower outcropping of harder rock, but none of the soft rock exceeds 500 m/s in the soft rock portion of the survey.*

6.1.2 Hard Rock Cross Line

The Hard Rock Cross Line has a similar layout as the Soft Rock CL except that it profiles Cross Line 35, thus shot number 10 on every SL. Figure 6.4 displays the starting velocity model of the Hard Rock inversion process. Figure 6.5 displays the resultant inversion model of the Hard Rock CL. The entire CL, excepting the center 10-meter portion, displays a very shallow hard rock continuity similar to a cliff face. The p-wave velocities reach a maximum of approximately 3,000 m/s. The Simulr16 calculated RMSE is 3.26, for iteration 10, which is close to the hand calculated 3.54 RMSE. Table 6.2 displays the iterative inversion steps of the Hard Rock Cross Line profile.

***Table 6.2**: Iterative Inversion Steps for Hard Rock Cross Line.*

Iteration Number	RMS Value
0	5.128

1	4.170
2	3.801
3	3.626
4	3.530
5	3.462
6	3.409
7	3.364
8	3.326
9	3.294
10	3.263

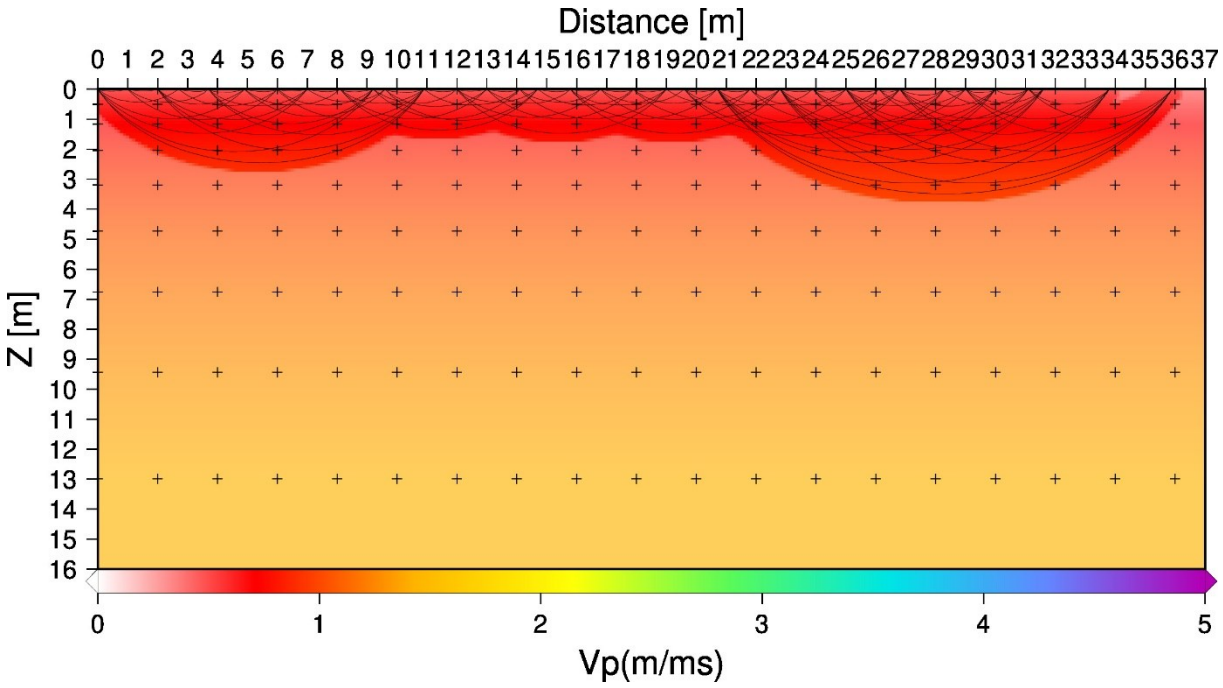

***Figure 6.4**: The starting model of the Hard CL. The origin of this profile in this figure is co-located with SL1 and RL 1. The small black crosses are the locations of the nodes that have a 2 meter by 1 meter spacing. The thin black lines represent the calculated ray paths. The velocities are a steady vertically decreasing gradient. The larger depth reached by ray paths towards meter 36 is explained by the fact that SLs 17-19 increase in offset compared to their active receivers.*

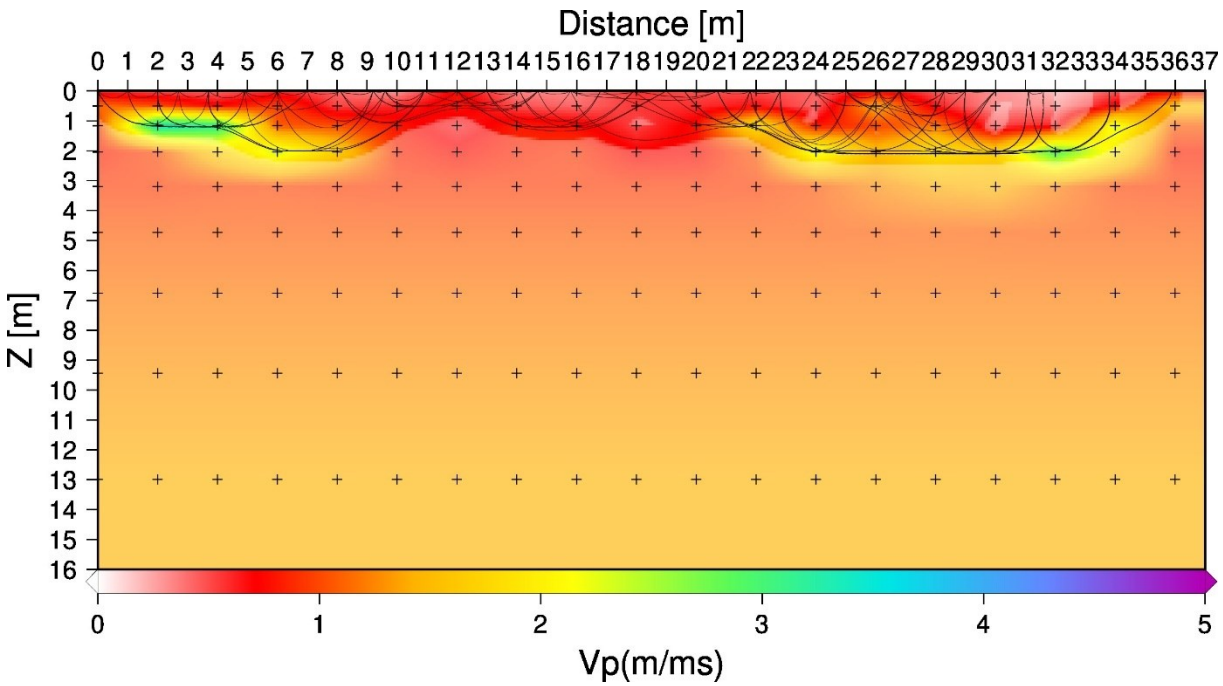

***Figure 6.5**: This is the inversion profile model of the Hard Rock CL. The origin of this profile in this figure is co-located with SL 1 and RL 1. The small black crosses are the locations of the node with a 2 meter by 1 meter spacing. The thin black lines represent the calculated ray paths and reach a maximum depth of 2 meters, which is a shallower depth than originally displayed in Figure 6.4. The hard rock is quite clear and shallow in depth in comparison to the surface, notably on the IL 1 and IL 16 portions of this section of the survey, with a maximum around 3,000 m/s. The hard rock dives in depth towards the center of the profile beyond the reach of the CL inversion process.*

6.2 In-Line 7 2D Profile

The final 2D In-Line profile is the result after a series of node densifications. The method to do this is based upon taking into account the size of the survey, 45 m in length, and determining what would be considered the first overdetermined inversion model. This overdetermined inversion model is considered a node once every meter along the x direction (the length of the inversion model), and a node every .125 meters in depth. This inversion model is overdetermined because Simulr16 itself recommends having around at least two receivers for every one node of the initial inversion model. The final model from each densification step is then used as the starting model for the inversion process to be run upon in the subsequent densification step. This process uses a Matlab code that takes the final iteration velocity model of the previous densification step from Simulr16 and the node cartesian coordinates of the new densification step, combines them, and then creates a velocity model

which is then reintroduced into the starting model of the new densification step. This model is then run with the new velocity model and the new node density, this creates the final iteration model which is then used in the subsequent new densification step. From there the density of the grid is halved for five steps. This process for both the High Velocity Grid Densification (HVGD) and the Low Velocity Grid Densification (LVGD) is displayed in Table 6.3 and Table 6.4, respectively.

There are two differences between these two grid densification processes: firstly, the initial model's velocity gradient, and the middle densification steps in Table 6.3 have an RMSE stop, where each iteration has a stopping value if the current and the previous iteration have too small of a different RMS value it stops the Inversion process there. Table 6.3 is the first densification process and starts from 50 m/s and then reaches a maximum velocity of 4,850 m/s. This velocity gradient is developed by both the Hard Rock and Soft Rock CL inversion processes which started around 50 m/s and went to the maximum value of 5000 m/s. Meanwhile Table 6.4 is the Low Velocity gradient that is theorized to prevent the inversion iteration process of dragging the high velocity rocks into the low velocity sediment, which is known to be incorrect due to a priori data. The velocity gradient for this densification process starts at 50 m/s and reaches a maximum velocity of 1,250 m/s.

***Table 6.3**: 2D High Velocity Grid Densification (HVGD) Parameters and Steps.*

	1st densification step	2nd densification step	3rd densification step	4th densification step	5th densification step (over determined)
Distance between X nodes (m)	16	8	4	2	1
Distance between Z nodes (m)	2	1	0.5	0.25	0.125
Final Iteration #	7	1	1	12	8
RMS Error	9.2	6.24	5.16	3.27	2.78

***Table 6.4**: 2D Low Velocity Grid Densification (LVGD) Parameters and Steps.*

	1st densification step	2nd densification step	3rd densification step	4th densification step	5th densification step (over determined)
Distance between X nodes (m)	16	8	4	2	1
Distance between Z nodes (m)	2	1	0.5	0.25	0.125
Final Iteration #	20	20	12	12	12
RMS Error	5.35	4.12	3.77	3.37	2.91

Figures 6.6, 6.7, and 6.8 are various steps of the HVGD. All of these have the same scale between each Figure, and all three of the Figures exclude the topography of the survey. Figure 6.6 is the initial model of the densification process prior to even the first densification step. This includes only the initial velocity model of the entire process. It has 16 horizontal meters by 2 vertical meters node spacing. Figure 6.7 is the 2nd Densification Step of the HVGD. It has node spacing of 8 horizontal meters by 1 vertical meter, it underwent two iterations, and had the final iteration RMSE of 6.24. Figure 6.8 is the 4th Densification Step, and is the last step before the model becomes over determined. It has a node spacing of 2 horizontal meters by .25 vertical meters, underwent twelve iterations, and had the final iteration RMSE of 3.27.

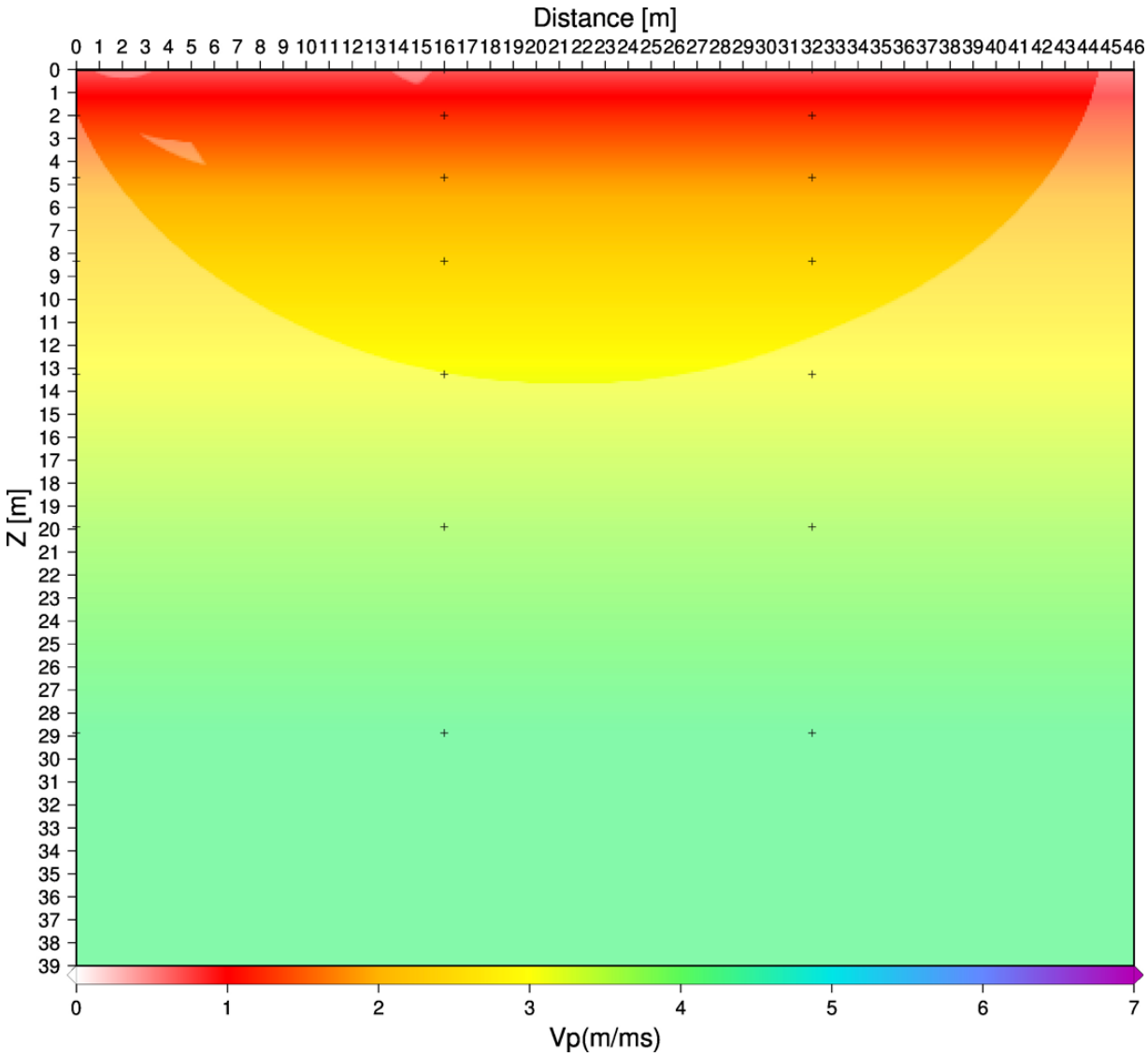

***Figure 6.6**: The initial velocity model of the HVGD. The small black crosses represent the locations of the nodes, with a 16 meter by 2 meter spacing. 0 m in this image is the side of the survey closest to the hill and is closest to receiver 40 and shot 12. The ray paths are not shown, however the lighter part of the survey at the top is where they would be displayed. The entire image slowly increases the velocity evenly throughout the profile. It is designed to max out at approximately 4,750 m/s from the Hard Rock CL that indicated that the maximum hard rock velocities were around 4,500 m/s. The rock velocities have the possibility of reaching up to 7,000 m/s however due to prior knowledge about the survey area this is known to be infeasible. The profile is designed to go to the depth of 39 meters due to several test run inversion processes reaching down to the depth of 29 meters with a safety margin of 10 meters.*

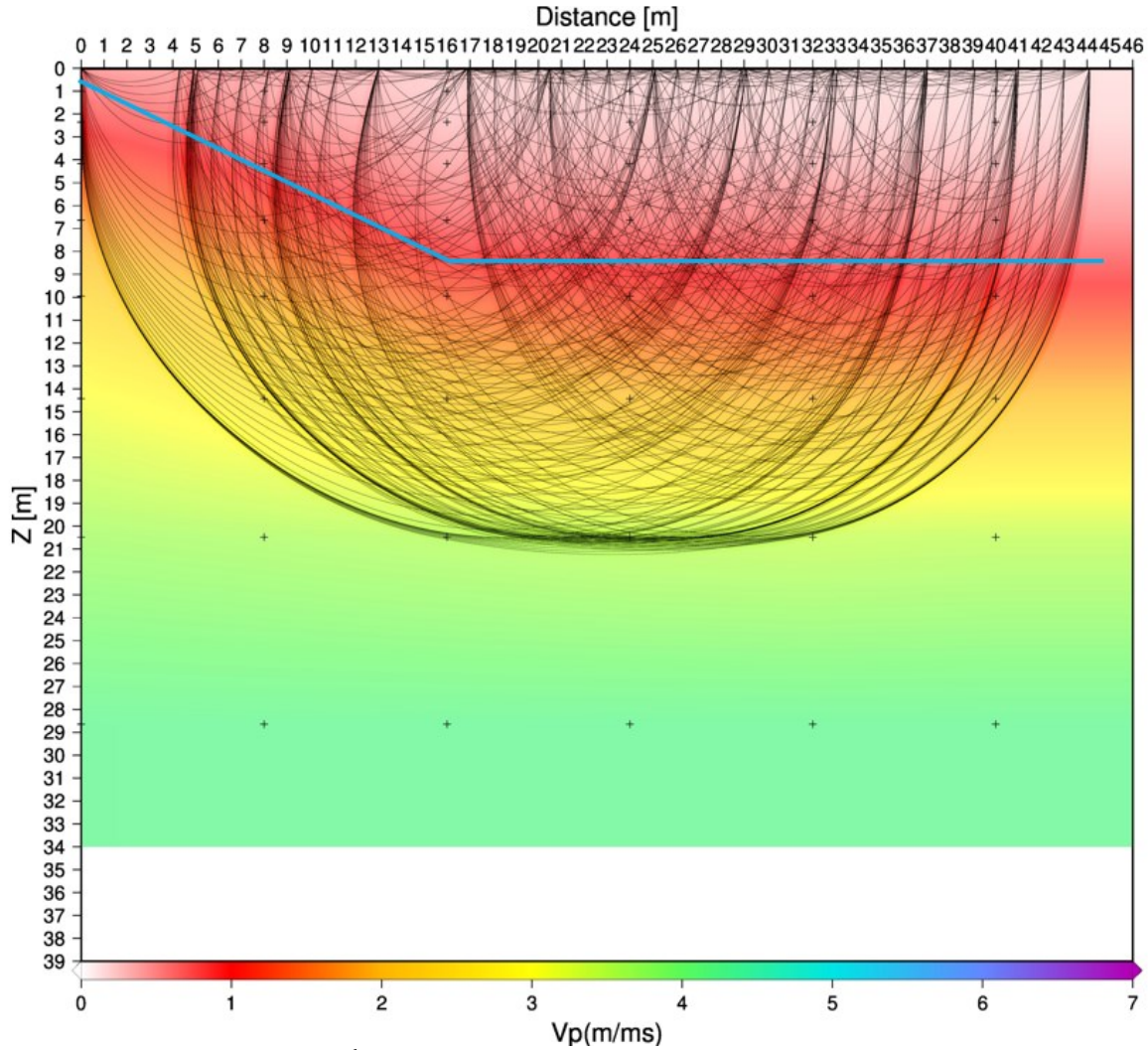

Figure 6.7*: This figure is the 2nd Densification Step of the HVGD. This figure has the same vertical and horizontal scale/dimensions as Figure 6.6. The small black crosses represent the locations of the nodes with an 8 meter by 1 meter spacing. Exactly like Figure 6.6. 0 m in this image is the side of the survey closest to the hill and is closest to receiver 40 and shot 12. The thin black lines are the ray paths, and reach down to a depth of 21 meters in almost perfect semi-spherical trajectories. The blue line indicates the trend to of the inversion model which starts at 0 m distance has begun to drag the higher velocities up closer to the surface, and lower velocities have been made much thicker and continues flat toward the 46 m end of the inversion model. The white gap at the bottom is necessary to keep the same scale as Figure 6.6.*

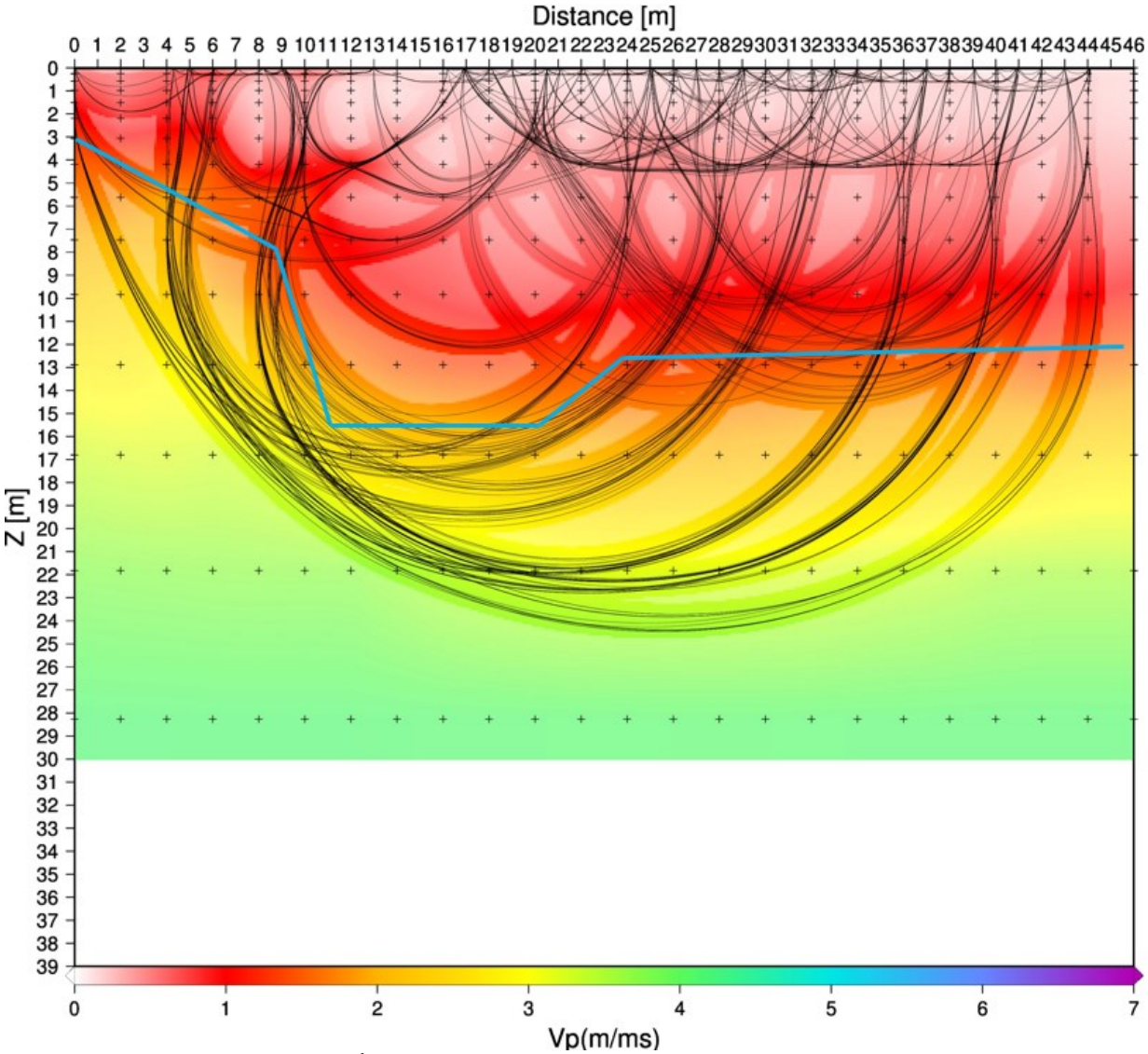

***Figure 6.8**: This Figure is the 4th Densification step of the HVGD. This figure has the same vertical and horizontal scale/dimensions as both Figure 6.6 and Figure 6.7, as well as 0 m being where receiver 40 and shot 12 are located. The black lines are the ray paths, and reach a maximum depth of 25 meters. The blue line indicates the velocity trend of the inversion model. Near 0 m the higher velocities are closer to the surface slowly increases in depth, and then drastically drops down similar to the cliff face to the north-west of the survey area. It then decreases in depth, and continues near horizontal with a slight positive incline towards the end of the inversion model near the footpath. The white gap at the bottom is necessary to keep the same scale as Figures 6.6 and 6.7.*

Figures 6.9, 6.10, and 6.11 are various steps of the LVGD. All of these have the same scale between each Figure and the previous HVGD. Similar to the HVGD the three Figures exclude the topography of the survey. Figure 6.9 is the initial model of the densification process prior to even the first densification step. This includes only the initial velocity model of the entire

process. It has 16 horizontal meters by 2 vertical meters node spacing. Figure 6.10 is the 2nd Densification Step of the LVGD. It has node spacing of 8 horizontal meters by 1 vertical meter, it underwent twenty iterations, and had the final iteration RMSE of 4.12. Figure 6.11 is the 4th Densification Step, and is the last step before the model becomes over determined. It has a node spacing of 2 horizontal meters by .25 vertical meters, underwent twelve iterations, and had the final iteration RMSE of 3.37.

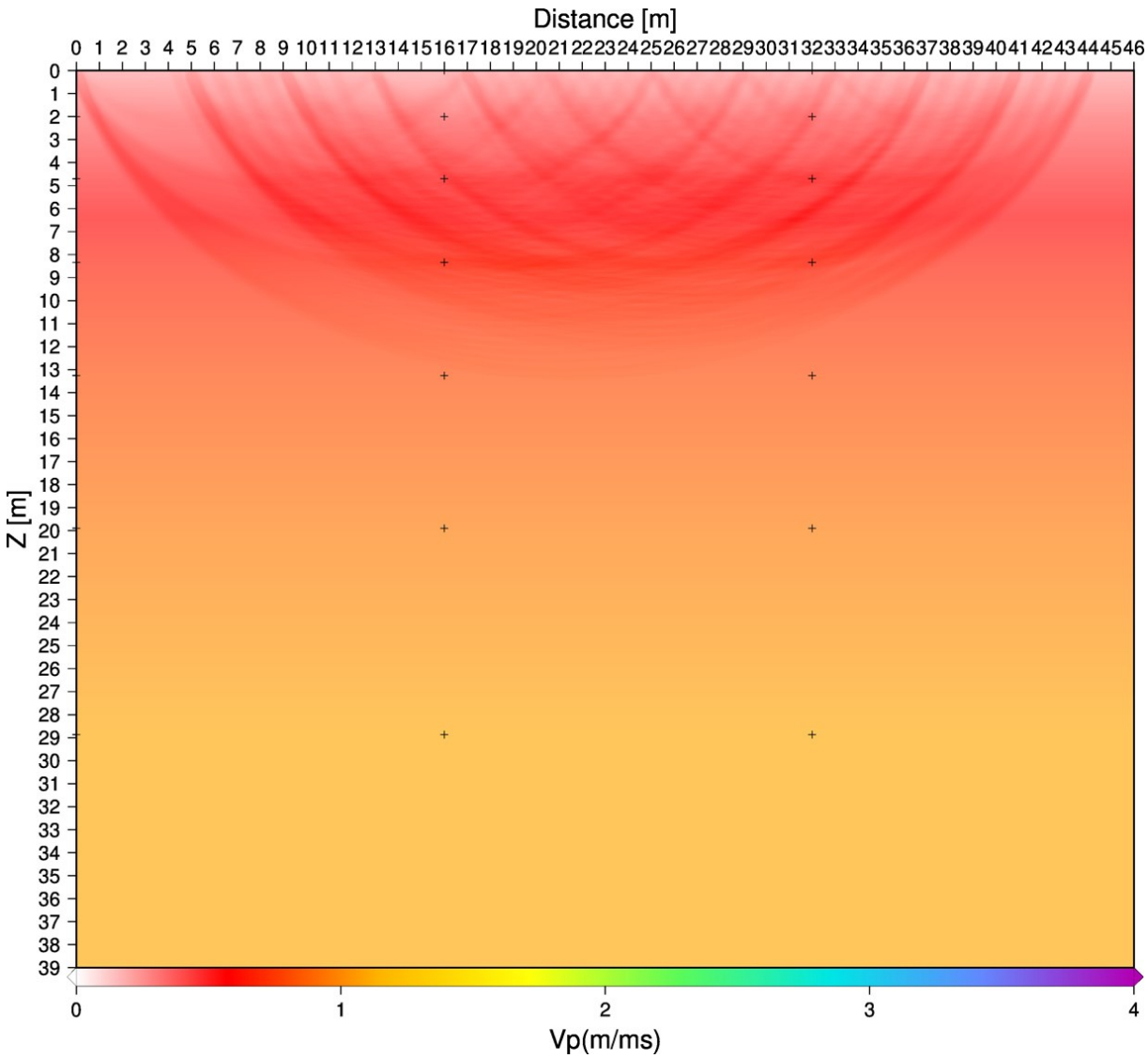

Figure 6.9*: This is the LVGD initial step. Black crosses are node locations, with a 16 meter by 2 meter spacing. 0 m in this image is the side of the survey closest to the hill and is closest to receiver 40 and shot 12. This inversion process' starting maximum velocity is approximately 1250 m/s, and allows a maximum possible depth of 39 meters.*

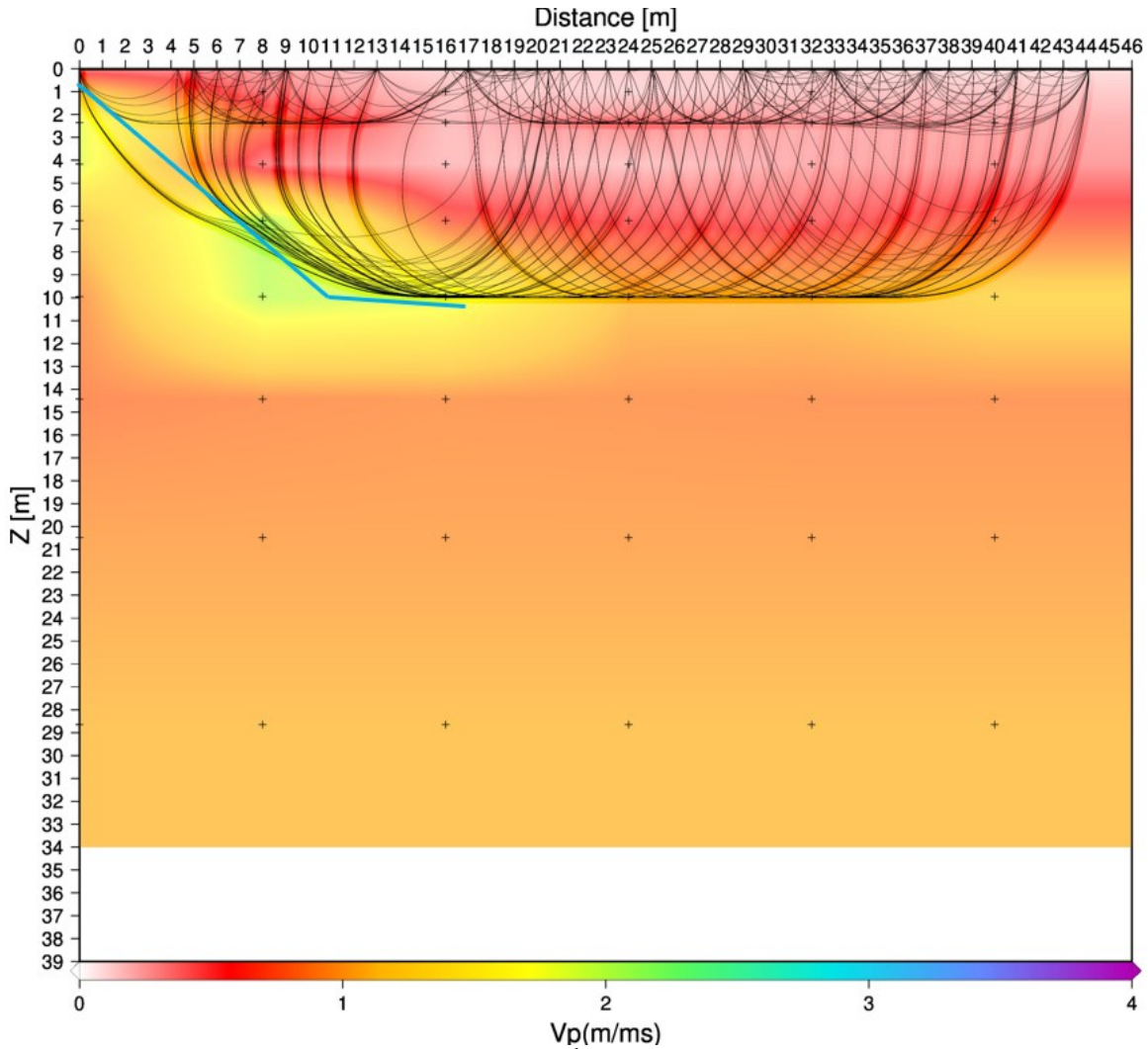

***Figure 6.10**: This is the inversion model of the 2nd Densification Step of the LVGD. The blue line denotes the hard rock faster velocities located in the North-West portion of the survey has begun to develop an angled trend that leads to a bench. This is a similar trend to the cliff face to the North West of the survey. The thin black lines represent the ray paths calculated by the inversion process. The hard rock lithologies do not increase back towards the surface similar to what would be seen if this is a river bed subsurface. That scenario is seen in the HVGD. None of the steps in the LVGD have any forced method of limiting the depth of the ray paths. Thus, the LVGD is itself developing the much shallower ray paths compared to the HVGD. This is more in line with the fact that traditional depth of knowledge is roughly equal to one fourth of the horizontal displacement. In this survey profile that would be equal to approximately 10 m in depth.*

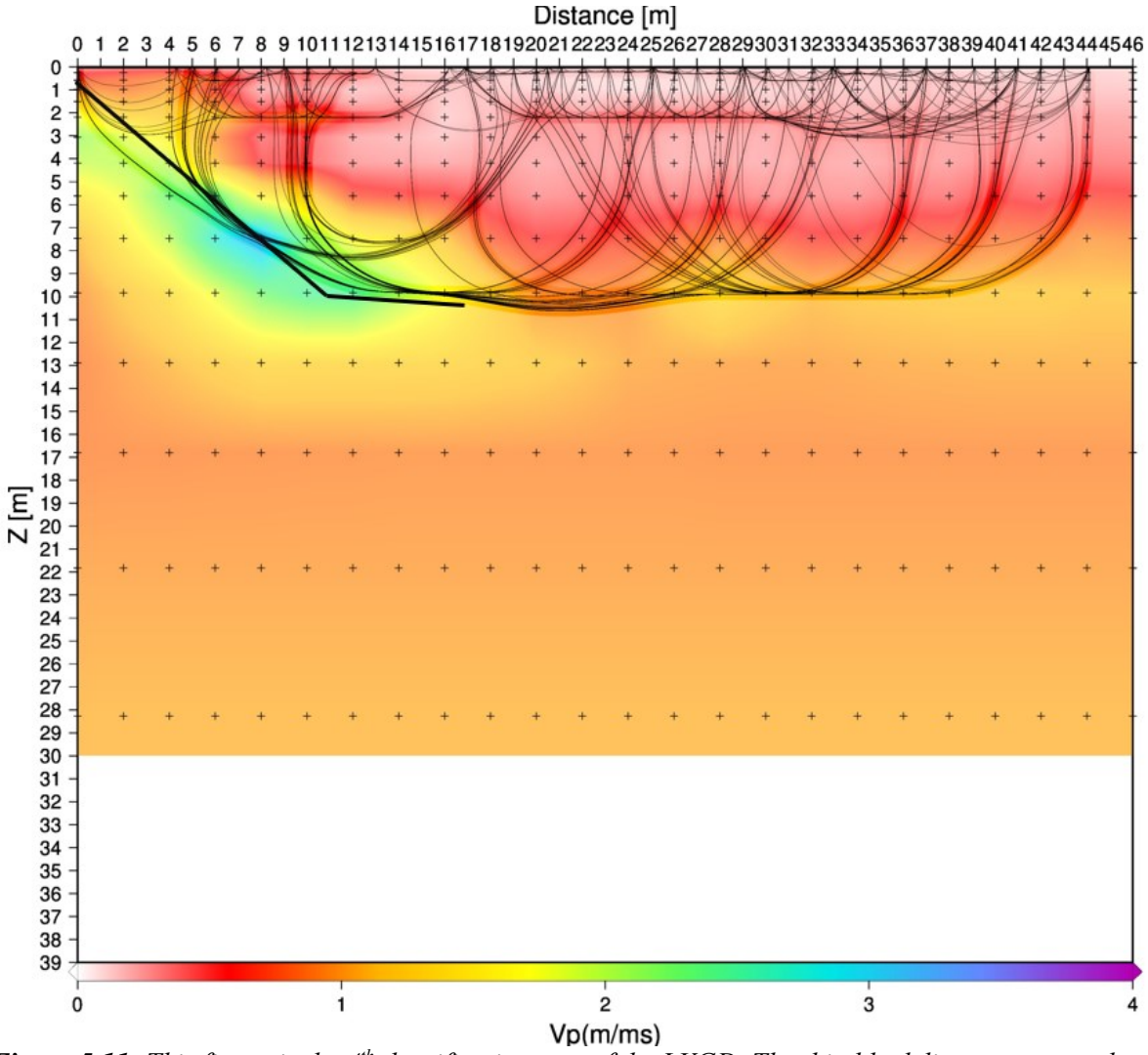

***Figure 5.11**: This figure is the 4th densification step of the LVGD. The thin black lines represent the calculated ray paths and reach a maximum depth of approximately 10 meters, which is a more believably accurate maximum depth for the offset of 46 m compared to the 25 m in Figure 6.9. The black line denotes the hard rock velocities similar to those in Figure 6.10. These have gained the expected higher velocities alongside a greater resolution. They have also become more prevalent towards the surface, which is evident in the field. The faster velocities that are denoted by the black line at 10 m depth are flat or at least not returning toward the surface toward 46 m and the footpath which is evident in Figure 6.8.*

Both the HVGD and LVGD are designed with two objectives in mind: 1) to create a feasible inversion model of the subsurface for the 2D IL 7 profile, and 2) create a valid starting node and velocity model for the 3D inversion process. Thus, it is necessary to compare the final results of them and choose which is preferred moving forward with that option. The LVGD model is the designated choice for several reasons. One of which is the a priori data gathered

from the field work of the IGFW, which will be discussed in the following chapter. This data is more closely represented in Figure 6.11 of the LVGD compared to Figure 6.8 of the HVGD. Another reason is the depths of the calculated ray paths, which follow the standard thought of depth versus horizontal offset more accurately in the LVGD than the HVGD.

6.3 3D Survey Inversion Model

The starting velocity model for the final 3D inversion process is taken from the output of the 4th densification step of the LVGD. The entire survey is broken up into the 6 constituent Roll-ons, of the 6 shot and 6 receiver lines. Then each Roll-on underwent the 2.5D inversion process. The purpose for doing this is the fact that no Roll-on had any effect on the prior or subsequent Roll-on. Thus, doing each individual Roll-on would allow for a more accurate inversion model than the entire model. The statistics of the Roll-ons are shown on Table 6.5. The hand calculated RMSE of Roll-on 4 average is 6.06. The RMSE average from every Roll-on is lower than the hand calculation mentioned in section 5.4.2. Figure 6.12 shows a 3D rendition of the 6 Roll-ons combined, and Figures 6.13 through 6.18 display each individual Roll-on Inversion Model.

Table 6.5*: Roll-on Statistics*

Roll-On	Number 1	Number 2	Number 3	Number 4	Number 5	Number 6
SL Numbers	1-6	3-8	5-10	7-12	9-14	11-16
RL Numbers	1-6	3-8	5-10	7-12	9-14	11-16
Final Iteration Number	15	13	13	7	14	9
RMSE	5.98	4.53	3.59	5.96	4.70	5.10

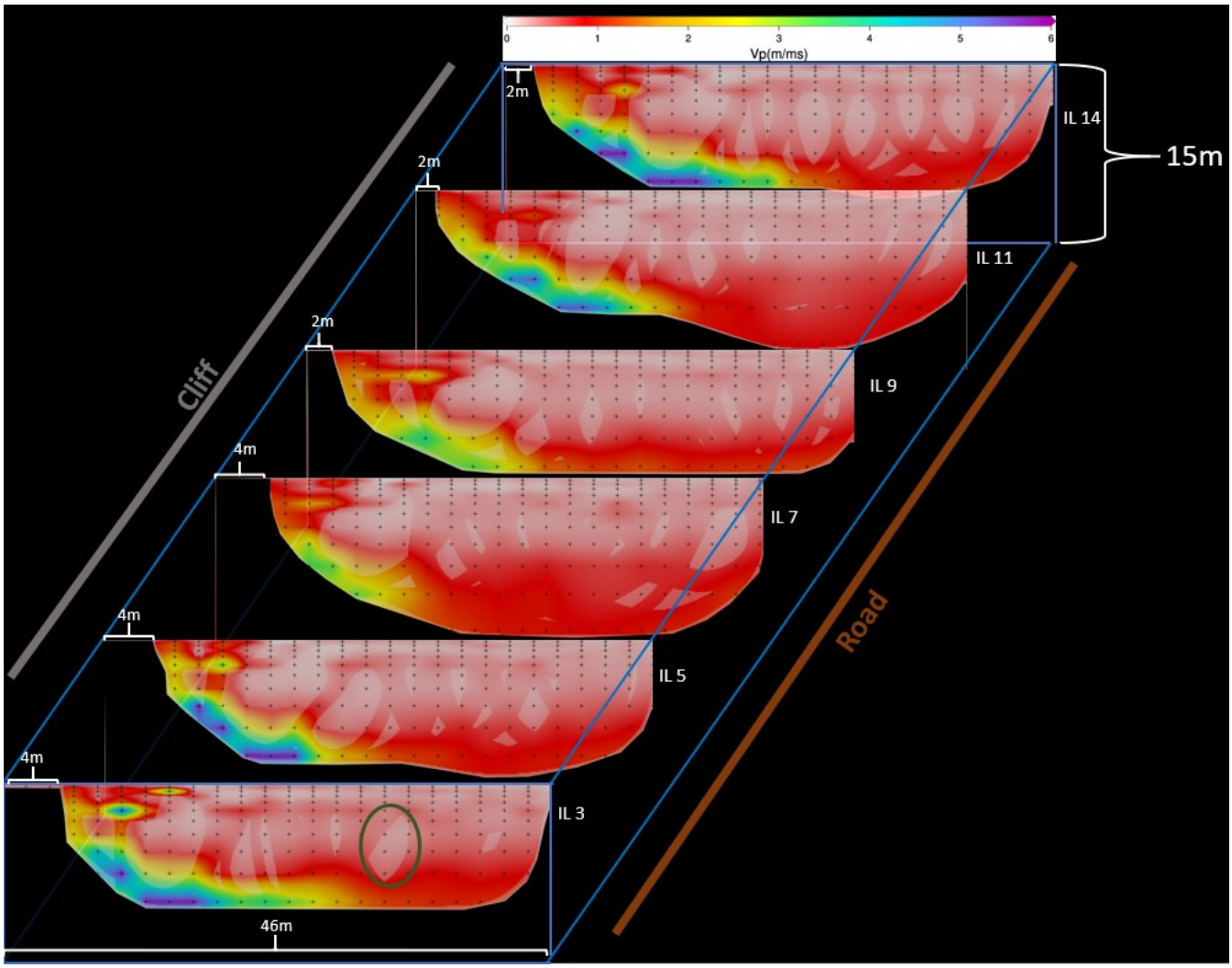

***Figure 6.12**: This Figure is a 3D display of the 6 Roll-on models. The blue lines represent the 3D outer cube of the entire survey. All of the profiles have the same dimensions and velocity color scales. The velocity color scale value is displayed on the top of the IL 14 profile. Each profile has had the areas beyond the reach of any ray paths blacked out so that only the calculated and known information is displayed. The brown line on the right shows the location of the footpath to the Southeast of the survey area, and the grey line on the right shows the location of the cliff face to the Northwest of the survey area. The small black dots represent the locations of the nodes on each of the profiles. The segments of each profile that are lighter in color are areas in which no ray path has been calculated to travel through. One of said areas is encapsulated by a green circle on the IL 3 profile. This 3D profile shows a general trend of faster harder rocks protruding further into the survey area in both the lowest and highest IL/RL segments, with a back step towards the NW cliff in the center of the survey area. This trend agrees with the theorized subsurface lithological division based upon the vegetation in Figure 4.1.*

Figure 6.13 displays the hard rock and soft rock interface of the IL3 profile. This profile is closest towards the beginning of the survey, representing RL and SL 1 through 6.

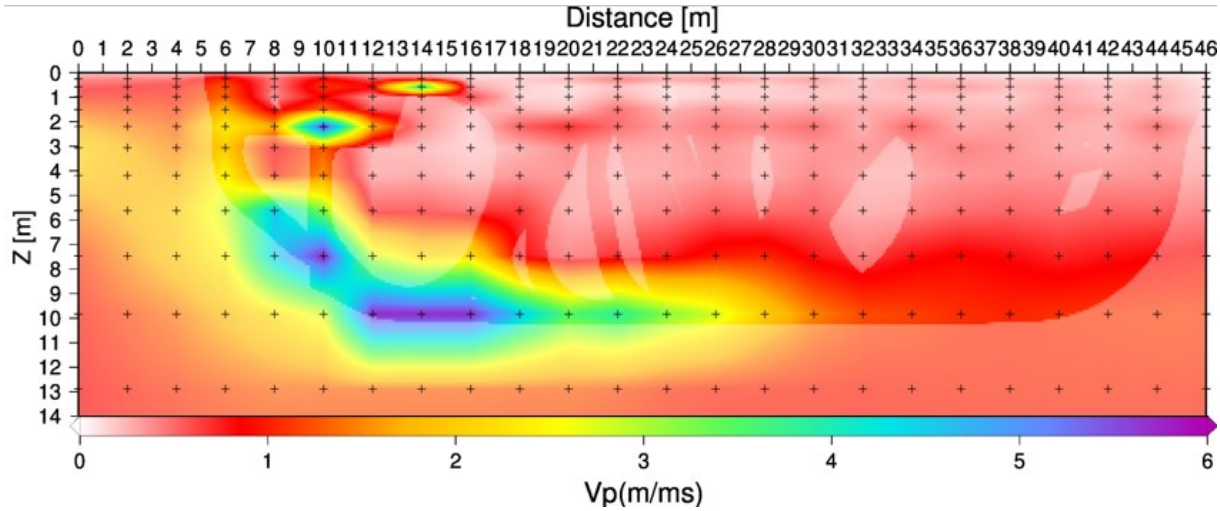

***Figure 6.13**: This figure displays the IL3 profile of the 3D seismic survey. 0 m is the cliff side of the survey, and 46 m is the footpath side of the survey. The hard rock portion of the survey reaches velocities up to 5,750 m/ms, and protrude approximately 28 m into the survey at a depth of 9 m to 10 m. It also has a shallow high velocity shelf like protrusion at approximately 1 m depth that extends 10 m into the survey, which then dives with a near vertical slope to a depth of 7.5 m. The rest of the profile, the Southeast portion near the footpath of the survey and a shallow layer on top of the hard rock, is dominated by the soft sedimentary rock.*

Figure 6.14 displays the subsurface inversion model of the IL5 profile. This profile represents RLs and SLs 3 through 8.

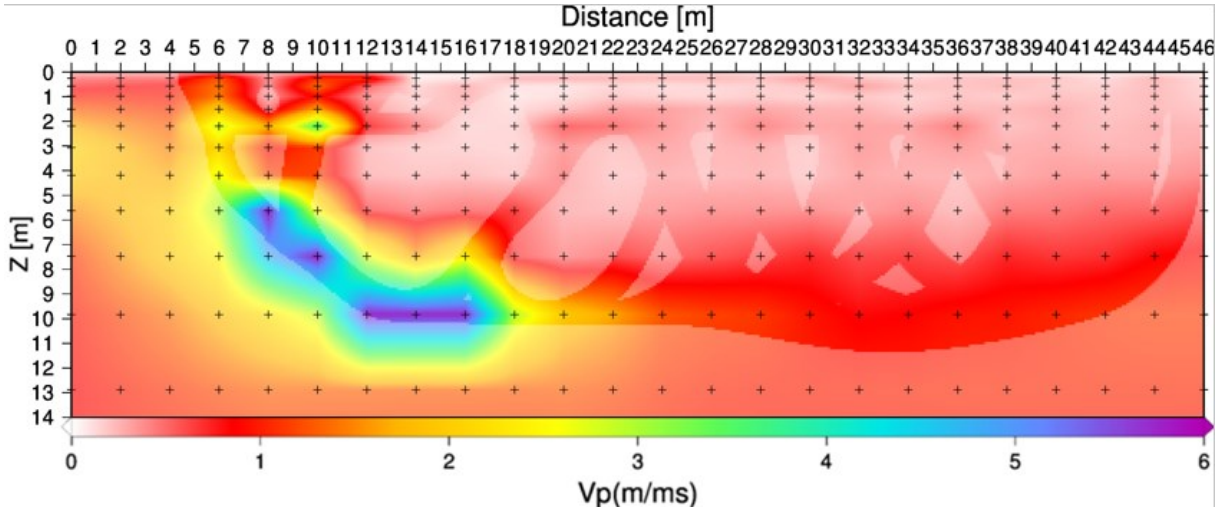

***Figure 6.14**: This figure displays the IL5 profile of the 3D seismic survey. 0 m is the cliff side of the survey, and 46 m is the footpath side of the survey. The hard rock portion of the survey reaches velocities up to 5,750 m/ms, and protrude approximately 20 m into the survey at a depth of 9 m to 10 m. This is an 8 m shorter protrusion of the hard rock into the survey at the same depth of 9 m to 10 m. The previous "high velocity shelf like protrusion" from the IL3 profile is still evident, however it is much less well defined, smaller, and displays lower velocities. The shallow layer on top of the hard rock is thicker than in the IL 3 profile, and dominates the entire Southeast part of the profile.*

Figure 6.15 displays the inversion model of the IL7 profile. This profile represents the RLs and SLs 5 through 10.

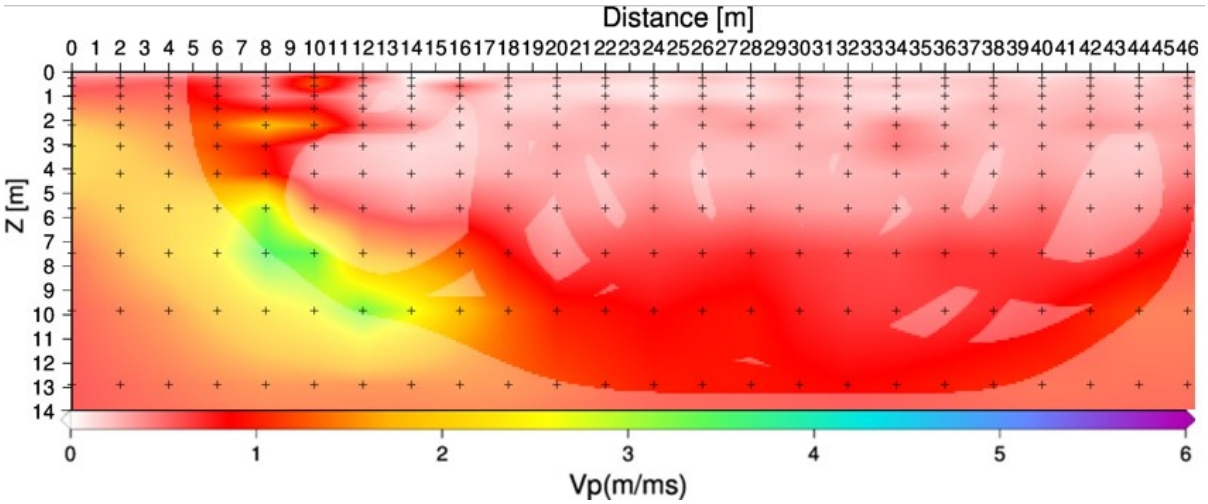

***Figure 6.15**: This figure displays the IL7 profile of the 3D seismic survey. 0 m is the cliff side of the survey, and 46 m is the footpath side of the survey. The hard rock of this profile only reaches approximately 3,500 m/ms, and even then, only smalls segments of this profile, at a depth of 6.5 m to 10 m from 7 m to 14 m of the profile, reaches near these velocities. This hard rock segment has a roughly 45-degree slope, which then flattens out slightly towards the bottom. The rest of the profile is dominated by the soft sedimentary rock. Unlike the 2D profile in Figure 6.11 the hard rock of this profile does not extend past the 18 m, which in Figure 6.11 continues in an almost continuous line until the end of the profile. The previous shallow self like protrusion is nearly non-existent with only a small 2,000 m/ms ovoid remnant. The soft rock portion of this profile is much thicker above, and nearer, the hard rock and the cliff face, up to a depth of 4.5 m and dominates the rest of the profile.*

Figure 6.16 displays the inversion model of the IL9 profile. This profile represents the RLs and SLs 7 through 12.

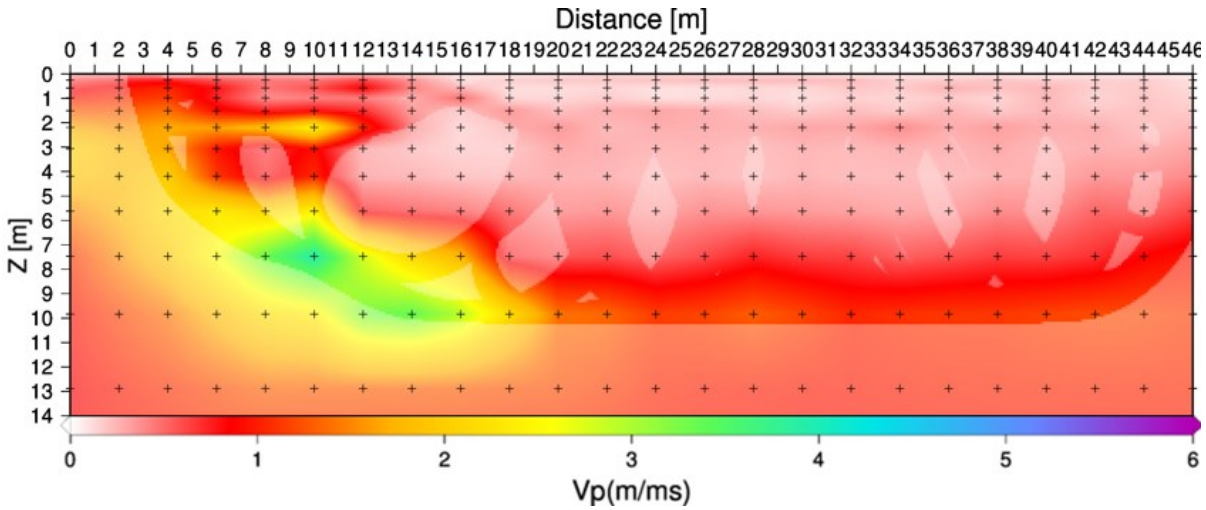

***Figure 6.16**: This Figure displays the IL9 profile of the 3D seismic survey. 0 m is the cliff side of the survey, and 46 m is the footpath side of the survey. Similar to IL7 the maximum hard rock velocities in this profile reach approximately 3,500 m/ms. The hard rock segments, while slightly larger than IL7, are deeper in depth 7 m to 10 m, but do protrude farther, 7.5 m to 16 m, into the profile. It also has a slightly less steep apparent angle of a 40-degree slope. However, the "high velocity shelf like protrusion" that mostly vanished in IL7 is present at a slightly deeper depth, albeit with lower velocities approximately 2,200 m/ms. The rest of the profile is dominated by the soft rock velocities.*

Figure 6.17 displays the inversion model of the IL11 profile. This profile represents the RLs and SLs 9 through 14.

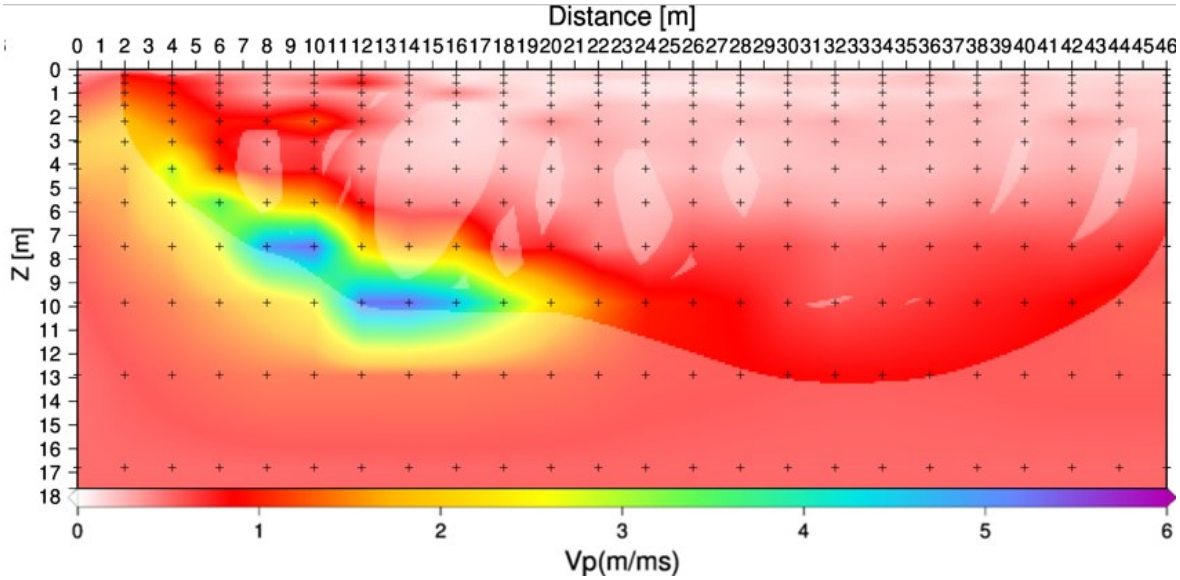

***Figure 6.17**: This Figure displays the IL11 profile of the 3D seismic survey. 0 m is the cliff side of the survey, and 46 m is the footpath side of the survey. The hard rock velocities have increased up to approximately 5,200 m/ms. This is similar to the velocities of IL3 and IL5, and unlike the velocities in IL7 and IL9. These velocities have an almost continuous 30-degree slope starting from 1.5 m to 10 m depth. These velocities also protrude further into the survey up to 21 m. however the "high velocity*

shelf like protrusion" is no longer evident. The soft rock velocities are thicker on top of the hard rock velocities, and dominate the entire South-eastern portion of the profile.

Figure 6.18 displays the inversion model of the IL14 profile. This profile represents the RLs and SLs 11 through 16, and is the end of the survey.

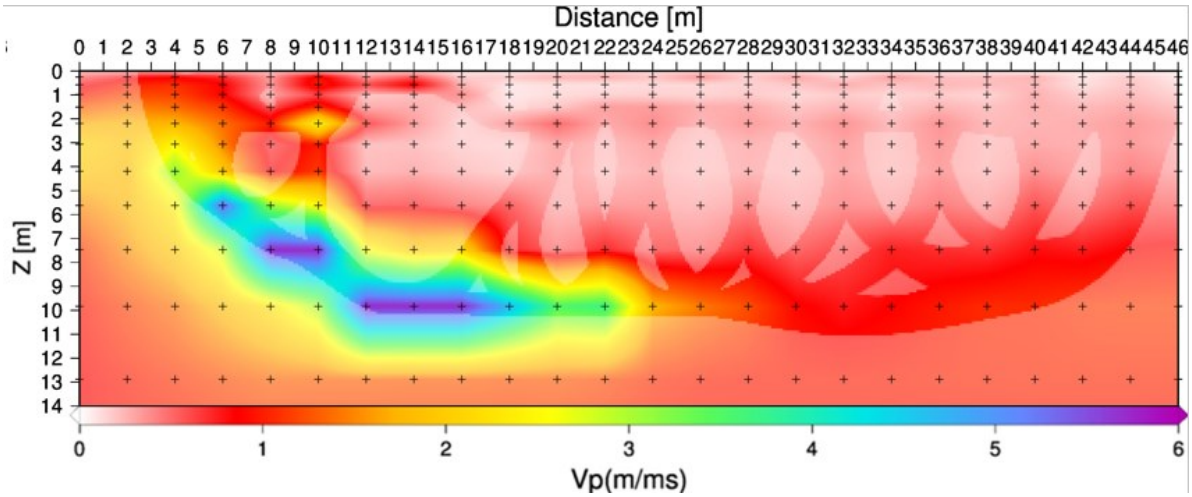

***Figure 6.18**: This Figure displays the IL14 profile of the 3D seismic survey. 0 m is the cliff side of the survey, and 46 m is the footpath side of the survey. The hard rock velocities reach up to 5,750 m/ms, protrude into the survey approximately 24 m, start at a depth of approximately 4 m, continue to 10 m, and have an approximate 30-degree slope. The "high velocity shelf like projection" might exist but the only evidence of it is a well-defined ovoid shape 10 m into the profile. The soft rock velocities are thicker on top and comparable to IL11 and IL9 unlike IL3 and IL5, and dominate the entirety of the South-east portion of the profile.*

The final inversion model demonstrates that the Hard Rock section of the survey protrudes farther away from the cliff, and into the survey area, near the IL1 side and IL16 side of the seismic survey. In-between IL6 and IL10 of the survey the Hard Rock retreats towards the NE cliff face, or CL 40, and is located at a greater depth. This could be attributed to erosion of the cliff when it was exposed to the surface in the past. On all ILs of the survey the Hard Rock starts within 2.5 meters of the surface, and then sharply descend in depth as the survey area progresses farther from the cliff face. It is clear that besides this small extension of the Kinzigite cliff that the survey is dominated by the quaternary sediments. The Soft Rocks also dominate far below the maximum effective depth of the seismic survey.

7: Discussion

7.1 Introduction

This chapter compares the results of the 3D inversion velocity model with the ERT and GPR that were created in the IGFW class. It also discusses the strengths and weaknesses of the Thesis. Figure 7.1 displays the GPS locations of the ERT survey, and Figure 7.2 displays the GPS locations of the GPR survey. Both of these Figures are shown to display how the ERT, GPR, and Seismic surveys compare with one another's locations. Figure 7.3 is a modified Figure 6.10 for ease of comparison between the three different methods.

Figure 7.1*: This figure is a map view of the ERT grid which overlaps the Seismic Survey of the DT-1B drill site. The yellow rectangle approximately displays the Seismic Survey. The dark red dots mark the GPS electrode locations, and the green circles are the GPS remote electrode locations. The Orange arrows present X and Y axis of the grid. ERT Profile Line 1 is represented by the pink line, and ERT Profile Line 20 is represented by the light blue line. The red line indicates the position of the aforementioned 237-meter length 2D profile where it overlaps the seismic and ERT surveys. The blue arrow indicates the footpath that is referred to throughout the survey modified from (Greenwood., 2023)*

***Figure 7.2**: This figure is a map view of the GPR survey area to show where it overlaps with the Seismic Survey of the DT-1B drill site. The yellow rectangle approximately displays the Seismic Survey. The white and black circles represent the GPS locations of the data points gathered from the 250 MHz measurements. The orange arrow indicates what is saved in the data recording as the Uphill direction, and the red arrow indicates what is saved in the data recording as the Downhill direction modified from (Greenwood., 2023).*

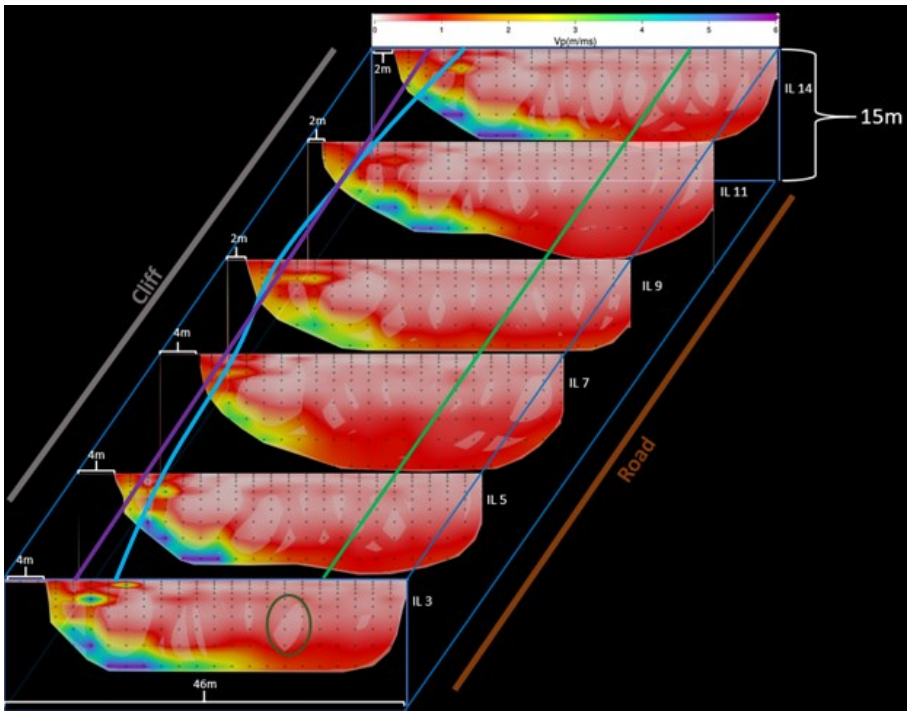

Figure 7.3*: This is a modified version of Figure 6.10 utilized for comparison against ERT and GPR methods. The light blue line represents the surface expression of the TZ. The green line represents the location of the Soft Rock Cross Line. The purple line represents the Hard Rock Cross Line.*

7.2 ERT Comparison to Seismic Velocity Inversion Model

In ERT high resistivities are created by dry sediments and hard rocks, whereas low resistivities are created by water saturated soils. However, quantities of clays (with its surface charge) and metallic ores in dry sediments will reduce apparent resistivities. Due to the importance of water content in the soil, the presence of groundwater can "overprint" the true signals of the lithological target area (Benson., 1984). In regards to the seismic survey the hard rock Kinzigite lithology should have much higher resistivities, and the soft rock quaternary sedimentary lithologies will have much lower resistivities.

Figures 7.4 and 7.5 both display vertical ERT profiles that overlap the seismic survey area that this Thesis used for the inversion process. Figure 7.6 displays ERT depth profiles, similar to a map view, that roughly overlay the seismic survey. Figure 7.7 displays an ERT depth profile similar to Figure 4.1.

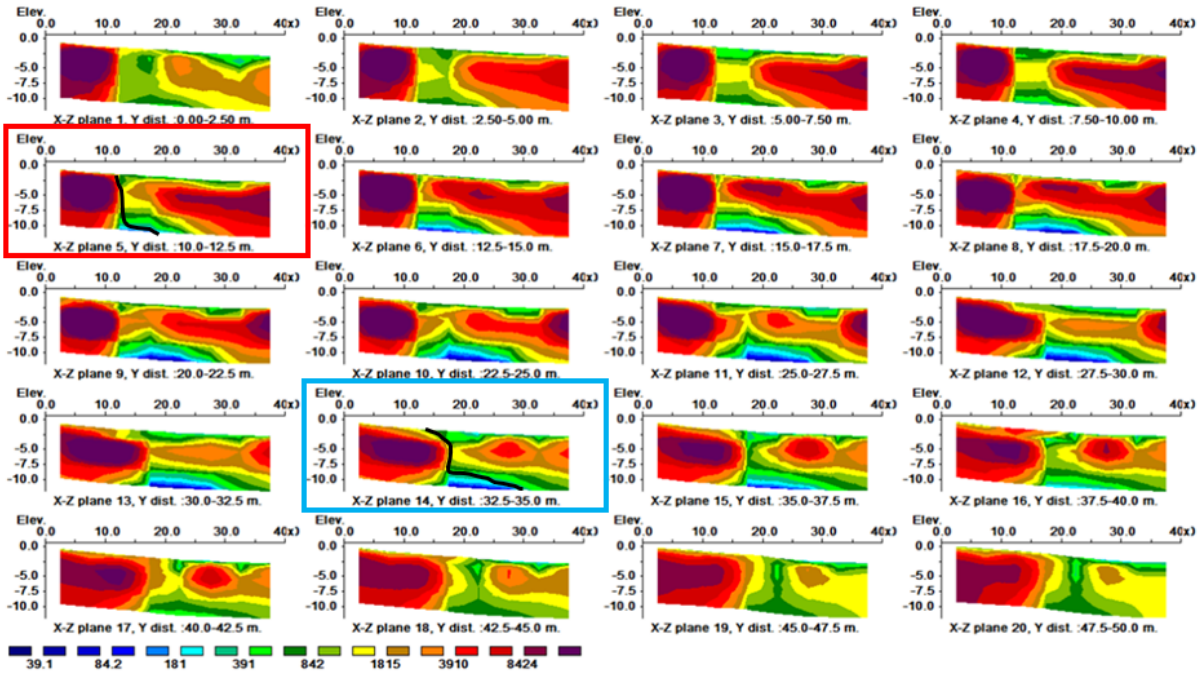

Figure 7.4*: This Figure from (Greenwood., 2023) displays vertical ERT profiles parallel to the IL7RL8 profile utilized in this Thesis. The origin of these slices is the side closest to the Cliff face in all previous Figures in this Thesis, however the final three profiles of this image are outside the seismic survey which underwent the inversion modelling process. The red rectangle roughly corresponds to the same location as IL 5 in Figure 7.3, and the blue rectangle corresponds to the location of IL 11 in Figure 7.3. The red and purple mass on every profile near the origin indicates a region of very high resistivity in the lithological subsurface. Dry impermeable rock typically has high resistivity (Benson., 1984). This correlates to the Kinzigite cliff to the NE protruding into the subsurface of the survey. The area of high resistivity is co-located with the hard rock velocities from the 3D Inversion model that is produced in this Thesis. The TZ, represented by the black lines in the red and blue indicated profiles, slowly increases its intrusion into the survey area from 10 m at the beginning of the survey, up to approximately 17 ms at the end of the survey. This increase agrees with the 3D inversion model of the hard rock protruding further into the survey near IL16*

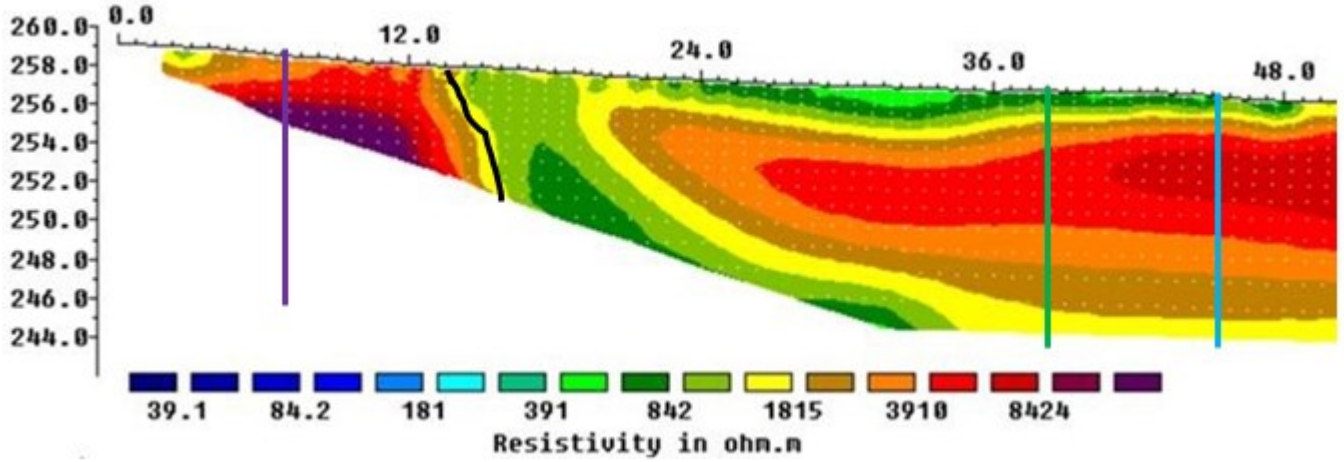

***Figure 7.5**: This figure from (Greenwood., 2023) displays the beginning portion, approximately the same size as the seismic survey, of the 237 m long 2D ERT line. The purple line denotes an approximate location of the HRCL profile, the green line denotes an approximate location of the SRCL profile, and the blue vertical line denotes an approximate location of the termination of the seismic survey on this profile. As in Figure 7.4 a high resistivity mass is located near the origin, and NE cliff face. Kinzigite, as a garnet biotite gneiss, can have resistivities from 200-100,000 ohm-meters (Octova., 2017). This high resistivity area in the ERT in conjunction with the weak internal reflections from the seismic profile is a prime example of weathered hard rock that gradually changes to unweathered hard rock mass discussed in (Butchibabu., 2021). This mass has a sharp slope, denoted by the black line, that dips below the ERT's effective depth just beyond the 12 m mark in the profile. This is in close approximation to the TZ determined by the Thesis. This profile also displays shallow deposits of sedimentary rock that is more conductive on top of the hard rock which are visible in the field and in the 3D Inversion model.*

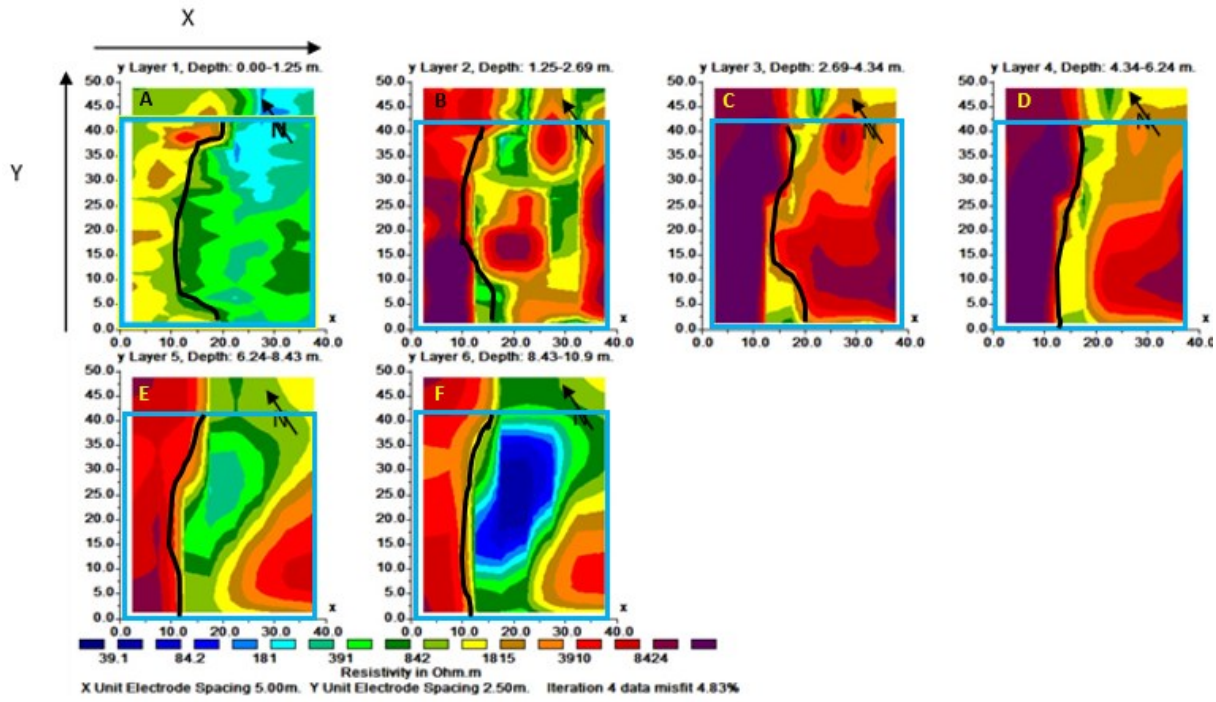

***Figure 7.6**: This Figure from (Greenwood., 2023) displays 6 depth profiles of the IGFW ERT. The shallowest, at 0-1.25 m, is A and the deepest, at 8.43-10.9 m, is F. Each depth profile has the same orientation and North is pointed by the black arrow. The light blue rectangle represents the approximate profile of the seismic survey on each depth profile. On each profile the black line*

represents the TZ. Layers A, B, C, E, and F has an almost interchangeable TZ profile to the profile on Figure 7.3. The IGFW paper states that the high resistivity section on layers C and D is a thin layer of loose sand. Loose sand can have resistivities from 500-5000 ohm-meters (Octova., 2017).

Figure 7.7*: This figure from (Greenwood., 2023) is similar to Figure 4.1. of the vegetation growth from water supply. This is a satellite Image of the complete DT-1B survey area. It has the Depth Layer 1 (0 m-1.25 m depth) overlaid. With the Kinzigite lithologies in yellows and reds, the softer sedimentary lithologies are in greens and blues, and the black line represents the TZ. The drier grasses are clearly growing on top of the Hard Rock segments of the Seismic Survey and the more lush grasses are located in the softer sedimentary lithologies.*

The ERT display of the hard rock portion and the TZ are extremely similar to the Hard Rock CL, IL7SL8, and 3D inversion models. From IL1 to IL6 and IL10 to IL16 the hard rock extends farther into the seismic survey area, and in-between IL6 and IL10 it regresses towards the cliff. If the Kinzigite of the drill site has dry air-filled fractures they will not appear in the ERT if they are not of sufficient size, as stated in (Tao., 2021). However, this does not preclude the Kinzigite mass from possessing a plethora of microfractures.

The ERT has better resolution of the rapid changes with the lithologies in the subsurface, than the resultant Simulr16 inversion process model. The better resolution is nothing surprising,

yet the comparison between the velocity model produced by Simulr16 and the ERT helps to display that the possible model uncertainties of contacts between bedrock and unconsolidated materials, such as the quaternary sediments, discussed in (Tao., 2021) were not apparent in the DT-1B site models.

However, the ERT also shows a higher resistivity zone that starts approximately 20 m into the survey and extends to the Southeast far beyond the footpath. This zone is approximately 2 m through 8 m in depth. This high resistivity zone does not necessarily indicate a hard rock lithology zone as loose sand can have resistivities up to 5,000 ohm-meters (Octova., 2017). These high resistivities also rule out the quaternary sediments having any sort of clays in large quantities located within this region due to the integral high moistures of clays lowering resistivities (Gołębiowski., 2022). The 3D, Soft Rock CL, and IL7SL8 inversion models concur with the fact that this zone is a thin dry sand layer as there are no high velocities whatsoever in this region of any of their models of the DT-1B survey area. This region is also lacking any signal layers in the seismic inversion models caused by clay and sand interbedding as indicated by (Gołębiowski., 2022). The IGFW 2022 conclusion, that this high resistivity zone is a thin dry layer of sand, is corroborated by the seismic and ERT data comparison due to the lack of high velocities in that region in any of the inversion produced models.

7.3 Ground Penetrating Radar Comparison to Seismic Velocity Inversion Model

GPR is usually limited to depths of approximately 10 meters, however in highly resistive lithological stratigraphic facies, depths of 100s of meters can be possible. It transmits EM energy into the subsurface, hits a boundary or object, and is then reflected back towards the surface. The amplitude is then recorded by the receiving antenna (Everett., 2013). The EM waves' velocity is determined by the electrical permittivity of the subsurface lithology.

Different GPR frequencies will vary the depth and resolution of the survey. Lower frequencies will penetrate the subsurface in greater depth, but will lack resolution of the subsurface.

Attenuation of EM waves is a function of a medium's conductivity. Dry sand, similar to what is theorized in the ERT data, has a relatively low attenuating value of conductivity equal to 0.01-0.1 milliSiemens per meter (mS/m). Meanwhile the presence of water in lithologies will increase conductivity and attenuation (Gołębiowski., 2022).

In regards to the GPR survey the hard rock lithologies are near crystalline so there will be low to no reflections within, however there will be a very strong and well-defined reflection on the surface of the lithology. The sedimentary quaternary deposits will have boundaries within its stratigraphy and thus will display layers in the GPR model. Of the three surveys that were conducted during the IGFW class the highest resolution, but least penetrating is the 250 MHz, then the 100 MHz, and the highest penetrating, but lowest resolution, is the 25 MHz survey. Figure 7.8 displays the 25 Mhz GPR survey results near IL 4. Figure 7.9 displays the 100 MHz GPR survey results near IL9. Figure 7.10 displays the 250 MHz GPR survey near IL 13.

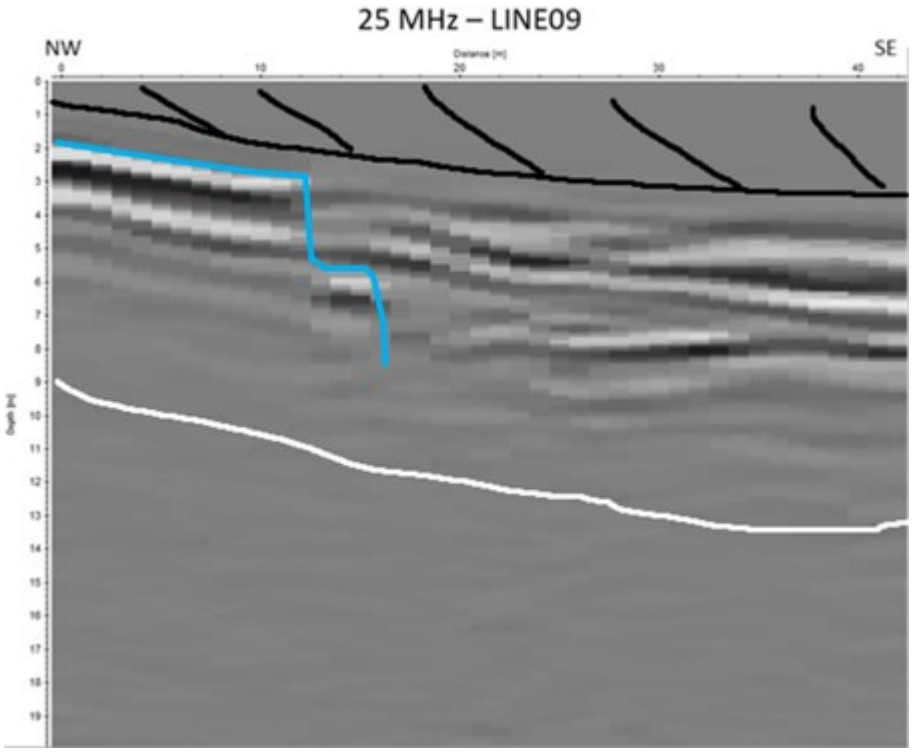

Figure 7.8*: This Figure modified from (Greenwood., 2023) displays Line09 of the 25 MHz GPR survey. The 25 MHz GPR Line09 is comparable in location to IL4/IL5 in the seismic survey. The origin labelled with NW is the same location near the cliff face as all the previous figures in this Thesis. The black area at the top of this figure indicates the air, which shows no reflections except for the topographic surface. The white line represents the ground water table, which completely attenuates GPR. The blue line indicates the totality of the hard rock protruding into the DT-1B survey area. The hard rock starts at approximately 1.5 m depth. It then continues at roughly the same depth below the surface, then undergoes a steep increase in depth, which then finally protrudes approximately 17 m into the survey area at 6 m-8 m depth.*

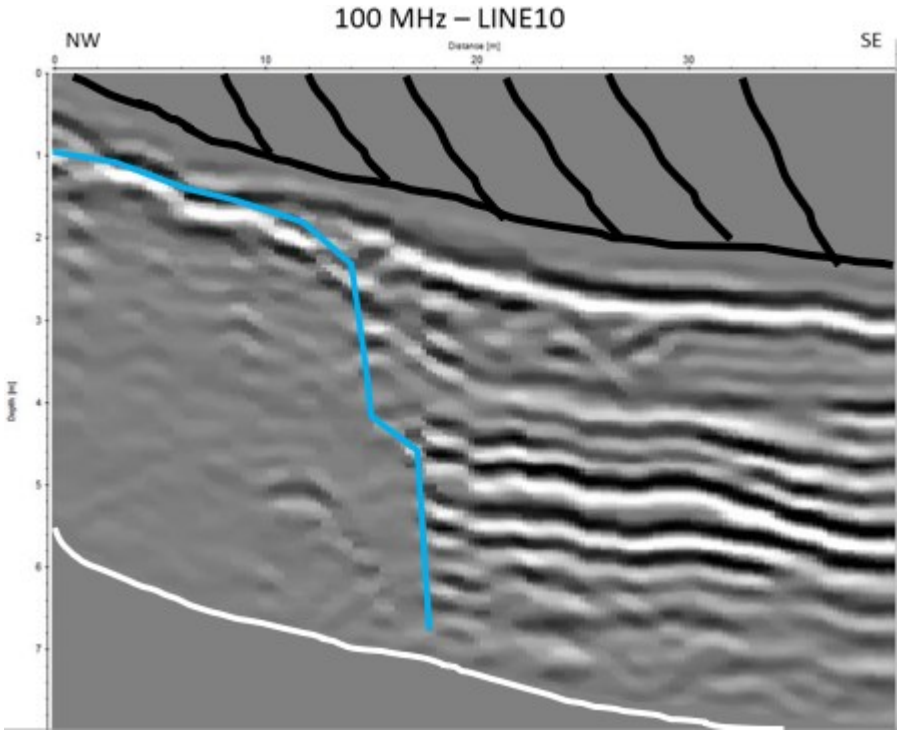

***Figure 7.9**: This Figure from (Greenwood., 2023) displays Line10 of the 100 MHz GPR survey. The 100 MHz GPR Line10 is comparable in location to IL8/IL9 in the seismic survey. The origin labelled with NW is the same location near the cliff face as all the previous figures in this Thesis. The black area at the top of this figure indicates the air, which shows no reflections except for the topographic surface. The white line represents the ground water table, which completely attenuates GPR. The blue line indicates the totality of the hard rock protruding into the DT-1B survey area. The hard rock starts at approximately at 1 m in depth and it stays at approximately the same depth below ground level until about 12 m into the DT-1B survey area. The ubiquitous steep increase in depth occurs at 12 m into the survey and continues until approximately 17 m into the survey at depth of 6 m.*

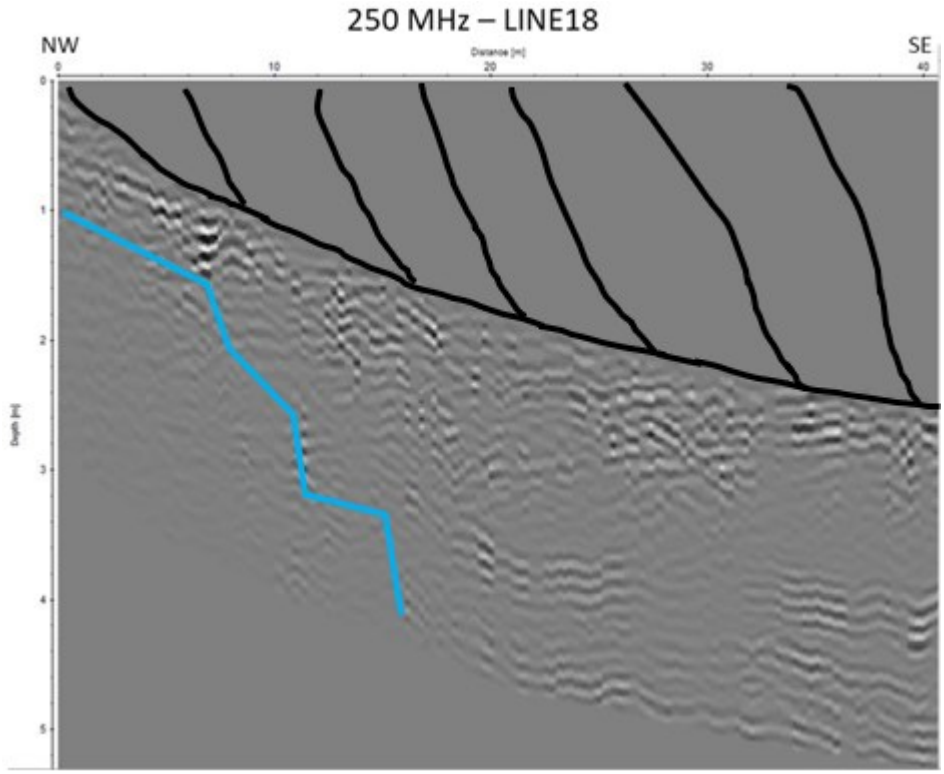

Figure 7.10*: This Figure from (Greenwood., 2023) displays Line18 of the 250 MHz GPR survey. The 250 MHz GPR Line18 is comparable in location to IL13/IL14 in the seismic survey. This is the least penetrating of the GPS surveys so the max depth is approximately 3 m. The origin labelled with NW is the same location near the cliff face as all the previous figures in this Thesis. The black area at the top of this figure indicates the air, which shows no reflections except for the topographic surface. The white line represents the ground water table, which completely attenuates GPR. The blue line indicates the totality of the hard rock protruding into the DT-1B survey area. The hard rock in this profile starts at 1 m depth, but has a less steep increase in depth than the other parts of the GPR survey, however it starts closer to the cliff. It terminates at 17 m into the DT-1B survey.*

The GPR display of the hard rock portion, soft rock portion, and the TZ are extremely similar to the Hard Rock CL, Soft Rock CL, IL7SL8, and 3D inversion models. The GPR displays a thin layer, approximately 35 cm, of weak reflections on top of the hard rocks on the cliff side of the survey, in all three GPR frequencies. This has been identified as sedimentary deposits on top of the hard rocks, as is evident in the ERT, in the field, and created in the velocity inversion models. There were also no fractures with apertures larger than the wavelength of the utilized GPR frequencies within the Kinzigite, as discussed in (Tao., 2021).

The sedimentary deposits entail the entire rest of the survey with no traces of hard rock boulders being located anywhere withing the DT-1B drill site. Depending upon the frequency

of the GPR it can have better or worse resolution of the DT-1B drill site, with the 250 MHz being the most accurate, however it does not reach the even limited depth of the seismic survey. All of the frequencies hit what is considered to be the water table and thus the GPR is severely attenuated. All three of the GPR surveys display similar reflections of subsurface layers in depths before the water table thus the quaternary deposits can be determined as being clay free utilizing knowledge gathered from (Gołębiowski., 2022). The GPR of 250 MHz has a better resolution of the exact top of the hard rock and its sharp decent in the subsurface gains much more detail in comparison to the velocity inversion model, however it cannot reach the depth of the of the velocity inversion model.

7.4 Comparison Conclusion

The GPR survey is comparably closer to the seismic velocity inversion model created in this Thesis than that of the ERT survey. This is due to the fact that the GPR and Inversion model both lack a possible hard rock lithology being located underneath and beyond the footpath. This misattribution of the subsurface lithologies would be a possible model of the DT-1B drill site had the IGFW not utilized a seismic survey, similar to the surveys conducted by Tao (2021). The possible issues of seismic refraction being poorly sensitive to shallow low velocity zones as discussed in (Owoc., 2019) did not become apparent in this Thesis, which is attributable to the density of the receivers and shots within the small footage of the DT-1B drill site.

The lack of evidence of clays in the quaternary sediments (Gołębiowski., 2022) determined that if the deposits in the DT-1B drill site are from the nearby Toce River, the surveyed sediments are gravel and sand dominated. This is in accordance with quaternary deposits, in the IVZ, are dominated by fluvial or glacial deposits in the mountains, hills, and modern river valleys (Piana., 2017).

The velocity models generated in this Thesis required a small layer of low velocity surficial layer on top of the hard rocks, even when not entirely existent, to have low RMSE values similar to a known issue of the seismic refraction inversion process described in (Hirsch., 2008) which is demonstratable in Table 5.2 and Figure 5.14, as the IL7 Test values have a starting model with much higher velocity rocks at the surface. These issues aside the velocity model generated in Simulr16 corelates closely to the GPR and ERT data gathered in the IGFW course. Whilst the inversion process for the velocity model does not include the elevation differences, the resultant model can be used in conjunction with the ERT and GPR to characterize the DT-1B drill site.

8: Concluding Remarks

8.1 Conclusions

This thesis creates three 2D inversion models which are then utilized to create a 3D inversion model for the two lithologies, hard rock Kinzigite and soft rock quaternary sediments, that compose the DT-1B drill site. The Transition Zone between the lithologies is characterized at the same time. The Kinzigite formation is determined to be a subsurface extension of the cliff that is located to the North-West of the drill site.

These models determine that the quaternary sediments dominate approximately the South-Eastern two thirds of the drill site, and has P-wave Velocities ranging from 100 m/s to 500 m/s. The remaining North-Western third of the drill site is comprised of the Kinzigite formation, and has P-Wave Velocities ranging from 2,500 m/s to 6,000 m/s. There is a thin layer, approximately 0 to 35 cm, of sediments on top of the Kinzigite. The Kinzigite extends anywhere from 10 m to 17 m into the drill site at a depth of approximately 1 m, with the farthest-reaching extensions being on the edges of the seismic survey. It then sharply increases in depth to approximately 9.5 meters. At this depth the Kinzigite penetrates further into the drill site up to 26 m. It is likely that the Kinzigite formation continues to extend South-East at deeper depths, however it is unverifiable with the currently available data. While large fractures are not apparent in the Kinzigite the likelihood of Kinzigite is high as the top portion of it shows signs of high weathering.

The Transition Zone follows the trend of the Kinzigite formation's penetration into the drill site, and is even observable at the surface using variations of grass growth. It has an angle of approximately 60 degrees from the top of the Kinzigite to the deeper portion.

This final 3D inversion model correlates well with the IGFW 2022 ERT and GPR data. Neither the inversion process, nor the two other geophysical process detected any loose boulders of Kinzigite located within the quaternary sediments. There is a large layer of dry sand in the quaternary deposits in the south eastern portion of the survey, which is observable in the ERT data. There is also a lack of any evidence of clays or even small interbedded layers of clays which might have been produced by the nearby Toce River.

A good velocity model for any future work in or near the DT-1B drill site should be as follows: a thin 30 cm layer of 150 m/s sediment placed on top of a 12 m wide layer of Kinzigite of 5,000 m/s. This layer then terminates with an approximately 60-degree sloped edge that delves 6 meters into the subsurface before flattening out again. In contact with this layer is a quaternary sedimental layer that has an average velocity of 350 m/s.

8.2 Outlook

IGFW is a field work that occurs yearly. This enables the possibility for a return to the survey site and create a larger survey that will enable greater depth penetration. This could allow the true depth of the cliff to the North-West to be discovered along with the possibility if it continues migrating to the South-East into what is this survey area. It could also discover how the cliff migrates towards the North-East. Also, further work on this data itself could be performed in conjunction with the ERT and GPR.

The DIVE project has two other boreholes planned. A similarly designed survey can be performed at each borehole with DIVE. Each could involve both P-wave and S-wave seismic survey. This survey's data did not include S-wave data due to issues in the field during the IGFW. So, both borehole sites could have similar or larger survey layouts utilizing S-wave seismics, and then all of the surveys could be compared to one another.

The seismic data itself could undergo further work and do a complete seismic processing flow. Following this processing flow a redo, or reuse, of these inversion velocity models and compare and contrast how these two separate methods analyze the data, and what their output models are.

References

American Geological Institute. Glossary of Geology and Related Sciences. Washington, DC., 1957m 325 pp; supplement, 1960, 72 pp.

Barnston, A. G. (1992). Correspondence Among the Correlation, RMSE, and Heidke Forecast Verification Measures; Refinement of the Heidke Score, *Weather and Forecasting*, Vol.7, 699-709.

Benson, R., et al. (1984). *Geophysical Techniques for Sensing Buried Wastes and Waste Migration.* Lockheed Engineering and Management Services Co.

Bleibinhaus, F. (2003). 3D Simultaneous Refraction and Reflection Seismic Travel Time Tomography and Application to Deep Seismic TRANSALP Wide-Angle. Doctoral Dissertation, University of Munich, Munich.

Brodie, K. H., Rutter, E. H. (1987). Deep Crustal Extensional Faulting in the lvrea Zone of Northern Italy, *Tectonophysics*, 140, 193-212.

Butchibabu, B., Khan, P. K., Jha, P. C. (2021). Geophysical Investigations for Stability and Safety Mitigation of Regional Crude Oil Pipeline Near Abandoned Coal Mines, *Journal of Geophysics and Engineering,* 18(1), 145-162.

Dashti, M., Stuart, A. M. *The Bayesian Approach to Inverse Problems*. Springer; (2017)

Everett, M., *Near-Surface Applied Geophysics*. Cambridge University Press; (2013).

Google Earth Pro, (2022). *Ornavasso Italy, 45°58'59.51"N, 8°23'56.09"E elevation 223M.* 3D Terrain data layer. [Image @ 2023 Maxar Technologies] Available at: http://www.google.com/earth/index.html [Accessed 02 January 2024].

Gołębiowski, T., Piwakowski, B., Ćwiklik, M. (2022) Application of Complex Geophysical Methods for the Detection of Unconsolidated Zones in Flood Dikes, *Remote Sensing*, 14(3):538.https://doi.org/10.3390/rs14030538

Grandis, H., Dahrin, D. (2014). Constrained Two-Dimensional Inversion of Gravity Data, *Journal of Mathematical and Fundamental Sciences,* Vol. 46(1), 1-13.

Greenwood, A. (2023). Personal Communication, IGFW Student Report, Montanuniversitat Leoben.

Gribenko, A., Zhdanov, M. (2017). Regularized Gauss-Newton Method of Nonlinear Geophysical Inversion in the Data Space: Applications to 3D Magnetotelluric Inversion, *SEG Technical Program Expanded Abstracts,* doi:10.1190/segam2017 -17632844.1

Hagelund, R., Levin, R., New, S. (2023). SEG-Y Revision 2.1 Data Exchange Format, Tulsa, OK. Society of Exploration Geophysicsts.

Haerudin, N., Yogi, I. (2021). A Combination of Monte-Carlo and Damped Least Square Inversion Method for Determining Radon Source in Geothermal Case, *Journal of the Earth and Space Physics,* Vol. 46, No.4, 103-116.

Hirsch, M., Bentley, L., Dietrich. P. (2008). A Comparison of Electrical Resistivity, Ground

Penetrating Radar and Seismic Refraction Results at a River Terrace Site, *Journal of Environmental & Engineering Geophysics,* 13(4), 325-333.

Holt, J., Zelt, B. C. (1995). 3D Finite-Difference Reflection Traveltimes, *Geophysical Journal International,*121, 427-434.

Huang, H., Hsiao, C. K., Huang, S. Y. (2010). Nonlinear Regression Analysis, *International Encyclopedia of Education,* 3, 339-346.

Lewis, D. *Matrix Theory.* Singapore: World Scientific; (1991).

Lowther, D. A., Throne, R. D., Olson L. G., Windlel, J. R. (2001). A Comparison of Zero and First Order Tikhonov Regularization for an Inhomogeneous Volume, *Computers in Cardiology,* Vol.28, 541-544.

Maiti, S., Erram, V., Gupta, G., Tiwari, R. (2012). ANN Based Inversion of DC Resistivity Data for Groundwater Exploration in Hard Rock Terrain of Western Maharashtra (India), *Journal of Hydrology*, 464-465, 294-308.

Octova, A., Yulhendra, D. (2017). Iron Ore Deposits Model Using Geoelectrical Resistivity Method with Dipole-Dipole Array, *MATEC Web of Conferences,* doi: 10.1051/matecconf/201710104017.

Owoc, B., Marciniak, A., Dzierzek, J., Kowalczyk, S., Majdanski, M. (2019). Seismic Imaging of the Mesozoic Bedrock Relief and Geological Structure Under Quaternary Sediment Cover: The Bolmin Syncline (SW Holy Cross Mountains, Poland), *Geosciences,* 9, 447. https://doi.org/10.3390/geosciences9100447.

Piana, F., et al. (2017). Geology of Piemonte Region (NW Italy Alps-Apennines Interference Zone), *Journal of Maps,* 13(2), 395-405.

Pistone, M., et al. (2017). Report on the ICDP Workshop DIVE (Drilling the Ivrea-Verbano zonE), *Scientific Drilling,* 23, 47-56.

Pistone, M., et al. (2020). Joint Geophysical-Petrological Modeling on the Ivrea Geophysical Body Beneath Valsesia, Italy: Constraints on the Continental Lower Crust, *Geochemisty, Geophysics, Geosystems,* doi: 10.1029/2020gc009397.

Pramudya, F. A., Ningsih, R., Nurfaidah, H., Sephiana, S. E., Wibowo, R. C., Zaenudin, A. (2021). Using Grid Search and Guided Random Search (Simulated Annealing) Methods in Determining the Earthquake Hypocenter in the Majalengka Region, West Java on November 11, 2021, *Jurnal Geocelebes,* Vol. 7(1), 1-7.

Quick, J. E., Sinigoi, S., Mayer, A. (1995). Emplacement of Mantle Peridotite in the Lower Continental Crust, Ivrea-Verbano zone, northwest Italy, *Geology*, 23(8), 739.

Rawlinson, N., Sambridge, M. (2003). Seismic Traveltime Tomography of the Crust and Lithosphere, *Advances in Geophysics,* 81-198.

Rutter, E., Brodie, K., James, T., Burlini, L. (2006). Large-Scale Folding in the Upper Part of the Ivera-Verbano Zone, NW Italy, *Journal of Structural Geology*, 29 (2007), 1-17.

Sambridge, M., Gallagher, K. *Encyclopedia of Solid Earth Geophysics*. Springer; (2011).

Sambridge, M., Mosegaard, K. (2002). Monte Carlo Methods in Geophysical Inverse Problems, *Reviews of Geophysics,* Vol. 40(3), 3-29.

Scarponi, M., et al. (2020). New Gravity Data and 3D Density Model Constraints on the Ivrea Geophysical Body (Western Alps), *Geophysical Journal International,* 222(3), 1977-1991.

Scherzer, O., Hofmann, B., Nashed, Z. (2023). Gauss-Newton Method for Solving Linear Inverse Problems with Neural Network Coders, *Sampl. Theory Signal Process. Data Anal,* 21, 25, https://doi.org/10.1007/s43670-023-00066-6.

Schmid, S. M., Kissling, E. (2000). The Arc of the Western Alps in the Light of Geophysical Data on Deep Crustal Structure, *Tectonics,* 19(1), 62-85.

Schmid, S. M., Kissling E., Diehl, T. (2017). Ivrea Mantle Wedge, Arc of the Westen Alps and Kinematic Evolution of the Alps-Apennines Orogenic System, *Swiss Journal of Geosciences*, 110(2), 581-612.

Shan, Y., Gong, F., Li, Z., Lin, G. (2007). A Grid-Search Inversion Method Looking for the Best Classification of Polyphase Fault/Slip Data, *Tectonophysics,* 433(1-4), 53-64.

Tao, M., Chen, X., Cheng, Q., Binley, A. (2021). Evaluating the Joint Use of GPR and ERT on Mapping Shallow Subsurface Features of Karst Critical Zone in Southwest China, *Vadose Zone Journal,* 21(1), 1-14

Thurber, C. (1983). Earthquake Locations and Three-Dimensional Crustal Structure in the Coyote Lake Area, Central California. *Journal of Geophysical Research,* Vol. 88, 8226-8236.

Appendix A (Extra Figures)

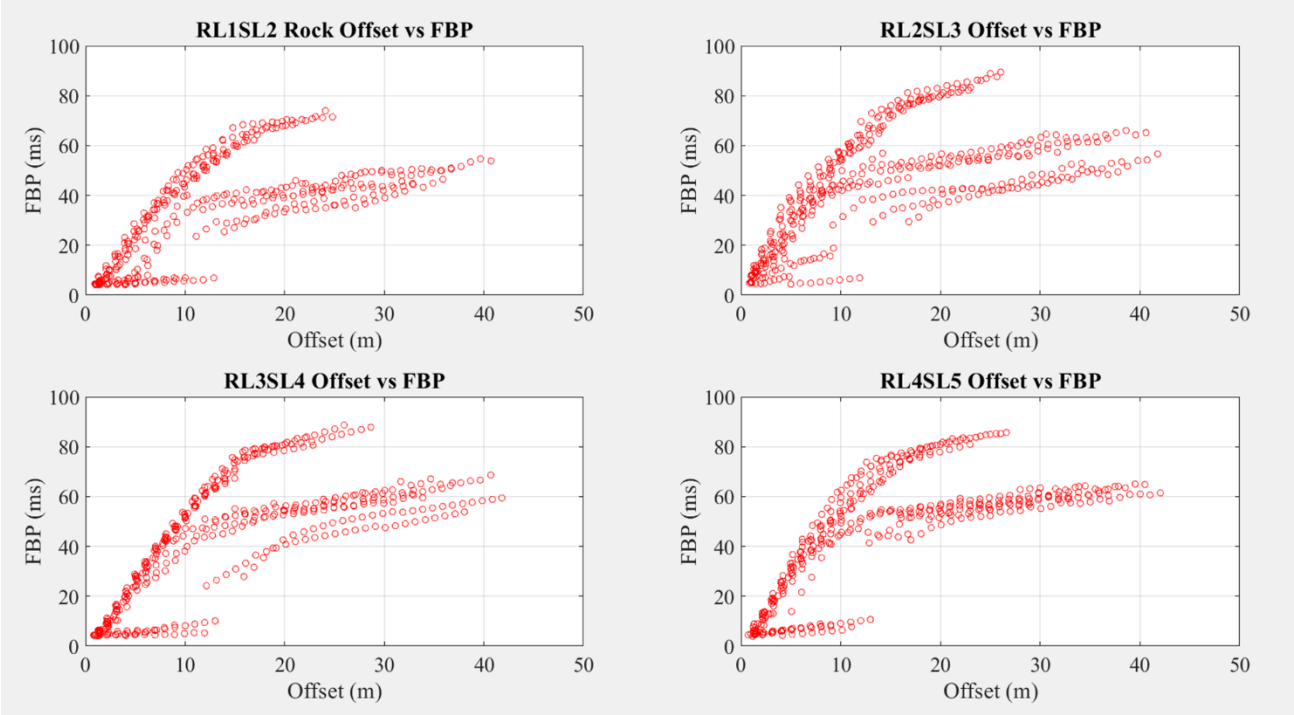

Figure 1: This displays the corrected Offset vs FBP of the first four In-Lines of the survey. Similar to Figure 4.9.

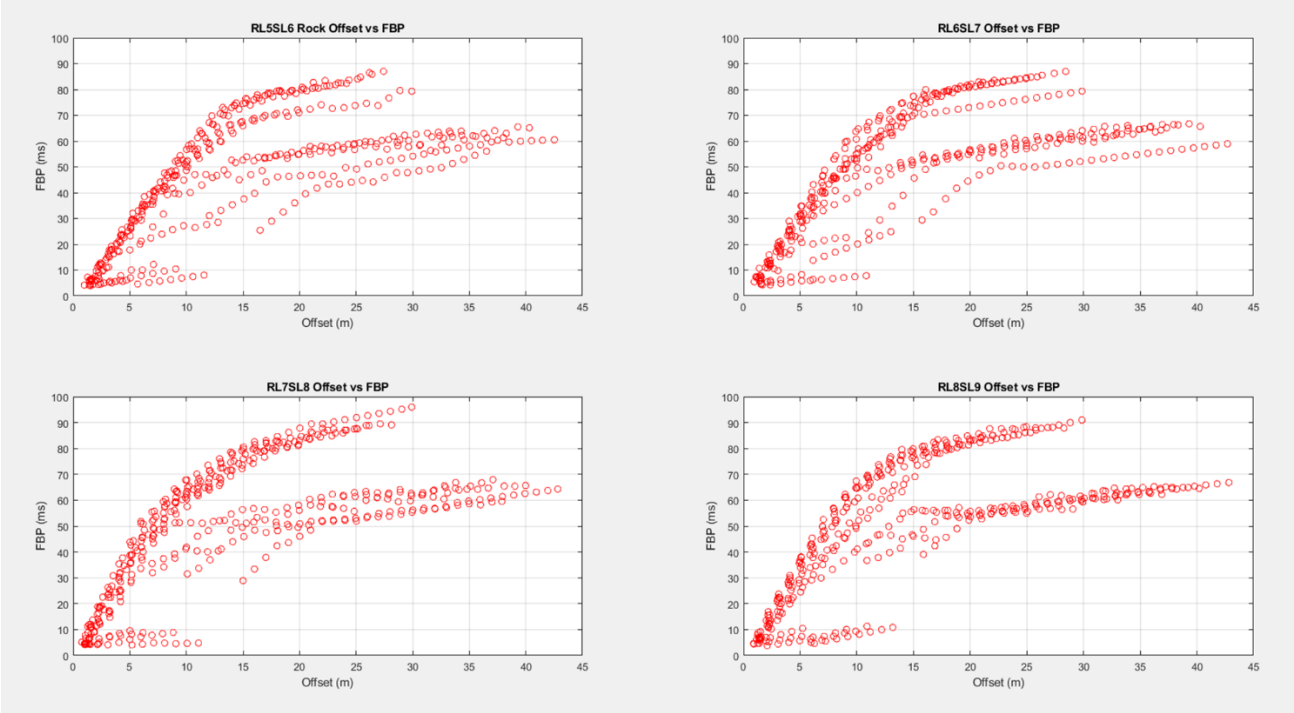

Figure 2: This displays the corrected Offset vs FBP of In-Lines 5-8 of the survey. Similar to Figure 4.9.

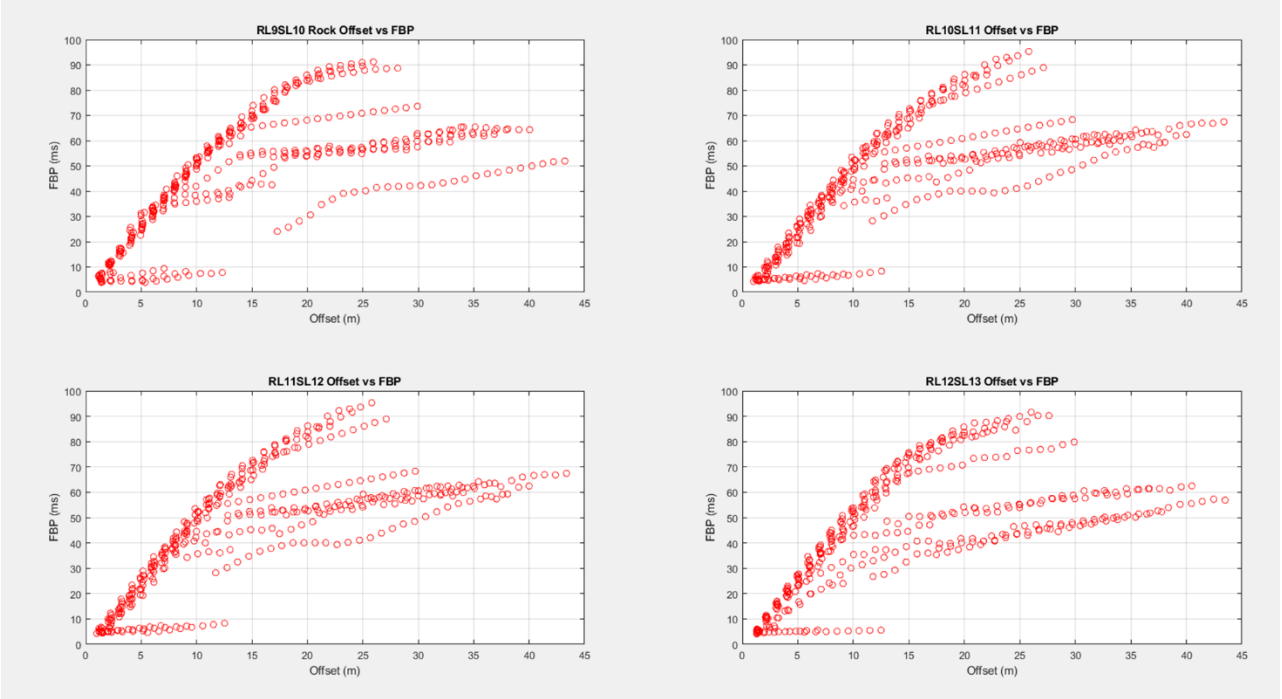

Figure 3: This displays the corrected Offset vs FBP of In-Lines 9-12 of the survey. Similar to Figure 4.9.

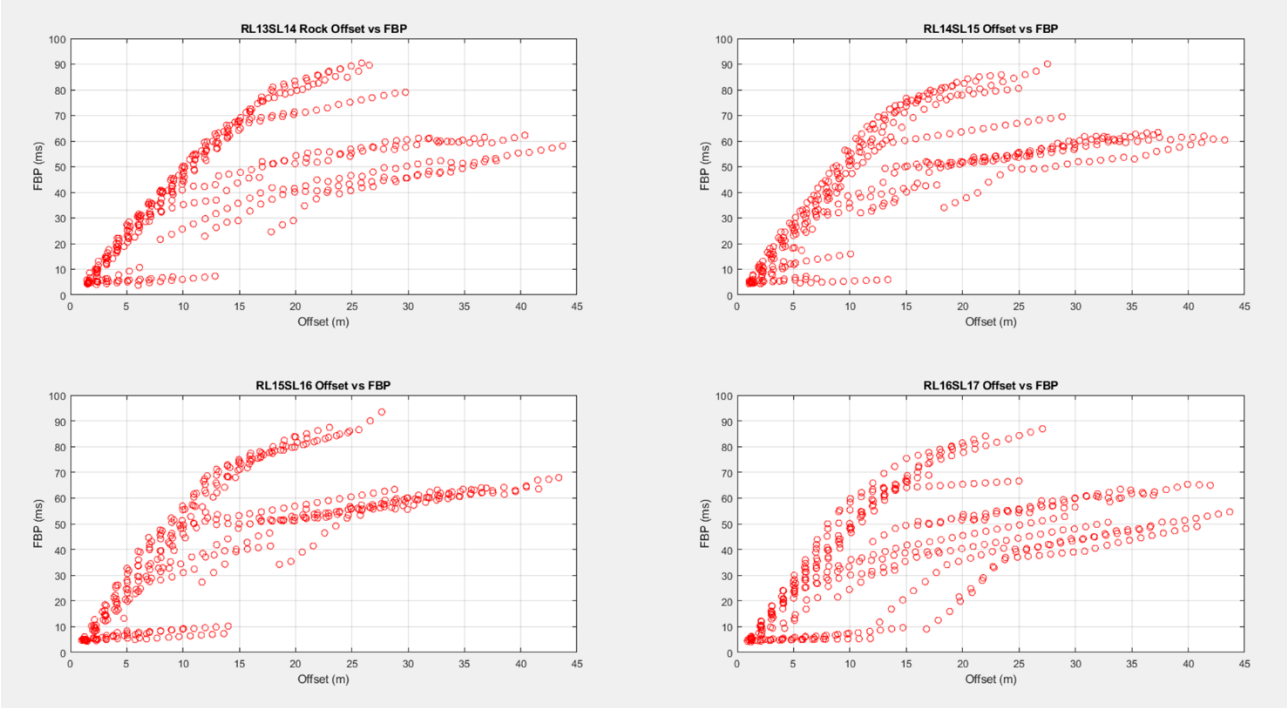

Figure 4: This displays the corrected Offset vs FBP of In-Lines 13-16 of the survey. Similar to Figure 4.9.

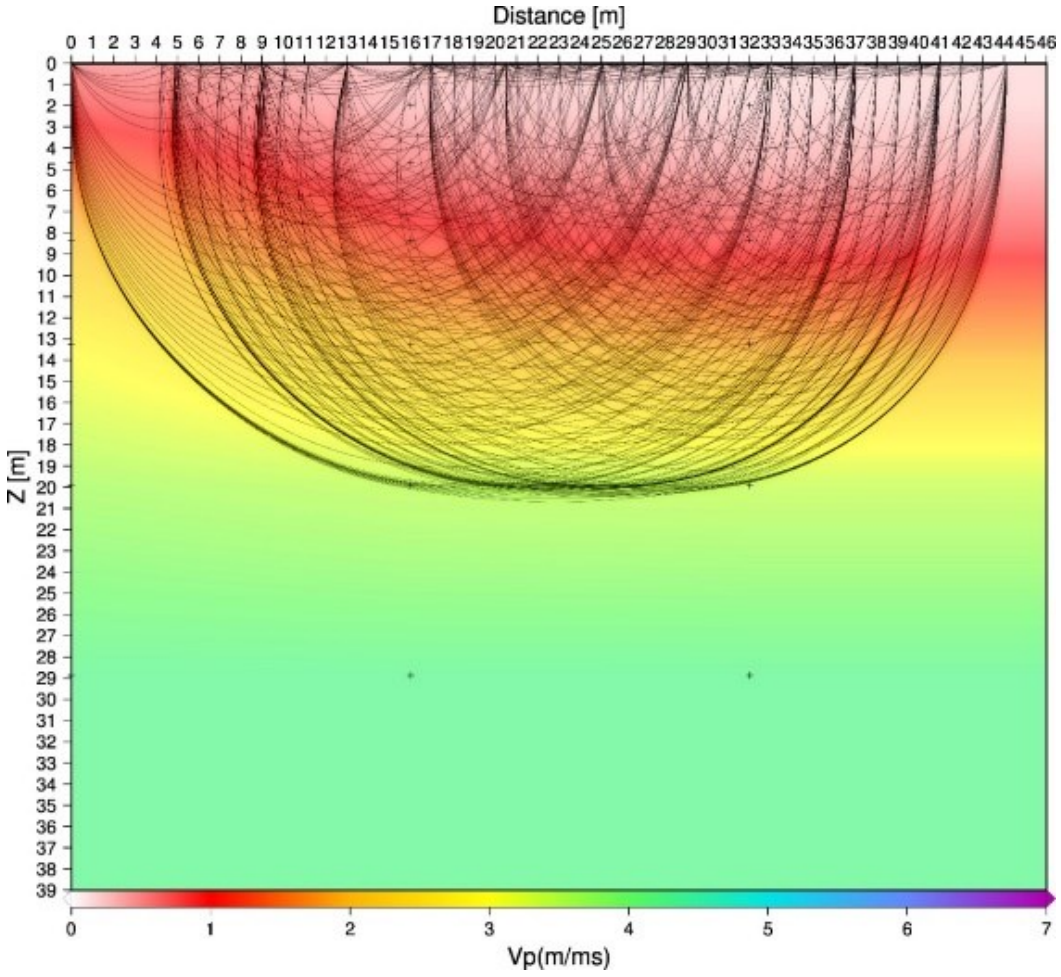

Figure 5: This is the 1st densification step of the HVGD representing the 16 meter by 2 meter node spacing.

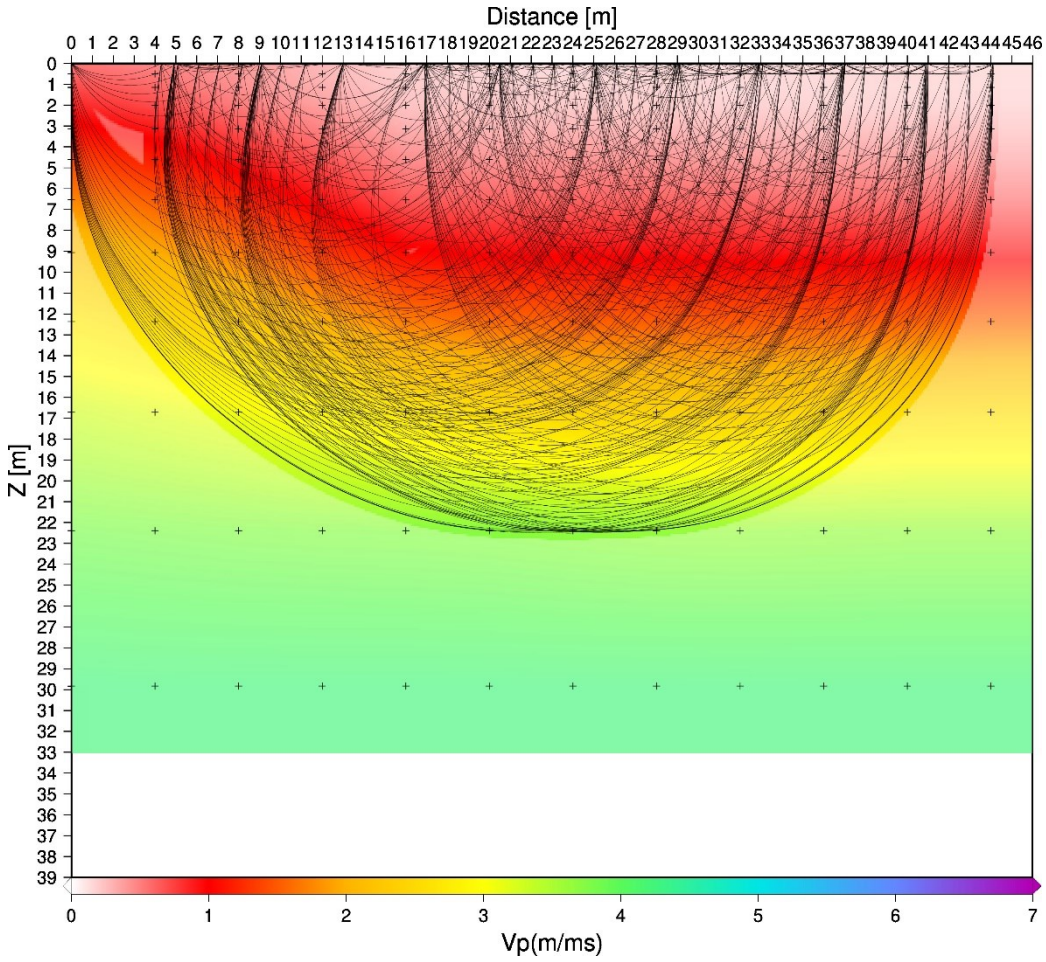

Figure 6: This is the 3rd densification step of the HVGD representing the 4 meter by .5 meter node spacing.

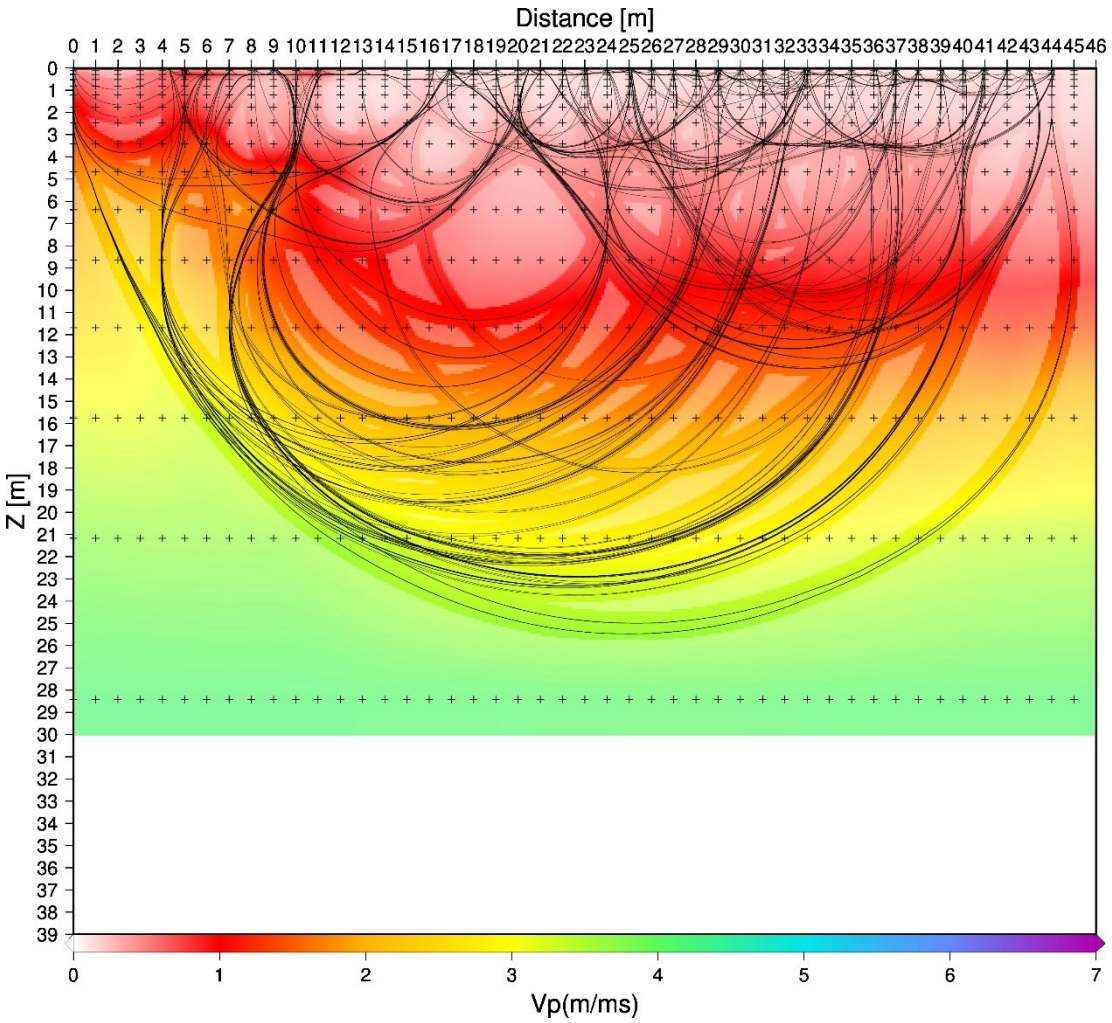

Figure 7: This is the 5th densification step of the HVGD representing the 1 meter by 0.125 meter node spacing.

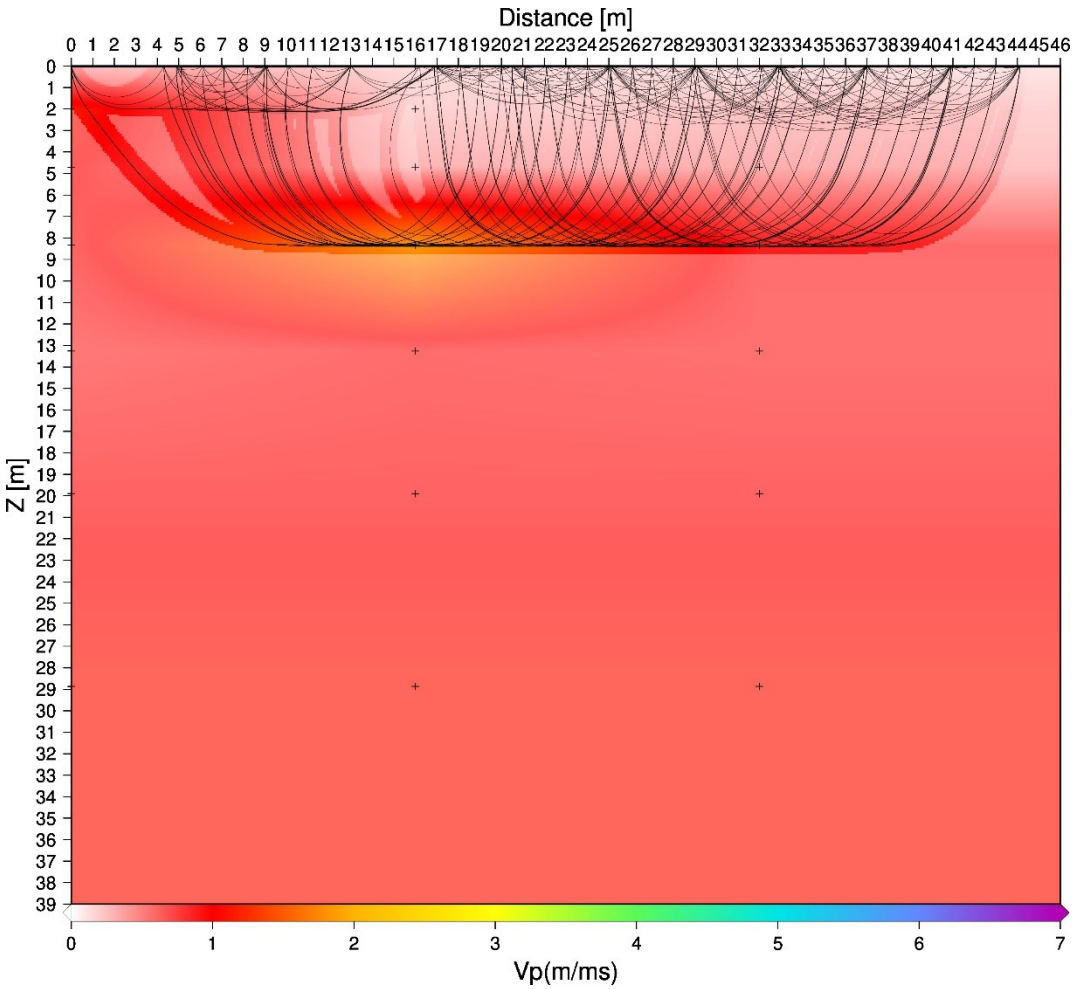

Figure 8: This is the 1st densification step of the LVGD representing the 16 meter by 2 meter node spacing.

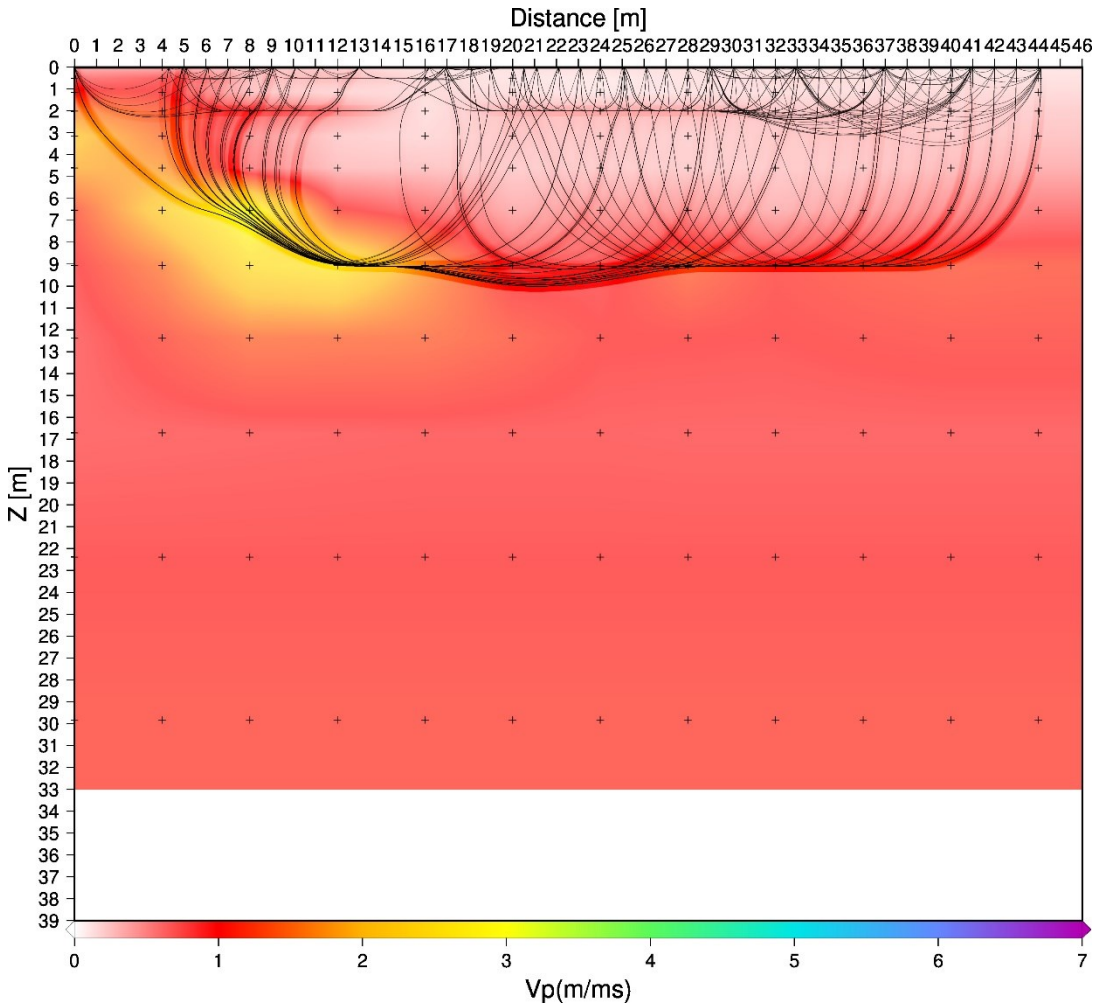

Figure 9: This is the 3rd densification step of the HVGD representing the 4 meter by .5 meter node spacing.

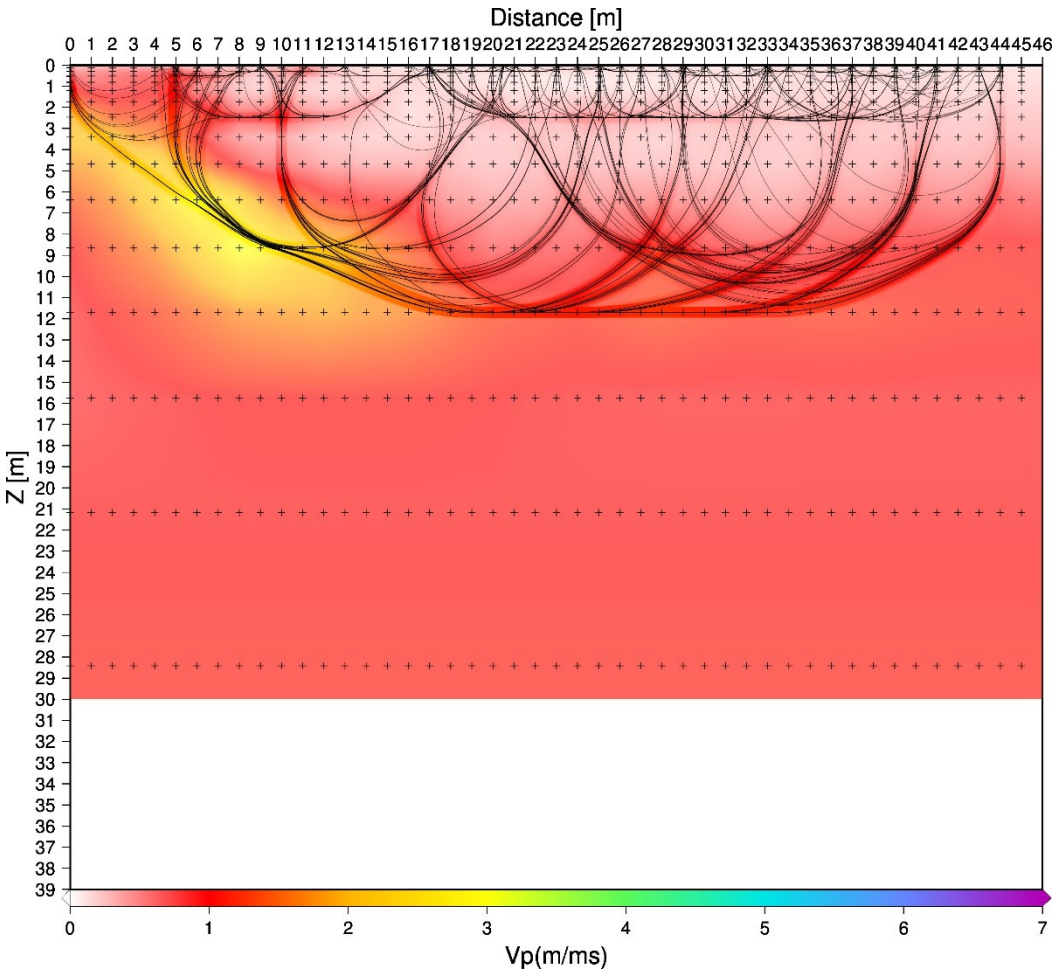

Figure 10: This is the 5th densification step of the LVGD, representing the 1 meter by 0.125 meter node spacing.

Appendix B (Matlab Codes)

This is the Matlab code used to translate SEGY data into data readable by Simulr16:

```
FB=load('segment6fbp.prn');
ZP=load('zplot.hdr');

index = find(ZP(:,4)==1);

ZP2=ZP;
l = size(index);

for i=1:l

    ZP2(index(i),9) = FB(i);
    if FB(i) == -1
        ZP2(index(i),5) = -1;
    end

end


Rec_loc = load("rec_o.lst");
Sht_loc = load("sht_o.lst");

Rec_loc2 = load("rec.lst");
Sht_loc2 = load("sht.lst");

figure
plot(Rec_loc(:,1),Rec_loc(:,2),'b+')
hold on
plot(Sht_loc(:,1),Sht_loc(:,2),'r*')
legend('Receivers','Shots')
title('Original')
hold off
grid on
axis equal

figure
plot(Rec_loc2(:,1),Rec_loc2(:,2),'b+')
hold on
plot(Sht_loc2(:,1),Sht_loc2(:,2),'r*')
legend('Receivers_rot','Shots_rot')
title('Rotated')
hold off
grid on
axis equal
```

This is the Matlab Grid Refinement Code:

```
S = 0.01;
xmin = -10;
xmax = 56;
zmin = -2;
zmax = 30;
X = [xmin:S:xmax];
Z = [zmin:S:zmax];
X = round(X,3);
Z = round(Z,3);
cols =  size(X,2);
rows =  size(Z,2);
file = fopen('vp12.bin');
    A = fread(file,[rows cols],'single');
    fclose(file)
    figure
    imagesc(X,Z,A)
N = load('node.xyz');
Nx = unique(round(N(:,1),3));
Ny = unique(round(N(:,2),3));
Nz = unique(round(N(:,3),3));
nx = size(Nx,1);
nz = size(Nz,1);
vel_node = zeros(nz,nx);
for i = 1:nz
    index2 = find(Z==Nz(i));
    for j= 1:nx
        index = find(X==Nx(j));
    vel_node(i,j) = A(index2,index);
    end
end
vel_node = vel_node';
s = size(vel_node);
lim1 = s(2);
lim2 = s(1);
fileID = fopen('SVvel_node1x0125.txt','w');
 for i= 1:lim1
     for j= 1:lim2
         fprintf(fileID, '% 3.2f',vel_node(j,i));
         if ~rem(j,16)==1
             fprintf(fileID, '%c\n','');
         end
     end
     fprintf(fileID, '%c\n','');
 end
 fclose(fileID)
figure
imagesc(X,Z,A)
hold on
plot(N(:,1),N(:,3),'kx')
```

This is the code utilized for Figures 4.3 and 4.4:

```
file_name = ('Final3dbreaks.prn');
data = importdata(file_name);
source_x = data(:, 1);
receiver_x = data(:, 2);
first_break_picks = 4+ data(:, 3);
unique_source_x = unique(source_x);
num_sources = numel(unique_source_x);
color_map = lines(num_sources);
figure;
for i = 1:num_sources
    source_x_location = unique_source_x(i);
    idx = source_x == source_x_location;
    plot(receiver_x(idx), first_break_picks(idx), 'Color', color_map(i, :),
'DisplayName', ['Source X = ', num2str(source_x_location)]);
    axis ij
    hold on;
end
xlabel('Receiver X');
ylabel('First Break Picks');
title('First Break Picks vs. Receiver X for Different Source X Locations');
set(gca, 'YDir', 'reverse');
legend('Location', 'Best');
grid on;
hold on
plot([receiver_x(1) receiver_x(end)], [4 4])
hold off;
```

This is the code utilized for Figure 1.1 and 5.1

```
[Lat,Lon]=utm2ll(intmE(:), intmN(:),32);
return
filenameOut='SWD-01b.txt';
dlmwrite(filenameOut,[Lat,Lon],'delimiter','\t','precision',8);
```

This is the code utilized for figures 4.5 through 4.11:

```
close all; clear all; clc
file_name = (['HROC.asc']);
data = importdata(file_name);
column_x = data(:, 1);
column_y = 4+data(:, 2);
column_y(column_y==3)=NaN;
figure(1);
subplot(1,2,1)
plot(column_x, column_y, 'ro');
hold on
title('Hard Rock Offset vs FBP');
```

```
xlabel('Offset (m)');
ylabel('FBP (ms)');
ylim([0 60])
grid on;
```